RCA REVIEW

a technical journal

RADIO AND ELECTRONICS
RESEARCH • ENGINEERING

Published quarterly by
RCA LABORATORIES

in cooperation with all subsidiaries and divisions of
RADIO CORPORATION OF AMERICA

VOLUME XXII | JUNE 1961 | NUMBER 2

CONTENTS

RCA REVIEW is regularly abstracted and indexed by ***Industrial Arts Index Science Abstracts*** (I.E.E.-Brit.), ***Electronic Engineering Master Index, Chemical Abstracts, Proc. I.R.E.***, and ***Electronic & Radio Engineer.***

RCA REVIEW

BOARD OF EDITORS

Chairman
R. S. Holmes
RCA Laboratories

E. I. Anderson
Home Instruments Division

A. A. Barco
RCA Laboratories

G. L. Beers
Radio Corporation of America

G. H. Brown
Radio Corporation of America

I. F. Byrnes
Industrial Electronic Products

A. L. Conrad
RCA Service Company

E. W. Engstrom
Radio Corporation of America

D. H. Ewing
Radio Corporation of America

A. N. Goldsmith
Consulting Engineer, RCA

J. Hillier
RCA Laboratories

E. C. Hughes
Electron Tube Division

E. A. Laport
Radio Corporation of America

H. W. Leverenz
RCA Laboratories

G. F. Maedel
RCA Institutes, Inc.

W. C. Morrison
Industrial Electronic Products

H. F. Olson
RCA Laboratories

D. S. Rau
RCA Communications, Inc.

D. F. Schmit
Radio Corporation of America

L. A. Shotliff
RCA International Division

S. Sternberg
Astro-Electronics Division

W. M. Webster
RCA Laboratories

I. Wolff
Radio Corporation of America

Secretary
C. C. Foster
RCA Laboratories

REPUBLICATION AND TRANSLATION

Original papers published herein may be referenced or abstracted without further authorization provided proper notation concerning authors and source is included. All rights of republication, including translation into foreign languages, are reserved by RCA Review. Requests for republication and translation privileges should be addressed to *The Manager.*

THE HELIX PARAMETRIC AMPLIFIER— A BROADBAND SOLID-STATE MICROWAVE AMPLIFIER*

By

C. Louis Cuccia[†] and Kern K. N. Chang[‡]

Summary—This paper describes a parametric amplifier which uses a helix as a slow-wave distributed interaction structure and has variable-capacitance solid-state diodes distributively coupled to the helix. An applied signal and a pump signal are coupled to the input of the helix; interaction occurs with the diodes and provides parametric amplification of the applied signal at the output of the helix. The helix parametric amplifier has an insertion loss of approximately 30 decibels betwen the input and the output of the helix before application of the pump signal; net gains as high as 38 decibels have been measured with the pump signal applied.

Experimental operation of helix parametric amplifiers in the 2200- to 2300-megacycle and 1800- to 2000-megacycle frequency bands is described. Gains in excess of 30 decibels have been measured over narrow frequency ranges. Operating bandwidths from 5 to 10 per cent at substantial gain have been achieved at pump frequencies less than twice signal frequency. Terminal single-sideband noise figures as low as 4.5 decibels have been measured.

INTRODUCTION

THE PARAMETRIC AMPLIFIER has recently become the object of world-wide research and development. In general, the development has been concentrated on two specific types: the cavity two-terminal parametric amplifier[1-3] and the traveling-wave parametric amplifier.[4-10]

The cavity type has several disadvantages: it has a narrow bandwidth, it requires a circulator, and its gain is very sensitive to variations in pump frequency and power. The traveling-wave type using a diode-loaded transmission line has shown great promise as a wide-band amplifier in analytical studies by Cullen,[4] Heilmeier,[8] and others. However, the large number of diodes required for usable gain (approximately two diodes per decibel of gain, according to

---

* Manuscript received.

[†] RCA Electron Tube Division, Los Angeles, Calif.

[‡] RCA Laboratories, Princeton, N.J.

Heilmeier), the close spacings involved, and the tendency for the pump power to be dissipated in the first few diodes restricts the operation of the device as a microwave amplifier. Other traveling-wave structures which use a periodically loaded waveguide[9] for operation and a coupled-cavity traveling-wave structure[10] at S-band have indicated the feasibility of the traveling-wave approach for the case when the pump power is applied at a multiplicity of points in the parametric amplifier structure.

This paper describes an approach to parametric amplifiers which uses a unique microwave filter circuit, the diode-loaded helix, first proposed by Chang.[11] The circuit has exceptional capabilities as a microwave-frequency low-noise amplifier including increased bandwidth, a small number of diodes, adaptability to circuit miniaturization, and inherently stable performance. The point of view of the paper is one of an experimental study so that circuit characteristics and capabilities are pointed out.

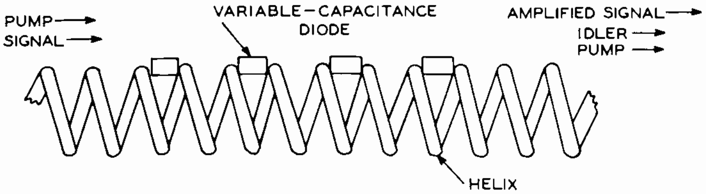

Fig. 1—Basic circuit structure of a diode-loaded helix parametric amplifier which uses variable-capacitance diodes as shunts for selected helix turns.

THE HELIX PARAMETRIC AMPLIFIER

In a basic helix parametric amplifier, varactor (variable-capacitance) diodes are distributively coupled to individual helix turns as shown in Figure 1; these diodes act as variable-capacitance shunts. The signal to be amplified, together with a pump signal is applied to the input section of the helix; the amplified version of the applied signal is derived from the output.

Figure 2 shows the principal components of the helix parametric amplifier: a length of helix, a helical coupler capable of coupling to the helix over almost two frequency octaves, and variable-capacitance semiconductor diodes housed in miniature pill-type structures. These structures are especially suitable as shunts for helix turns.

Figure 3 shows an experimental helix parametric amplifier having three diodes in the helix turns, helical couplers for coupling the signal to and from the helix, and a direct connection to the helix for the

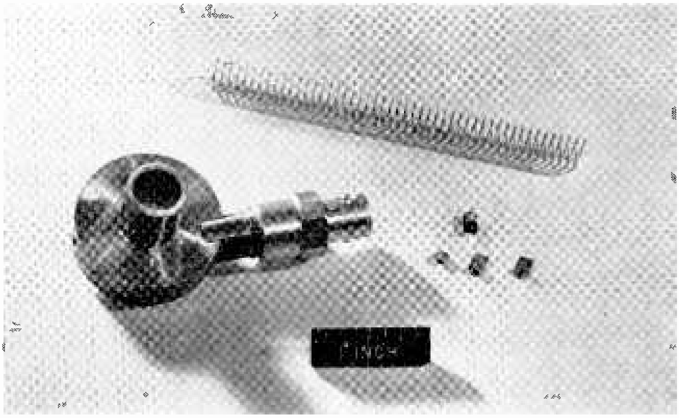

Fig. 2—Typical circuit elements of a helix parametric amplifier; helix, helical coupler, and pill-type variable-capacitance semiconductor diodes.

pump signal. This amplifier is typical of helix parametric amplifiers in which as few as two and as many as five or six diodes are used. Amplification is provided in the small exposed region indicated by the pencil point without the use of tuning stubs, numerous circuit structures, or narrow-band elements.

The small number of shunting diodes in a helix structure can develop higher voltages and store more energy than a diode-loaded transmission line or waveguide. This feature is due to the unusual

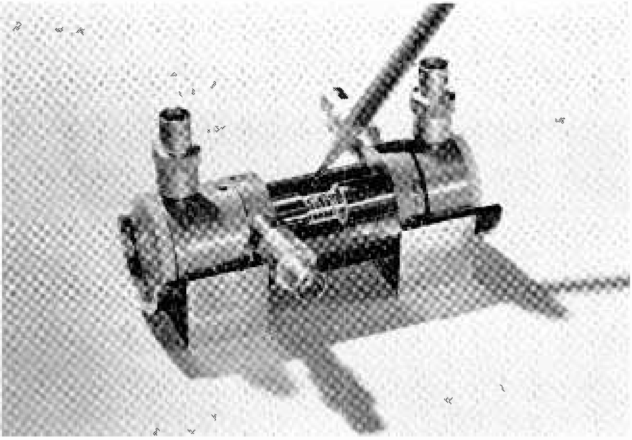

Fig. 3—An experimental helix parametric amplifier. The vertical connectors (left and right) are for pump signal and termination respectively. The pencil points to the small portion of the diode-loaded helix in which parametric amplification takes place.

filter characteristics inherent in a diode-loaded helix structure, and is augmented by a pump frequency which is less than twice the signal frequency. As shown in the curve of gain as a function of pump-power in Figure 4, the gain rises to a maximum value and then decreases with increasing pump power. On the other hand, the standard two-terminal cavity parametric amplifier has a gain curve in the usable-gain regions which continues to rise very rapidly as a function of increasing pump power. Such a characteristic indicates the need for stringent pump-power stabilization.

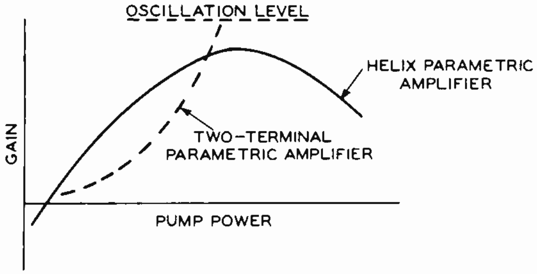

Fig. 4—Gain as a function of pump power for a conventional two-terminal parametric amplifier and a helix parametric amplifier.

The noise figure of the helix parametric amplifier is in the 5- to 7-decibel range as compared to 2 to 4 decibels for two-terminal cavity parametric amplifiers. There is a wide range of applications for amplifiers in the 5- to 7-decibel noise-figure category. The high degree of miniaturization possible with the parametric amplifier makes it very attractive for such applications.

FILTER-HELIX CIRCUIT

In the helix parametric amplifier, the applied signal and the pump signal interact successively in each diode-loaded helix turn and generate an idler signal at the difference frequency. Amplification is obtained at the signal and idler frequencies by conversion of power supplied by the pump to these frequencies.

The system interactions which occur in the helix parametric amplifier are different from those which occur in traveling-wave structures or two-terminal structures.

Experimental evidence indicates that the basic circuit of the helix parametric amplifier is comparable to that of a filter helix. The diode-loaded helix displays the general characteristics of a coupled multiple-tuned circuit at each of the three pertinent frequencies.

In deducing the basic nature of the parametric amplifier circuit, the effect of periodic loading of the helix with variable capacitance diodes must be considered first. The unloaded helix is a slow-wave structure which is nondispersive over wide ranges of frequencies encompassing a number of frequency octaves. Such unloaded helices, when wound with low-loss materials and supported in nondissipative structures, are capable of signal translation at an insertion loss of the order of a few decibels. Helix structures periodically loaded with electrically nonvariable elements have been used by Dodds and Peter to enhance the gain in a traveling-wave tube, and by Siegman and Johnson to suppress backward waves in a traveling-wave tube. However, the use of periodic loading elements which produce amplification is new in the microwave art.

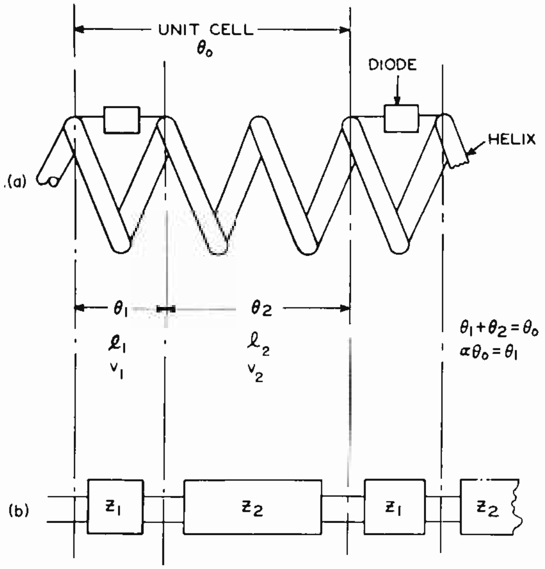

Fig. 5—Equivalent impedance (b) for a helix with its turns periodically loaded with diodes (a).

The helix, when periodically loaded by impedance elements, becomes dispersive and develops a pattern of transmission bands and stop bands. In the transmission bands, the stored energy per length of helix is greatly increased by periodic loading. A general analysis of the transmission characteristics of a periodically loaded helix in a traveling-wave tube, published by Dodds and Peter,[12-14] is applicable in defining stop and pass bands for the loaded helix shown in Figure 5.

In the diode-loaded helix of Figure 5(a), each loaded helix turn is a first section of filter having an electrical phase angle θ_1. The length of helix between that loaded turn and the next loaded turn is a second section of filter having an electrical phase angle θ_2. As indicated in Figure 5(b), impedances Z_1 and Z_2 represent, respectively, the diode-loaded helix turn and the following unloaded helix section.

The phase angles θ_1 and θ_2 can be related to the lengths, l_1 and l_2, and the phase velocities, v_1 and v_2, of the respective sections by the following expressions:

$$\theta_1 = \frac{\omega l_1}{v_1},$$

$$\theta_2 = \frac{\omega l_2}{v_2},$$

where ω is the angular frequency. The sum of the electrical angles of the two sections comprising a unit cell may be expressed as follows:

$$\theta_0 = \omega \left[\frac{l_1}{v_1} + \frac{l_2}{v_2} \right],$$

where $\theta_0 = \theta_1 + \theta_2$.

Dodds and Peter have established a parameter α which determines the ratios of the electrical angles in a unit filter cell comprised of the impedances Z_1 and Z_2;

$$\theta_1 = \alpha\, \theta_0,$$

$$\theta_2 = (1 - \alpha)\, \theta_0.$$

The phase angle, θ, of an infinite filter chain as related to the electrical angle, θ_0, and the ratio parameter, α, is shown to be

$$\cos\theta = \frac{K+1}{2}\cos\theta_0 - \frac{K-1}{2}\cos\left[\theta_0\,(1-2\alpha)\right].$$

The parameter K relates the difference in magnitudes of Z_1 and Z_2 and, therefore, the degree of periodic loading.

$$K = \frac{1}{2}\left[\frac{Z_1}{Z_2} + \frac{Z_2}{Z_1}\right].$$

This equation describes the existence of a pass band when cos θ is less than one, and a stop band when cos θ is greater than one. The limits of the bands are

$$\cos\theta = \pm 1.$$

Figure 6 shows the pass and stop bands as a function of frequency

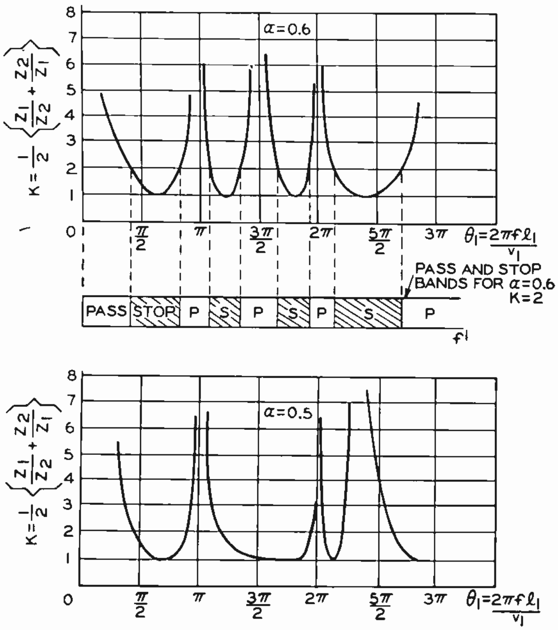

Fig. 6—Loading parameter K as a function of electrical angle θ_1 of the diode-loaded helix turn in each unit cell for two values of α.

and curves of K for $\alpha = 0.5$ and $\alpha = 0.6$. For $K = 1$ or $Z_1 = Z_2$, no stop bands are developed. As K is increased, stop bands become increasingly wider; their location depends upon frequency and on the ratio parameter, α.

The equation for K clearly defines the stop and pass bands for an infinitely long periodically loaded helix when the ratios of the electrical angles and the impedances of the sections of the cells are established. In the helix parametric amplifier, only a few unit cells are involved and the loading produced by the variable-capacitance diodes is relatively light. Therefore, the over-all aggregate of stop and pass bands displayed by a length of helix having periodic loading introduced into a short length is not as distinct as in the heavily loaded longer structure. In addition, there is the practical aspect of including the periodic-loaded length of helix as the middle of three successive lengths of helix, with the first and last lengths acting as input and output circuits to the periodically loaded length. The dissimilarity of the impedances of the loaded and unloaded lengths provides impedance discontinuities and reflections which make coupling to each end of the diode-loaded helix difficult.

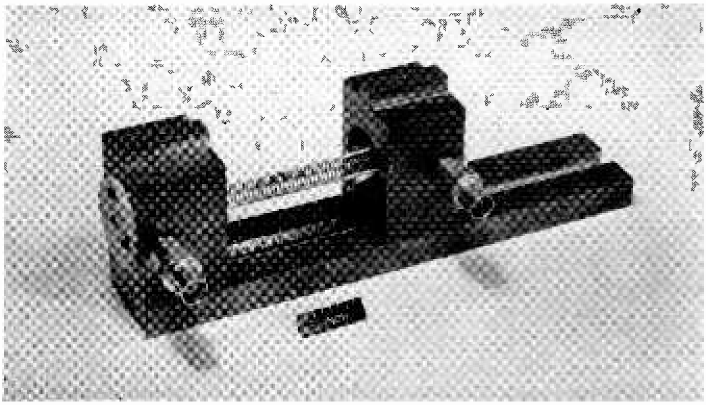

Fig. 7—Helix-and-coupling arrangement used for testing the transmission characteristics of the helix used in the helix parametric amplifier.

TRANSMISSION CHARACTERISTICS OF DIODE-LOADED FILTER HELIX

An experimental study of the transmission and coupling characteristics of a helix periodically loaded by variable-capacitance diodes along a portion of its length was undertaken using the structure shown in Figure 7. In this structure, the helix is supported by ceramic rods, and a direct connection is made to each end of the helix.

Semiconductor variable-capacitance diodes of the type shown in Figure 8 were used as helix-turn loading elements. These germanium-type diodes[15] have capacitances of the order of one picofarad. They are encapsulated in small cylindrical packages approximately one-tenth of an inch in diameter. The helix was similar to those used in RCA medium-power S-band traveling-wave tubes.

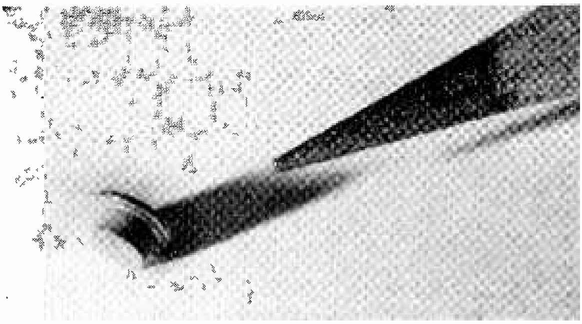

Fig. 8—The pill type of variable-capacitance semiconductor diode used in the helix parametric amplifier. The size of the diode is compared with that of a conventional pencil point.

One end of the helix was terminated in a matched load and the input VSWR was measured on a reflectometer over the 2000- to 4000-megacycle frequency range. The diodes were spaced at intervals of two, three, and four turns. The periodicity of the low-VSWR regions decreased with decreasing diode spacing from an average of approximately 1000 megacycles for a diode in every fourth turn to about 300 megacycles for a diode in every second turn. Figure 9 shows the VSWR with diodes positioned in every second turn. The several match ranges in the 2000- to 4000-megacycle frequency range include a relatively broad band of very low VSWR in the 2200- to 2300-megacycle range, and a narrower band of very low VSWR near 3000 megacycles. Small shifts in diode position and spacing produced substantial shifts in the frequency locations of these ranges of low VSWR.

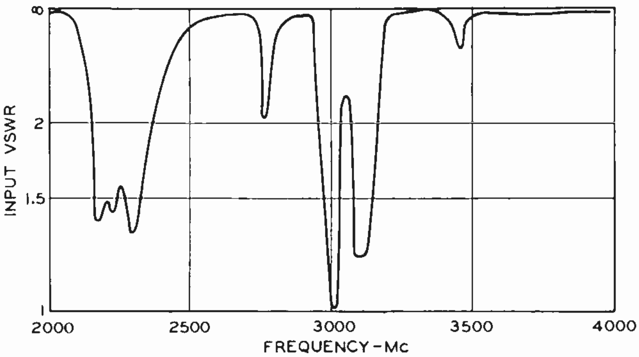

Fig. 9—Input VSWR as a function of frequency for the helix structure of Figure 7 with the structure periodically loaded by three diodes and $\alpha = 0.5$

The curves of Figure 10 show insertion-loss measurements on the diode-loaded helix structure of Figure 7 under conditions of no diode loading, a single diode loading per one helix turn, and diodes loading alternate turns. The unloaded helix has an insertion loss of from one to six decibels over the entire frequency octave from 2000 to 4000 megacycles.

The loading of the helix with a single diode provided only a point of impedance discontinuity and did not constitute periodic loading. For this case, the measured insertion loss generally occurred in the neighborhood of 12 to 15 decibels over the 2000- to 4000-megacycle frequency range. The insertion loss resulting from the insertion of three diodes into the helix (a diode loading alternate helix turns) is shown in Figure 10 for the frequency range 860 to 4000 megacycles. The general configuration of bands having greater and less attenuation is evident; bands of relatively low attenuation occur in the UHF and lower L-band frequency ranges, and a narrow band of very low attenuation occurs near 3000 megacycles. This latter band matches a band of very low VSWR predicted by the VSWR measurement. A relatively high insertion loss of greater than 20 decibels was measured in the 2200- to 2300-megacycle band where a very low input VSWR was observed.

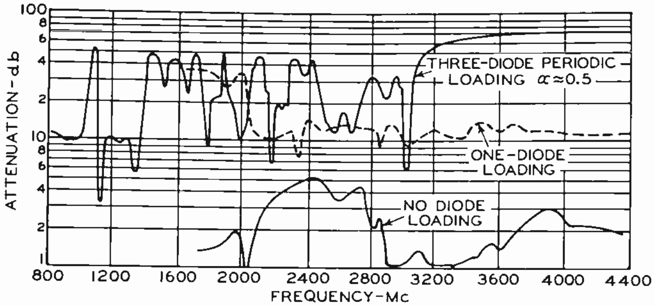

Fig. 10—Attenuation as a function of frequency for the helix of Figure 7 for different loading conditions.

Pass-Band Significance

The attenuation curve of a diode-loaded helix shown in Figure 10 provides an important key to the understanding of the helix parametric amplifier. The particular periodic loading used results in a relatively narrow pass band of low insertion loss at approximately

3000 megacycles and at 6000 megacycles (not shown in Figure 10). These pass bands have been found experimentally to present an excellent load to signals applied to the helix at 3000 megacycles, with the result that such signals develop considerable voltages across each of the diodes. In fact, sparks have been observed between the diodes and helix turns in very dim light (when the contacts between these elements were broken) with r-f power of several hundred milliwatts applied to the helix in the band. Considerable radiation has been detected at a distance from the unshielded helix. The dissipative qualities of the structure are indicated by the fact that less than 10 milliwatts of r-f power was detected at the output of the helix when almost one watt of net power was applied to the input of the helix. The diode-loaded helix also acted as a harmonic generator at these frequencies with an input signal at 3000 megacycles delivering power at 6000 megacycles in the output with good conversion efficiency.

It has been determined experimentally that, at high gain, parametric amplification is possible when the pump signal is passed through the highest-frequency pass band and the signal and idler frequencies are approximately 70 and 30 per cent, respectively, of the pump frequency, provided that suitable pass bands are developed by the diode-loaded helix at these frequencies. The location of the highest pass band and the pass bands used for the signal and idler frequencies can be controlled by (1) variation of the spacing between diodes (and thus of α), (2) use of an asymmetrical spacing if the helix diameter and pitch are maintained constant, or (3) adjustment of the helix parameters to provide a mechanical means for adjusting the frequency of operation over a range comprising a substantial portion of an octave.

Substantial insertion loss has been encountered in the frequency bands used for the signal frequency, but considerably less at the idler frequencies. Even in favorable transmission bands, the diode-loaded helix, unlike the shunt-loaded transmission line, provides a complex coupled band-pass-filter type of circuit[16,17] in each pass band. The diode-loaded turns present series components of high impedance in cascade to the signals traveling along the helix. This arrangement provides improved impedance matching to each diode over wide frequency ranges because the helix turn shunting each element is a broadband circuit which enhances the signal development to the diodes at the principal frequencies. As a result, high gain is achieved with a very small number of diodes and circuit elements.

EXPERIMENTAL HELIX PARAMETRIC AMPLIFIERS

Two experimental helix parametric amplifiers are shown in Figure 11. Two couplings are made to each side of the portion of the helix where the diode loading takes place, one by direct connection and the other by means of a helical-coupler.

The helical coupler in the helix parametric amplifier simplifies the technique of multiple-signal coupling to and from the helix because (1) it is a very small structure, (2) it may be coupled to a helix over a range of several frequency octaves, and (3) it is basically a directional coupler. This type of coupler is widely used in traveling-wave tubes[18] because of its excellent low-VSWR coupling characteristics. In the helix parametric amplifier, it couples the pump and input signals to the helix with a great degree of mutual signal isolation. In addition, it provides a versatile output circuit for the multiple processing of the output pump signal, amplified input signal, and idler signal, although its insertion loss is higher than that of waveguide or coaxial-cavity couplers.

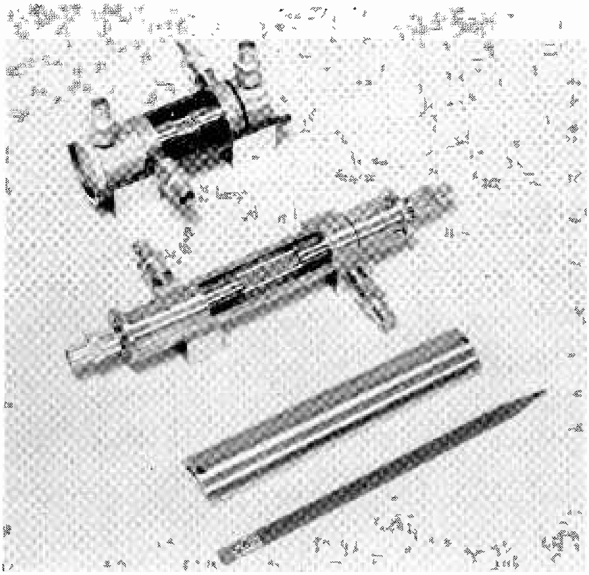

Fig. 11—The sizes of two experimental helix parametric amplifiers compared with that of a conventional pencil.

The helix parametric amplifiers shown in Figure 11 use diode-loaded helix structures which are substantially the same as the structure shown in Figure 7. The use of a helix of fixed size and characteristics, on which different numbers of diodes are positioned for optimum signal-frequency gain characteristics, has resulted in optimum terminal-to-terminal net gains in excess of 20 decibels for all signal frequencies from 1800 megacycles to 3000 megacycles. The pump frequencies used for the extreme and median frequencies were as follows:

Signal Frequency (Mc)	*Pump Frequency* (Mc)
1800	2400
2250	3000
2800	3800

A high degree of precision is required in the circuit elements. As in the traveling-wave tube, minute eccentricities in pitch of the helix can produce substantial changes in the transmission characteristics of the helix. The design of the helical coupler imposes very close tolerances on all parameters. These tolerances are necessary to maintain coupling in frequency bands located many hundreds of megacycles apart.

In general, three diodes were employed for most broad-band experiments. Values of α, the ratio of the electrical angle of the diode-loaded helix turn to the total electrical angle of one cell of the periodic structure, were chosen to give amplification in the 1800- to 2800-megacycle frequency range.

Neither the number of diodes nor their positioning was arbitrary. In the absence of any diodes on the helix, the insertion loss was less than 5 decibels from the input helical coupler to the output helical coupler at the input-signal frequency. A single diode-loaded turn increased this insertion loss to a value in excess of 12 decibels; however, the gain furnished by this single diode when the pump signal was applied, just overcame this insertion loss. When two properly spaced diodes were used, the cold insertion loss was increased. The maximum gain, on application of pump signal, was of the order of 10 decibels from input terminal to output terminal.

The use of three diodes properly positioned in selected turns produced a cold insertion loss of up to 30 decibels. The application of pump energy resulted in up to 40 decibels of net terminal-to-terminal gain in stable operation.

More than three diodes in a periodic array produced special gain characteristics in narrow frequency bands, but no determinable advantage with respect to maximum or wide-band gain. The bulk of the pump power was dissipated by the first three diodes; extra diodes produced additional cold insertion loss but contributed very little gain in the parametric amplification process.

The scope of the program did not permit a full-scale evaluation of optimum diode characteristics for the helix parametric amplifier, although optimum characteristics undoubtedly exist for each helix design frequency range, and desired gain–bandwidth product. On the other hand, the operation of the helix parametric amplifiers was not dependent on critical diode characteristics. Germanium diodes having cutoff frequencies ranging from 60000 to 90000 megacycles and capacitances of 0.25 to 1.0 picofarad could often be interchanged with only small resultant changes in gain. On the other hand, attempts to use diodes with cutoff frequencies of less than 50000 megacycles resulted in substantial reductions in gain.

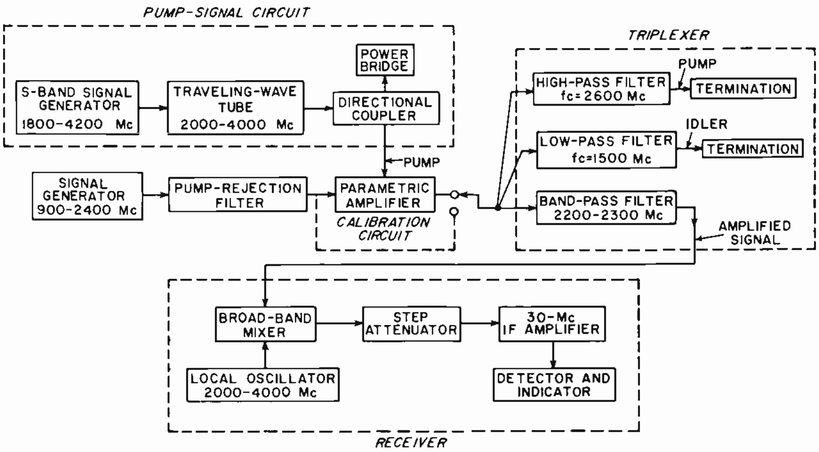

Fig. 12—Block diagram of the circuit used for testing the gain characteristics of a helix parametric amplifier for the frequency band 2200 to 2300 megacycles.

TEST CIRCUIT

The circuit aspects of the helix parametric amplifier are based on a straightforward requirement. Because both input and pump signals are applied to the inputs of the amplifier, an amplified input signal, a pump signal of reduced intensity, and an idler signal are produced in the output of the amplifier. *These three output signals must be terminated in proper impedances.*

Figure 12 shows the basic circuits and components of a test arrangement for gain measurement over the 2200- to 2300-megacycle frequency band. The input signal is applied from a tunable signal generator through a low-loss pump-rejection filter to the amplifier input. The pump signal is supplied to the amplifier by a tunable signal generator which drives a traveling-wave tube and provides pump power of up to one watt variable over the 2000- to 4000-megacycle frequency band.

The output circuit in Figure 12 is a triplexer-type arrangement. The output of the parametric amplifier feeds into a power divider having three output circuits. One output circuit couples to a band-pass filter which passes the amplified band of frequencies to the mixer of a receiver. The second output is coupled to a high-pass filter which rejects both the amplified input-signal and idler-signal power and couples the remaining power at the pump frequency to a matched termination. The third output is coupled to a low-pass filter having a cutoff frequency between the low-frequency of the idler signal and high frequency of the input signal; a matched termination is provided at the output of the low-pass filter as a termination for the idler signal.

The receiver includes the mixer mentioned above, a local oscillator, a calibrated step attenuator, a 30-megacycle i-f strip, and a detector. Gain is measured by a comparison technique; the detector is first calibrated without the parametric amplifier between the input-signal generator and the power divider and then with the parametric amplifier in the circuit. The calibrated attenuator in the receiver is used to measure power gain.

Several precautions were adopted to assure the validity of gain measurements. First the detector was calibrated while pump power of up to one watt was fed into the triplexer to eliminate spurious mixer responses caused by pump-power leak-throughs; in addition, the filters in the triplexer arrangement were arranged to provide at least 80 decibels isolation between the mixer and the pump termination at pump frequency to prevent pump power from effecting the receiver.

Noise figure was measured at S-band with essentially the same circuit. The output of an AIL-70A noise source was applied to the pump-rejection filter, and a calibrated receiver and Hewlett-Packard 304B noise-figure meter (which also powers the noise source) were substituted for the receiver used in the gain measurements.

GAIN PERFORMANCE IN THE 2200- TO 2300-MEGACYCLE BAND

For evaluation of the helix parametric amplifier as a wide-band amplifier with respect to structure, circuit, and performance characteristics, a signal-frequency in the 2200- to 2300-megacycle band was chosen, and extensive measurements of electrical performance were made. The following discussion of pertinent performance characteristics is derived from these measurements. It must be emphasized, however, that these performance characteristics are intended only to illustrate the basic electrical behavior of the helix parametric amplifier and the relationship between the circuit structure and performance, and not to establish the design of a particular amplifier.

Operation in the 2200- to 2300-megacycle frequency band is consistent with the existence of a pass band in that region, a higher-frequency pass band for the pump in the 3000-megacycle range, and a pass band of relatively low insertion loss in the idler-frequency band of 800 to 900 megacycles. Figure 10 shows the pass- and stop-band characteristics of a helix structure, similar to that shown in Figure 7, when it is loaded by 3 diodes.

In the circuit shown in Figure 12, the band-pass filter in the output circuit passes only the desired 2200- to 2300-megacycle band. The high-pass filter in the output pump circuit has a cutoff frequency of 2600 megacycles, and the low-pass filter in the idler output circuit has a cutoff frequency of 1500 megacycles.

Signal connections to the helix parametric amplifier consist of the input signal and the pump signal which are applied to the input helical coupler and the input direct connection to the helix, respectively. The triplexer output circuit is coupled to the output helical coupler, which was specially designed to couple to the helix at all three principal frequencies. The output direct connection to the helix is coupled to a circuit arrangement which permits a wide choice of match and mismatch terminations at the idler frequency. One advantage of the use of pump and idler signals located in relative proximity to the principal signal frequency is that helical couplers have sufficiently wide frequency-coupling characteristics to couple to the helix at all three of these signals, thereby simplifying the coupling problem.

GAIN CHARACTERISTICS

Gain in the 2200- to 2300-megacycle band is a function of several parameters if the helix characteristics remain fixed. These parameters include pump frequency, pump power, and diode spacing as defined by α, the ratio of the electrical angle of the diode-loaded helix turn to the electrical angle of the entire unit cell in each period. For example, when $\alpha = 0.5$, the diodes are in a row between alternate helix turns.

The gains achieved were very stable for long periods of time with frequent turning on and off of the equipment. In general, the curves for gain as a function of pump power were of the type shown in Figure 4 and evidenced very little tendency toward oscillation.* The broad peak of the curve provides for peak gains with small change over a substantial range of pump power.

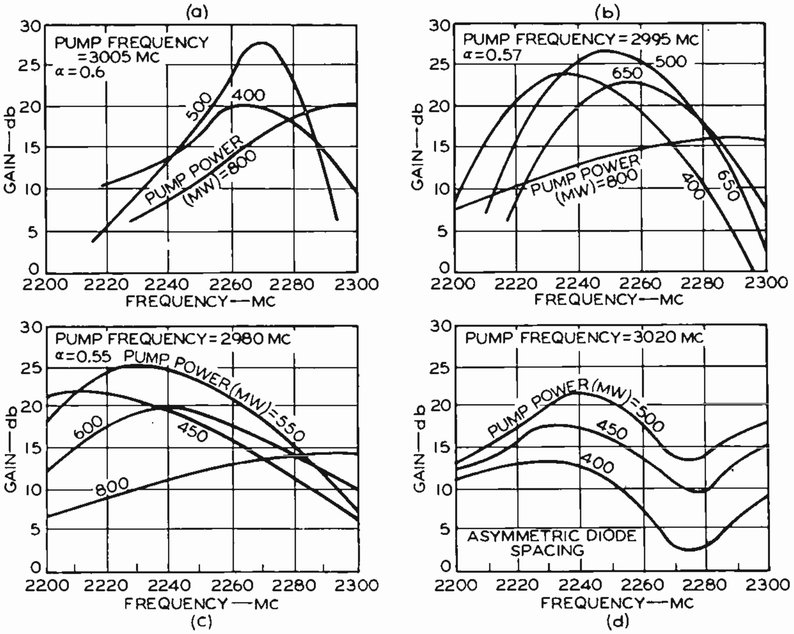

Fig. 13—Gain as a function of frequency for several fixed values of pump power.

Figure 13 shows gain characteristics with respect to various values of pump power for values of α of 0.55, 0.57, and 0.6. These curves do not establish optimum or maximum bandwidth values, but indicate that for a pump power of 500 milliwatts, peak values of more than 20 decibels of gain may be obtained. The gain peaks which are located in various parts of the 2200- to 2300-megacycle frequency band are dependent on the periodic diode-spacing parameter α. No value of α

---

* Oscillations were observed only after prolonged tests at very high pump powers which resulted in the diodes becoming very hot (although not hot enough to cause damage to the diodes); once the diodes cooled, the oscillations disappeared.

shown provides for gain across the entire 100-megacycle band at any value of pump power.

Figure 13(d) shows gain as a function of frequency when the spacing between diodes in the helix turns is made slightly asymmetrical. This condition corresponds in some degree to the staggered tuning used in some intermediate-frequency amplifier strips. The peaked narrow-band gain characteristic typical of the true periodic diode arrangement is replaced by characteristics having lower gains across wider frequency bands. The gain hole at 2275 megacycles is primarily due to the VSWR spike-like increase in the input helical-coupler coupling produced by the asymmetrical diode arrangement.

Each family of curves shown in Figure 13 was measured at a fixed pump frequency; individual curves correspond to significant values of pump power. If the pump frequency is varied until gain is optimized at each signal frequency, the gain characteristics of symmetrical diode-loading arrangements may be broadened. Figure 14, a curve of gain at 15 decibels (at fixed pump power) across the 2200- to 2300-megacycle frequency band as a function of pump frequency, shows that a decrease in pump frequency of the order of 50 megacycles at each end of the band prevents gain drop-off.

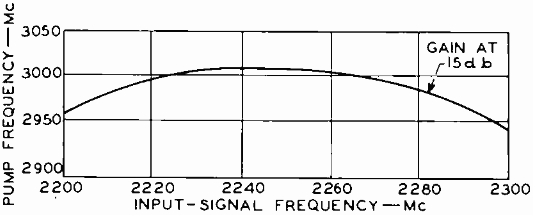

Fig. 14—Locus of pump frequency over the range of signal frequencies from 2200 to 2300 megacycles for a three-diode amplifier operated at 15-decibel gain and with a constant pump power.

Figure 15 shows parametric-amplifier amplification as a function of pump frequency and pump power at the midband frequency of 2250 megacycles for both the symmetrical periodic diode position arrangement and the asymmetrical diode position arrangement; these curves relate to the midband operation shown in Figures 13b and 13c.

As indicated in Figure 15a, the gain for symmetrical diode loading varies as a sin x/x type of function of pump frequency; maximum gain occurs at a pump frequency of 2995 megacycles, the peak of the principal lobe. Gain as a function of pump power at 2995 megacycles follows the general curve of Figure 4. In this curve the gain decreases as pump power increases beyond 600 milliwatts.

For asymmetrical diode loading (see Figure 13d), substantial gain can be achieved at a number of closely spaced pump frequencies. The gain is stable at each of these frequencies, as evidenced by the curves shown in Figure 15d.

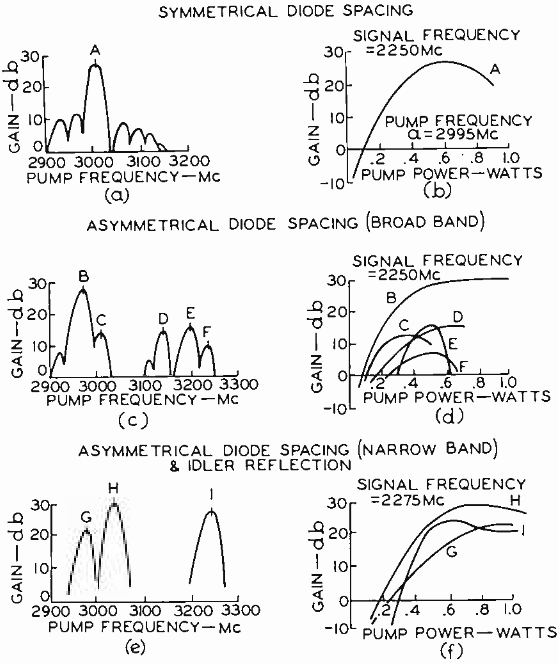

Fig. 15—Gain as a function of frequency and pump power for both symmetrical and asymmetrical diode spacing.

A reflection technique was used to study idler-signal information reflected back to the diode-loaded helix structure for regeneration. Prior to installation of a tuning stub on the output direct-connection to the helix, the parametric amplifier was adjusted to a gain of 22 decibels at 2250 megacycles with the idler properly terminated; after installation and tuning of the stub, the gain was increased to 40 decibels with excellent stability.

Asymmetrical positioning of the diodes in the helix and idler-signal reflection also peak the gain into a narrow frequency band. Figures 15e and 15f show the curves for gain as a function of pump frequency and gain as a function of pump power at each significant pump frequency. The asymmetrically positioned diodes were arranged to provide peak gains of 30 decibels at 2275 megacycles. The bandwidth was very narrow, but the amplifier was stable at all significant pump frequencies.

The gain characteristics were measured under small-signal conditions with signal inputs at —30 dbm and less. In general, the 3-diode helix parametric amplifier was saturated at power-output levels of about one milliwatt and depended upon the types of diodes used, the diode arrangement, and the amount of pump power required at the frequency of signal amplification. Figure 16, a typical curve of gain as a function of input-signal strength for fixed pump power and pump frequency, shows amplifier saturation occurring at an output-signal level of approximately one milliwatt and the small-signal gain resulting from input-signal levels below the saturation levels.

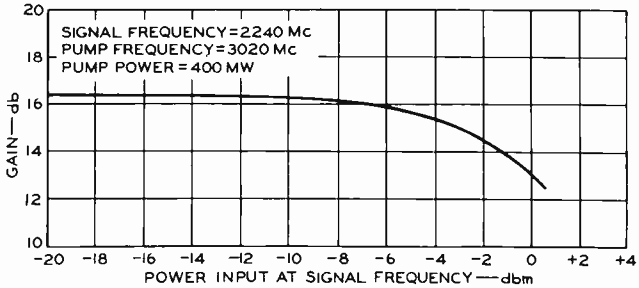

Fig. 16—The gain of an experimental helix parametric amplifier as a function of the input-power level.

NOISE-FIGURE MEASUREMENTS AT 2275 MEGACYCLES

In measuring the noise figure, a 2200-2300 megacycle bandpass filter was used in the output circuit. The measurement was made with the amplifier adjusted to give a gain in excess of 25 decibels at the center frequency (2250 megacycles). The representative curve of gain as a function of pump power shown in Figure 17 was produced at a pump frequency of 3135 megacycles.

The pump rejection filter at the amplifier input stopped noise components at frequencies equal to the pump frequency and at those higher frequencies which beat with the pump signal and produce noise components at 2250 megacycles. In the output circuit, the local oscillator of a receiver driving the noise-figure meter was adjusted to 2280 megacycles. This produced a 30-megacycle component from 2250-

megacycles noise which was amplified in the 30-megacycles receiver i-f strip. However, the image noise of the midband noise at 2310 megacycles was prevented from reaching the mixer by the sharp band-edge characteristics of the 2200- to 2300-megacycle filter.

The curves of noise figure as a function of pump power and gain as a function of pump power for the operating frequencies mentioned above are shown in Figure 17. In regions of low pump power, the noise figure is high; the figure decreases as the pump power is increased to maximum gain. This behavior is similar to that described by R. C. Knechtli and R. D. Weglein.[19] In the maximum-gain region, the terminal noise figure passes through a minimum having a measured value of 4.5 decibels.*

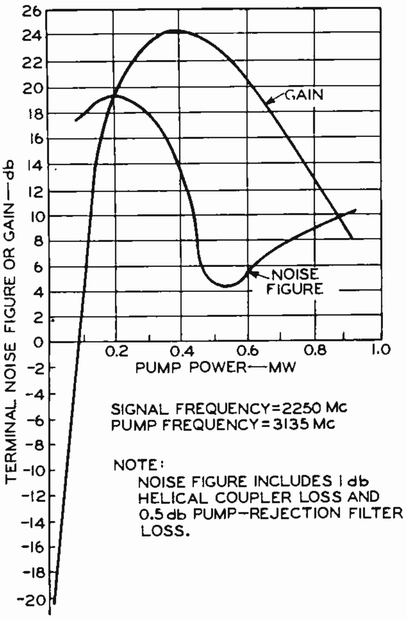

Fig. 17—Noise figure and gain as a function of pump power for a helix parametric amplifier.

As pump power increases beyond the region of maximum gain, the noise figure increases (with decreasing gain). Because the diodes are unbiased in the helix, the point of diode conduction cannot be exactly

---

* This terminal noise figure includes approximately 1.5 decibels insertion loss due to the input helical coupler and the pump-rejection filter.

determined. However, evidence indicates that diode conduction occurs beyond maximum gain.

Figure 17 indicates a useful pump-power range of more than 150 milliwatts in the vicinity of peak gain where terminal noise figures of less than 6 decibels are achieved. This noise figure is in a range of stable gain, and is stable itself because of the noncritical mode of operation at the high-gain crest of the curve shown as a function gain versus pump power.

The terminal noise figure measured at 2275 megacycles represents a noise figure between single-channel and double-channel operation and actually comprises contributions from two modes of operation—the first-harmonic mode of pump power acting on the square-law variation of capacitance charge, and the second-harmonic mode of pump power acting on the cubic variation of capacitance charge. For pure single-channel operation in either mode, all noise components in the idler frequency in each mode must be rejected at the amplifier input; in double-channel operation, all idler-frequency components in each mode must be accepted.

In the first-harmonic mode of pump power, the effective pump frequency is at the applied pump frequency of 3145 megacycles. The idler frequency in that mode, in response to an applied signal at 2275 megacycles, occurs at 860 megacycles. Experiments showed that approximately 8 per cent of the applied signal power was reflected back to the signal generator at the input helical coupler and more than 30 per cent of the idler-frequency power. The noise-figure contribution in this mode, therefore, is approximately 1.1 decibels greater than that for true single-channel operation where 860-megacycle information is completely rejected.

The ultimate single-channel noise-figure contribution (*NF*) in this mode may be calculated from the following equation[2] on the basis of the ratio of signal to idler frequencies when the amplifier is operated at room temperature and high gain:

$$NF \approx 1 + \frac{\omega_s}{\omega_L}$$

where ω_s and ω_L represent the signal and idler frequencies, respectively. For the frequencies under consideration,

$$NF \cong 1 + \frac{2275}{860} \cong 3.65$$

$$\cong 5.62 \text{ decibels.}$$

This is greater than the value measured.

Because of the high pump power of almost one-half watt required for maximum gain and minimum noise figure, however, it appears that the amplifier is operating primarily in the mode where the second harmonic[20] of the pump signal is the effective amplifier pump. In this mode, the idler-signal components occur at the difference between the second harmonic of the pump signal and the input-signal frequency (3995 megacycles). The minimum theoretical noise figure for the amplifier is then approximately

$$NF \cong 1 + \frac{2275}{3995} \cong 1.568$$

$$\cong 1.95 \text{ decibels.}$$

Thus, the total noise figure of 4.5 decibels is primarily the result of contributions of the second-harmonic mode of pump operation and includes losses due to the input circuit, helix losses, and losses in the diode. The noise-figure contribution due to the second-harmonic mode of operation is single-channel because noise components at the idler frequency in this mode of operation are entirely rejected by the pump rejection filter.

WIDE-FREQUENCY-RANGE GAIN CHARACTERISTICS

The 3-diode helix parametric amplifier was tested for gain over frequency ranges other than the 2200- to 2500-megacycle band. A helix of the same size and number of turns per inch was used, but the diodes were positioned differently. Measurements of gain over the 2650- to 2750-megacycle band with fixed pump frequency and pump power indicate the promising capabilities of an amplifier using this helix as a wide-range mid-S-band amplifier.

Two arrangements of three diodes corresponding to an α of about 0.4 provided the curves shown in Figure 18.

Approximately 30 decibels of cold insertion loss was present between input and output terminals before application of fixed values of pump power at fixed frequencies of 2338 and 2348 megacycles. The net gain curves represent the large total electronic gains which overcome the cold insertion loss and provide the net terminal-to-terminal gains. These gain curves represent gain peaking at 1810 megacycles, and the best average point-to-point gain over the entire 10 per cent frequency band. The gain was stable at all frequencies in the frequency range shown in Figure 18.

GAIN TESTS USING MORE THAN THREE DIODES

Amplifier tests were made with a diode-loaded helix using four and five diodes in the 1800-megacycle frequency range. The four-diode arrangement was pumped at 2310 megacycles, the five-diode arrangement at 2658 megacycles. With both the four- and five-diode arrangements, gain of 12 to 14 decibels was achieved at 1800 megacycles with pump power of 250 milliwatts and a pump frequency of 1760 megacycles. The 4-diode arrangement provided 24-decibel net gain with a pump power of only 125 milliwatts at a pump frequency of 2435 megacycles. In all cases, the frequency band over which this gain could be maintained was only a few megacycles wide; however, the pump power was lower than that required for the same gain when three diodes were used.

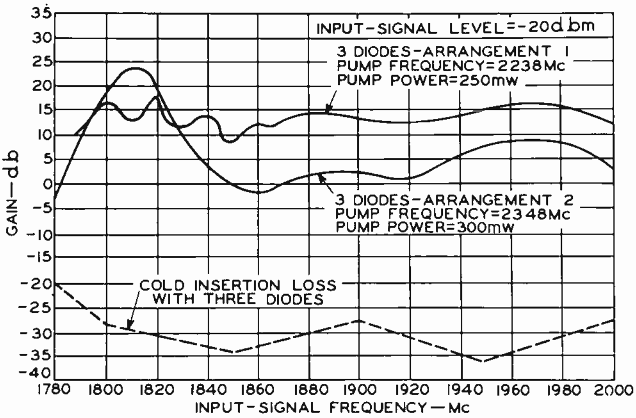

Fig. 18—Gain and cold insertion loss as a function of frequency of a three-diode helix parametric amplifier for two arrangements of the three diodes. The cold-insertion-loss curve is a generalized curve with variations with frequency omitted.

PUMP FREQUENCY, POWER, AND GAIN STABILITY

In general, the experimental helix parametric amplifiers tested have not been self-oscillatory at any pump frequency or power, except under conditions of severe output-circuit mismatch. This tendency to remain nonoscillatory persisted in all modes of operation tested, including modes requiring as much as one watt and as little as 2.5 milliwatts of pump power for substantial gains, and during operation at pump frequencies in pass-bands other than those providing maximum gain characteristics.

The characteristic behavior of the helix parametric amplifier (gain rising to a peak and then decreasing with increasing pump power) is due to many factors. The principal cause is that the diodes start conduction near the peak gain condition. This effect results in increased diode conduction and increased resistance shunting of the diode-loaded helix turns as pump power is increased.

However, the absence of self-oscillation, even at electronic gains as high as 70 decibels, is due to the nonreciprocal nature of the device. With the particular coupler arrangements used, the amplifier is not reversible; that is, the inputs and outputs cannot be interchanged without severe deterioration in gain.

ACKNOWLEDGMENT

The authors gratefully acknowledge the cooperation of C. Mueller of RCA Laboratories, who supplied the diodes for this investigation, and the support and encouragement of H. K. Jenny and R. G. Talpey in this unconventional approach to the study of parametric amplifiers. In addition, the authors acknowledge helpful discussions with J. J. Napoleon, R. E. Johnson, G. Heilmeier, J. Hilibrand, and L. S. Nergaard covering many aspects of amplifier design and operation.

REFERENCES

[1] H. Suhl, "Proposal for a Ferromagnetic Amplifier in the Microwave Range," *Phys. Rev.*, Vol. 106, p. 384, April 1957.

[2] S. Bloom and K. K. N. Chang, "Theory of Parametric Amplification Using Nonlinear Reactances," *RCA Review*, Vol. 18, p. 578, December 1957.

[3] L. S. Nergaard, "Nonlinear-Capacitance Amplifiers," *RCA Review*, Vol. 20, p. 3, March 1959.

[4] A. L. Cullen, "A Traveling-Wave Parametric Amplifier," *Nature*, Vol. 181, p. 332, February 1, 1958.

[5] P. K. Tien and H. Suhl, "A Traveling-Wave Ferromagnetic Amplifier," *Proc. IRE*, Vol. 46, p. 700, April 1958.

[6] R. S. Engelbrecht, "A Low Noise Nonlinear Reactance Traveling-Wave Amplifier," *Proc. IRE*, Vol. 46, p. 1655, September 1958.

[7] C. V. Bell and G. Wade, "Circuit Considerations in Traveling-Wave Parametric Amplifiers," 1959 *IRE WESCON Record*, Pt. 2.

[8] G. Heilmeier, "An Analysis of Parametric Amplification in Periodically Loaded Transmission Lines," *RCA Review*, Vol. 20, p. 442, September 1959.

[9] R. C. Honey and E. M. T. Jones, "A Wide-Band UHF Traveling-Wave Variable Reactance Amplifier," *IRE Transaction on Microwave Theory and Techniques*, Vol. MTT-8, p. 351, May 1960.

[10] K. P. Grabowski, R. D. Weglein, and M. R. Currie, "S-Band Traveling-Wave Parametric Amplifier Using a Filter Circuit," *Trans. IRE PGED*, Vol. ED-7, p. 115, April 1960.

[11] K. K. N. Chang, G. Conrad, and R. Hughes, "The Diode-Loaded Helix as a Microwave Amplifier," *Proc. IRE*, Vol. 48, p. 939, May 1960.

[12] W. J. Dodds and R. W. Peter, "Filter-Helix Traveling-Wave Tube," *RCA Review*, Vol. 14, p. 502, December 1953.

[13] W. J. Dodds, R. W. Peter, and S. F. Kaiser, "New Developments in Traveling Wave Tubes," *Electronics*, Vol. 20, p. 130, February 1953.

[14] A. E. Siegman and H. R. Johnson, "Suppression of Backward-Wave Oscillation by Filter Helix Methods," *Trans. IRE PGED*, Vol. ED-2, p. 20, April 1955.

[15] C. W. Mueller, C. F. Stocker, J. Hilibrand, and R. D. Gold, "Parametric Diodes for Ultra-High Speed Computers," *Trans. IRE PGED*, Vol. ED-7, p. 111, April 1960.

[16] B. D. H. Tellegen, "Coupled Circuits," Philips Research Reports, 1-19, Vol. 2, p. 1, February 1947.

[17] M. Dishal, "Design of Dissipative Band-Pass Filters Producing Desired Exact Amplitude-Frequency Characteristics," *Proc. IRE*, Vol. 37, p. 1050, September 1949.

[18] C. L. Cuccia, "Lightweight Very-Wide-Band Integral Package TWT's," *Microwave Journal*, Vol. 3, p. 47, July 1960.

[19] R. C. Knechtli and R. D. Weglein, "Low Noise Parametric Amplifier," *Proc. IRE*, Vol. 48, p. 1218, July 1960.

[20] K. K. N. Chang and S. Bloom, "A Parametric Amplifier Using Lower-Frequency Pumping," *Proc. IRE*, Vol. 46, p. 1383, July 1958.

OPTIMUM BAND SHAPE FOR TELEVISION INTERMEDIATE-FREQUENCY AMPLIFIER*

By

T. MURAKAMI†

Summary—*In a phase-linearized television intermediate-frequency amplifier, the optimum bandshape is "haystack" or parabolic. With this type of bandpass characteristic, the system transient response to a stepped carrier has a single precursory undershoot and a single overshoot with no associated transient ringing. In such a system, the optimum carrier position is approximately at the 40 per cent response point on the selectivity curve.*

INTRODUCTION

BOTH theoretical and experimental results have shown that a linear phase system exhibits a symmetrical transient response with the fastest possible rise time for a given amplitude characteristic.[1] The purpose of this paper is to determine the optimum amplitude characteristic and the optimum carrier position for a phase-linearized television-receiver i-f amplifier. In the past, it has generally been assumed that the ideal receiver attenuation (RA) curve for vestigial sideband (VSB) transmission of a television signal is the standard RA characteristic.[2] However, this type of bandshape results in considerable transient ringing of the response envelope before and after the input-carrier amplitude transition.

Before determining the optimum i-f bandshape, consideration will be given to the transient response of a system with the standard RA characteristic. A parabolic bandpass characteristic is then analyzed to show the effect of departing from the standard RA curve and normal carrier position. The low-pass/bandpass analogy[3] is then de-

---

* Manuscript received 23 May 1960.

† Formerly, of RCA Home Instruments Division, Camden, N.J.; presently with RCA Defense Electronic Products Division, Moorestown, N.J.

[1] T. Murakami and Murlan S. Corrington, "Applications of the Fourier Integral in the Analysis of Color Television Systems," *IRE Trans. Circuit Theory*, Vol. CT-2, No. 3, p. 250, September, 1955.

[2] G. E. Anner, *Elements of Television Systems*, p. 460, Prentice-Hall, Inc., New York, 1951.

[3] T. Murakami and R. W. Sonnenfeldt, "Transient Response of Detectors in Symmetric and Asymmetric Sideband Systems," *RCA Review*, Vol. 16, p. 580, December, 1955.

rived on a simplified basis and used to determine the optimum i-f bandshape from a special low-pass system with the desired transient response.

RESPONSE TO STEPPED CARRIER OF VSB SYSTEM WITH STANDARD RA CURVE

The standard RA characteristic as shown in Figure 1 consists of region 1 where parts of both sidebands are present, and region 2 where only the upper sideband is present. If the system phase function is assumed to be linear with frequency in the ideal case, the response to a suddenly applied sine wave can be expressed as (see Appendix I)

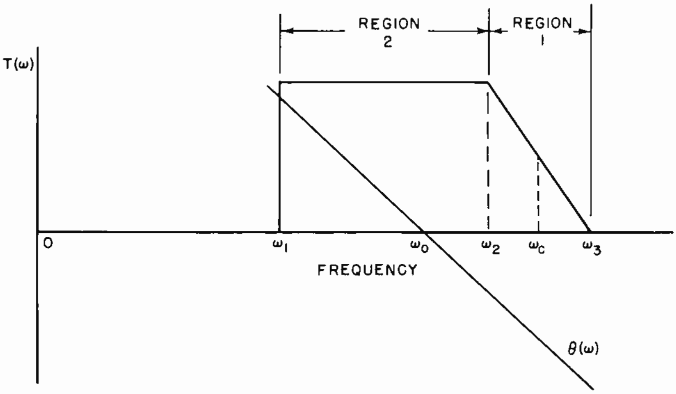

Fig. 1—Standard RA transmission curve.

$$R(t) = \operatorname{Im} \left(\exp \{j\omega_c t\}[P(t) + jQ(t)]\right), \tag{1}$$

where
$$P(t) = \frac{1}{4} + \frac{1}{2\pi} \operatorname{Si} (\omega_c - \omega_1) t, \tag{2}$$

$$Q(t) = \frac{1}{2\pi} \left(\frac{2 \sin (\omega_3 - \omega_c) t}{(\omega_3 - \omega_2) t} + \operatorname{Ci} (\omega_1 - \omega_c) t - \operatorname{Ci} (\omega_2 - \omega_c) t \right), \tag{3}$$

and Im (x) indicates the imaginary part of x. ω_c is the carrier frequency and the delay t_d is omitted in these equations, and Si (x) and Ci (x) are defined by

$$\operatorname{Si} (x) = \int_0^x \frac{\sin t}{t} dt$$

$$\mathrm{Ci}\ (x) = \int_x^\infty \frac{\cos t}{t}\, dt.$$

Equations (2) and (3) have been plotted in Figure 2 along with the envelope function for the frequencies indicated in Figure 1. It is noted that the inphase component, $P(t)$, could be recovered by the use of a product detector. $P(t)$ is of the same form as the step response of an ideal "brickwall" low-pass system. With 100 per cent modulation of the carrier, the envelope is made quite unsymmetrical by the vector addition of the quadrature component to the inphase component. When the modulation index, m, is small, the envelope distortion will also be small. If the input carrier is stepped from a finite level instead of from zero, the output envelope may be written

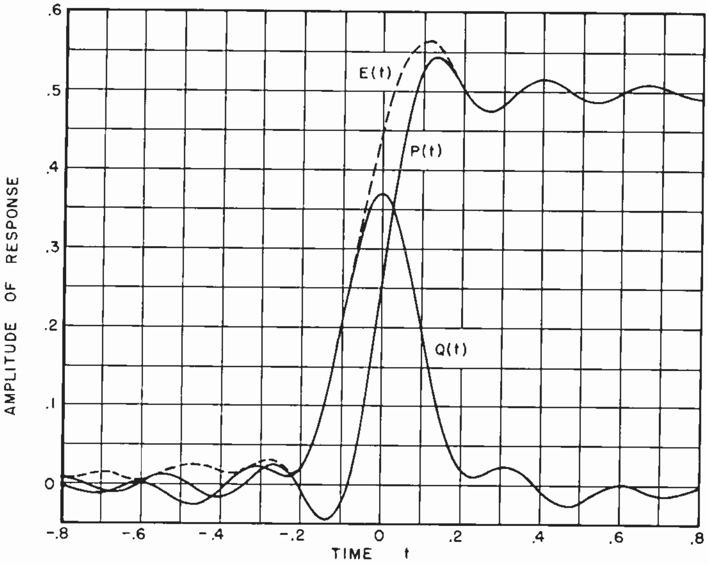

Fig. 2—Envelopes of carrier output from ideal VSB bandpass system with step of carrier applied at 50 per cent point.

$$E(t) = |(1-m)T(\omega_c) + m[P(t) + jQ(t)]|, \tag{4}$$

where $T(\omega_c) = 0.5$ for the ideal VSB case. For this particular example, let the input carrier be suddenly changed in amplitude from 0.5 to 1.0 so that $m = 0.5$. The detected output is as shown in Figure 3 for the envelope, inphase, and quadrature component detectors. Less distortion is noted in the envelope than in the previous case where the modulation was 100 per cent, the envelope being very similar to the inphase component.

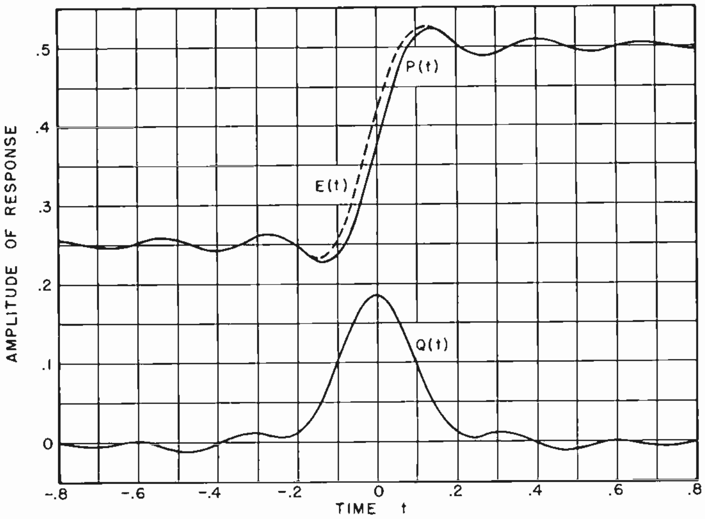

Fig. 3—Envelopes of carrier output from ideal VSB bandpass system with 50 per cent step-modulated carrier applied at 50 per cent point.

RESPONSE OF PARABOLIC BANDPASS SYSTEM TO SUDDENLY APPLIED CARRIER

To show the effect of the band shape and carrier position on a linear phase system, let us consider the parabolic bandpass system shown in Figure 4. The amplitude function shown in Figure 4 is represented by

$$T(\omega) = 1 - \left(\frac{\omega - \omega_0}{\omega_2 - \omega_0}\right)^2, \tag{5}$$

where $\omega_1 \leqq \omega \leqq \omega_2$ and $\omega_0 = (\omega_1 + \omega_2)/2$. The response to a suddenly applied carrier as shown in Appendix II can be written in the form of Equation (1), where

$$P(t) = \frac{1}{2}\left[1 - \left(\frac{\omega_c - \omega_0}{\omega_2 - \omega_0}\right)^2\right]\left[1 + \frac{1}{\pi}\left[\mathrm{Si}\ (\omega_2 - \omega_c)t - \mathrm{Si}\ (\omega_1 - \omega_c)t\right]\right]$$

$$+\frac{1}{2\pi t(\omega_2-\omega_0)^2}\left[(\omega_c-\omega_1)\cos(\omega_2-\omega_c)t + (\omega_2-\omega_c)\cos(\omega_1-\omega_c)t\right]$$

$$-\frac{1}{2\pi t^2(\omega_2-\omega_0)^2}\left[\sin(\omega_2-\omega_c)t-\sin(\omega_1-\omega_c)t\right] \qquad (6)$$

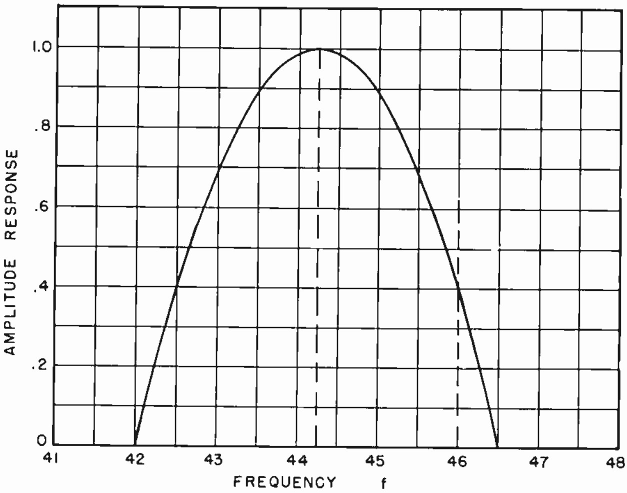

Fig. 4—Parabolic bandpass system ($\omega_1 = 42$ mc, $\omega_0 = 44.25$ mc, $\omega_c = 46$ mc, and $\omega_2 = 46.5$ mc).

and $$Q(t) = -\frac{1}{2\pi}\left[1-\left(\frac{\omega_c-\omega_0}{\omega_2-\omega_0}\right)^2\right]\left[\mathrm{Ci}\,(\omega_2-\omega_c)t-\mathrm{Ci}\,(\omega_1-\omega_c)t\right]$$

$$+\frac{1}{2\pi t(\omega_2-\omega_0)^2}\left[(\omega_c-\omega_1)\sin(\omega_2-\omega_c)t + (\omega_2-\omega_c)\sin(\omega_1-\omega_c)t\right]$$

$$+\frac{1}{2\pi t^2(\omega_2-\omega_0)^2}\left[\cos(\omega_2-\omega_c)t-\cos(\omega_1-\omega_c)t\right]. \qquad (7)$$

Equations (6) and (7) have been plotted in Figure 5 along with the envelope function for

$\omega_2 - \omega_c = \pi$ $\omega_2 - \omega_0 = 4.5\pi$

$\omega_c - \omega_1 = 8\pi$ $\omega_c - \omega_0 = 3.5\pi$

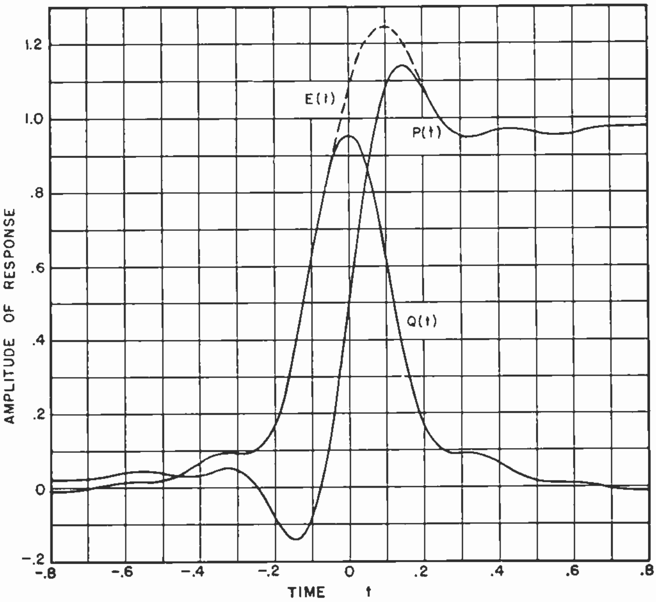

Fig. 5—Normalized envelopes of output from parabolic bandpass system with step-modulated carrier applied at 39.5 per cent point.

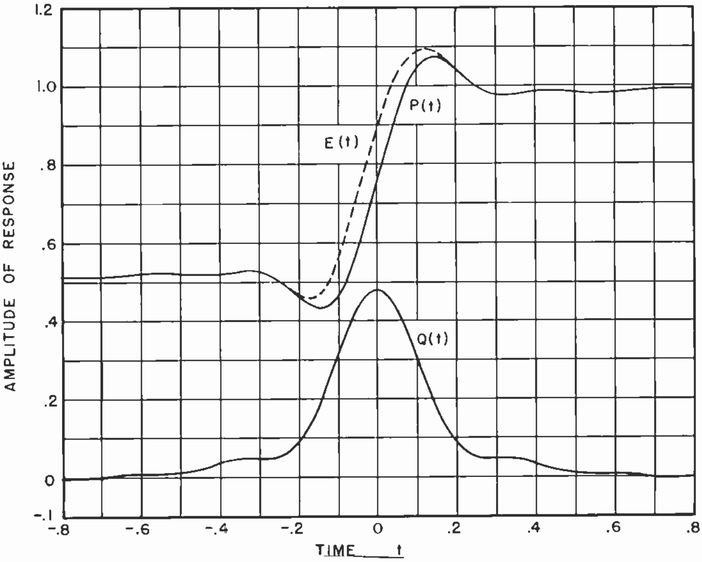

Fig. 6—Normalized envelopes of output from parabolic bandpass system with 50 per cent step-modulated carrier applied at 39.5 per cent point.

where the carrier is applied at approximately the 40 per cent response point. The curves shown in Figure 5 have been normalized to unit amplitude by dividing the response by the steady-carrier amplitude. Considerable asymmetry is developed in the envelope of the output carrier. The curves in Figure 5 correspond to a 100 per cent modulated carrier; for smaller percentages of modulation, the wave shape of the envelope will approach that of the inphase component. This is illustrated by the curves of Figure 6 which are for a 50 per cent modulated carrier. The single preshoot and overshoot obtained in the transient response for this band shape is desirable in television since it enhances the picture quality.

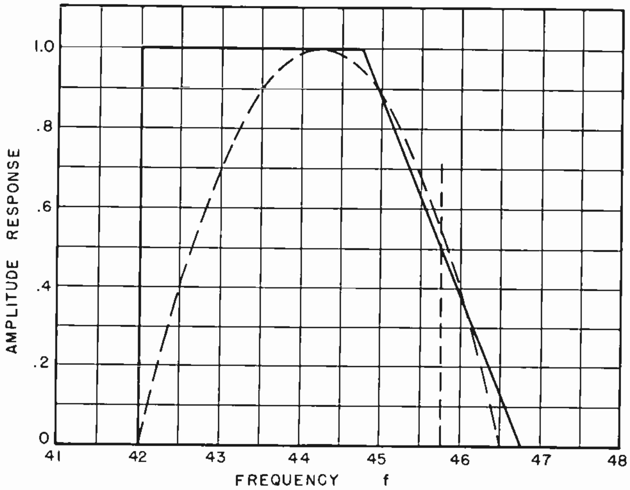

Fig. 7—Ideal VSB bandpass system.

It is of interest to compare the band shapes and transient responses of the standard idealized RA characteristic and the parabolic bandpass system. Inspection of Figure 7, which shows both characteristics, reveals that the standard RA curve has a 3-decibel bandwidth which is about 40 per cent greater than that for the parabolic band shape. However, a comparison of the rise times of the inphase components shows that they are equal. The reason for the improved bandwidth–rise-time ratio obtained with the parabolic band shape is the high-frequency peaking resulting from the parabolic band shape and operation with the carrier below 50 per cent. This fact will be more evident after the discussion of low-pass/bandpass analogs in the following sections.

When the carrier position is changed so that the amplitude response at the carrier frequency is .50, the normalized response to a suddenly applied carrier is as shown in Figure 8. The amplitude of both the overshoot and the quadrature component is decreased as the carrier is moved toward the center frequency of the pass band. With a 50 per cent step-modulated carrier, the envelope of the output carrier approaches the inphase component as illustrated by Figure 9. Figures 10 and 11 show the corresponding envelopes of the output carrier when the carrier is placed at the 60 per cent response point on the bandpass characteristic. It is noted that the precursory and following overshoots are greatly decreased in amplitude.

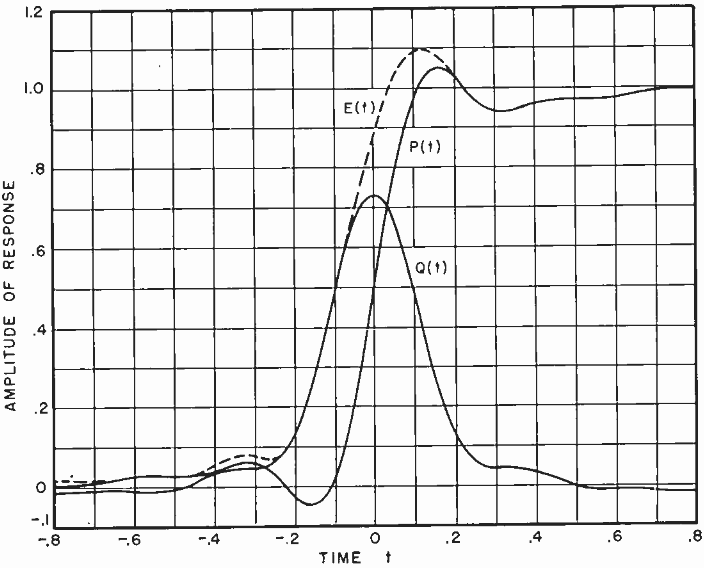

Fig. 8—Normalized envelopes of output from parabolic bandpass system with step-modulated carrier applied at 50 per cent point.

LOW-PASS/BANDPASS ANALOG FOR ASYMMETRICAL SIDEBAND SYSTEM

By use of the low-pass/bandpass analog it is possible to determine the band shape for the bandpass system which results in the most suitable transient response for the television signal. For a symmetrical double-sideband (DSB) system, the equivalent low-pass analog is obtained by shifting the bandpass to the origin so that the carrier position is at zero, as shown in Figure 12(a) and (b). This results

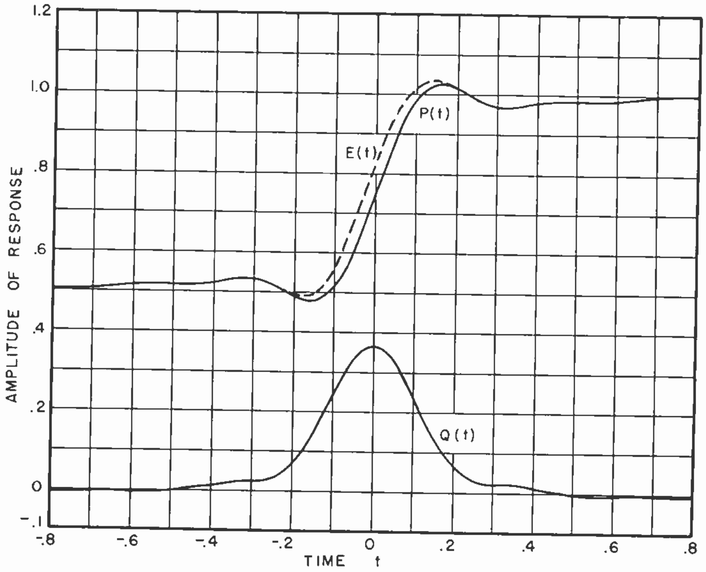

Fig. 9—Normalized envelopes of output from parabolic bandpass system with 50 per cent step-modulated carrier applied at 50 per cent point.

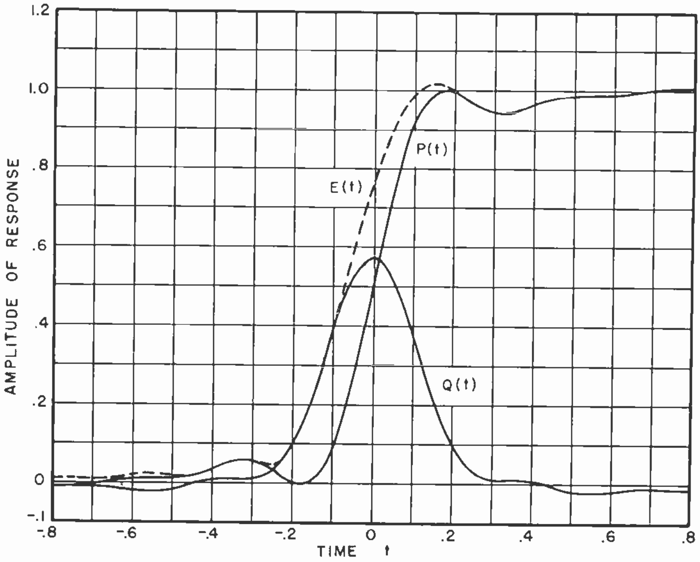

Fig. 10—Normalized envelopes of output from parabolic bandpass system with step-modulated carrier applied at 60 per cent point.

in a low-pass system with the same selectivity as the upper side frequency of the bandpass system.

In an asymmetrical-sideband system there are two analog filters, one for the envelope of the inphase component of the output carrier and the other for the quadrature component of the output carrier. A relatively simple derivation for these analog filters will now be given. Consider the passage of a carrier with sinusoidal amplitude modulation through a transmission system with amplitude and phase characteristics $T_C \exp[j\theta_c]$, $T_U \exp[j\theta_u]$, and $T_L \exp[j\theta_l]$ for the three angular frequencies ω_c, $\omega_c + \omega_m$, and $\omega_c - \omega_m$, respectively, as shown in Figure 13.

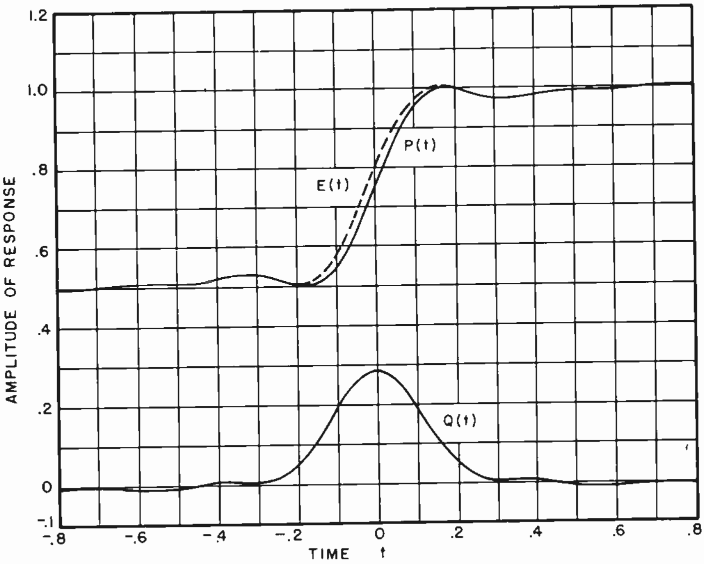

Fig. 11—Normalized envelopes of output parabolic bandpass system with 50 per cent step-modulated carrier applied at 60 per cent point.

Let the amplitude-modulated carrier e_i at the input be

$$e_i = E(1 + m \sin \omega_m t) \sin \omega_c t$$

$$= E\left[\sin \omega_c t + \frac{m}{2} \cos(\omega_c - \omega_m)t - \frac{m}{2} \cos(\omega_c + \omega_m)t\right], \qquad (8)$$

where E is the carrier amplitude and ω_m the modulation frequency.

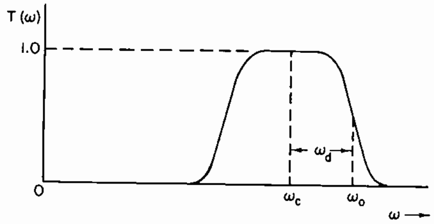

(a) BANDPASS SYSTEM

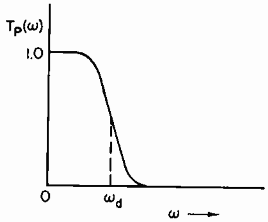

(b) LOW-PASS ANALOG

Fig. 12—Bandpass system and low-pass analog.

Passage through the bandpass system will produce the output wave e_o given by

$$e_o = E\left(T_C \sin\,(\omega_c t + \theta_c) + \frac{mT_L}{2} \cos\,[\,(\omega_c - \omega_m)t + \theta_l] \right.$$
$$\left. + \frac{mT_U}{2} \cos\,[\,(\omega_c + \omega_m)t + \theta_u] \right), \qquad (9)$$

where each frequency component has been modified in amplitude and phase in accordance with the transmission characteristic of Figure 13. Equation (9) can be rewritten as

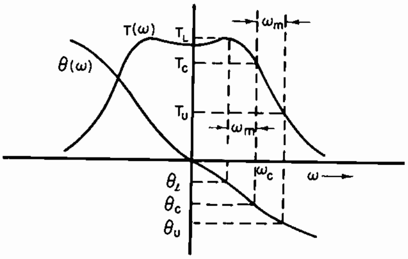

Fig. 13—Transmission characteristic of bandpass system.

$$
\begin{aligned}
e_o = E\,\mathrm{Re}\Bigg(& -jT_C \exp\{j(\omega_c t + \theta_c)\} + \frac{mT_L}{2}\exp\{j[(\omega_c - \omega_m)t + \theta_l]\} \\
& + \frac{mT_U}{2}\exp\{j[(\omega_c + \omega_m)t + \theta_u]\}\Bigg) \\
= E\,\mathrm{Re}\Bigg(& \exp\{j(\omega_c t + \theta_c)\}\left[-jT_C + \frac{mT_L}{2}\exp\{-j(\omega_m t - \theta_L)\}\right. \\
& \left. + \frac{mT_U}{2}\exp\{j(\omega_m t + \theta_U)\}\right]\Bigg) \\
= E\Bigg(& \left[T_C + \frac{mT_L}{2}\sin(\omega_m t - \theta_L) + \frac{mT_U}{2}\sin(\omega_m t + \theta_U)\right] \\
& \sin(\omega_c t + \theta_c) \\
& + \left[\frac{mT_L}{2}\cos(\omega_m t - \theta_L) - \frac{mT_U}{2}\cos(\omega_m t + \theta_U)\right]\cos(\omega_c t + \theta_c)\Bigg)
\end{aligned}
\tag{10}
$$

where $\theta_L = \theta_l - \theta_c$ and $\theta_U = \theta_u - \theta_c$ and $\mathrm{Re}(x)$ indicates the real part of x. The coefficient of $\sin(\omega_c t + \theta_c)$ is the envelope of the inphase component of the output carrier, and the coefficient of $\cos(\omega_c t + \theta_c)$ is the envelope of the quadrature component of the output carrier. The a-c part of the inphase component, $P(t)$, can be expressed as

$$
P(t) = \mathrm{Im}\left[\frac{mT_L}{2}\exp\{j(\omega_m t - \theta_L)\} + \frac{mT_U}{2}\exp\{j(\omega_m t + \theta_U)\}\right].
\tag{11}
$$

It is thus seen that to obtain the envelope of the inphase component of the original modulation,

$$
m \sin \omega_m t = \mathrm{Im}\,[m \exp\{j\omega_m t\}]
\tag{12}
$$

must pass through a system with the transfer function

$$
T_P \exp j\theta_P = \frac{1}{2}\,[T_L \exp(-j\theta_L) + T_U \exp j\theta_U],
\tag{13}
$$

where T_P is the amplitude characteristic and θ_P is the phase characteristic of the equivalent low-pass filter. Equating real and imaginary parts in Equation (13) gives

$$T_P \cos\theta_P = \frac{1}{2}\,(T_U \cos\theta_U + T_L \cos\theta_L) \tag{14}$$

$$T_P \sin\theta_P = \frac{1}{2}\,(T_U \sin\theta_U - T_L \sin\theta_L). \tag{15}$$

Solving Equations (14) and (15) for T_P and θ_P results in the amplitude and phase characteristics of the low-pass analog for the envelope of the inphase component in terms of the characteristics of the bandpass system. Thus

$$T_P = \frac{1}{2}\,[T_U^2 + T_L^2 + 2T_UT_L \cos(\theta_U + \theta_L)]^{1/2} \tag{16}$$

$$\theta_P = \tan^{-1}\frac{T_U \sin\theta_U - T_L \sin\theta_L}{T_U \cos\theta_U + T_L \cos\theta_L}. \tag{17}$$

To obtain the associated analog filter for the quadrature component, the envelope of the quadrature component $Q(t)$, as given by Equation (10), is rewritten in complex form

$$Q(t) = \mathrm{Im}\left(\frac{jmT_L}{2}\exp\{j(\omega_m t - \theta_L)\} - \frac{jmT_L}{2}\exp\{j(\omega_m t + \theta_U)\}\right). \tag{18}$$

The original modulation as given by Equation (12) must, by Equation (18), pass through a system with a transfer function

$$T_Q \exp j\theta_Q = \frac{j}{2}\,[T_L \exp(-j\theta_L) - T_U \exp j\theta_U], \tag{19}$$

where T_Q is the amplitude and θ_Q the phase of the quadrature analog filter. In terms of the bandpass characteristics, T_Q and θ_Q are

$$T_Q = \frac{1}{2} \left[T_U^2 + T_L^2 - 2T_U T_L \cos\,(\theta_U + \theta_L) \right]^{1/2} \tag{20}$$

$$\theta_Q = \tan^{-1} \frac{T_L \cos\theta_L - T_U \cos\theta_U}{T_L \sin\theta_L + T_U \sin\theta_U}\,. \tag{21}$$

LOW-PASS ANALOGS IN LINEAR-PHASE BANDPASS SYSTEMS

When the system phase is linear, so that $\theta_L = -\theta_U$, the low-pass analog characteristics for the inphase component in terms of the bandpass characteristics reduce to

$$T_P = \frac{1}{2}\,(T_L + T_U) \tag{22}$$

and

$$\theta_P = \theta_U = -\theta_L. \tag{23}$$

The corresponding equations for the quadrature filter are then

$$T_Q = \frac{1}{2}\,(T_L - T_U) \tag{24}$$

and

$$\theta_Q = \frac{\pi}{2} + \theta_U. \tag{25}$$

In an asymmetric sideband system where the carrier is placed on the low-frequency side of resonance, T_Q will be negative. For this case $-\pi$ must be added to θ_Q so that T_Q will be positive in agreement with the normal convention for amplitude. Thus

$$\theta_Q = -\frac{\pi}{2} + \theta_U. \tag{26}$$

To show the use of the low-pass analogs, let us apply the analog equations to the standard television RA characteristic shown in Figure 1. In this case, the low-pass analog filter for the inphase component is as shown in Figure 14(a), and the corresponding quadrature-filter characteristic is shown by Figure 14(b) when the carrier is at 50 per cent on the sloping characteristic. It is noted that the phase angle θ_Q is shifted by π as the response passes through zero at the origin.

When a unit step of carrier is applied to the bandpass system, this corresponds to a unit-step function applied to the analog filters. For the inphase component, the response by the Fourier integral is then

$$P(t) = \frac{1}{2\pi} \int_{-\infty}^{\infty} T_P(\omega) G(\omega) \exp \{ j [\omega t + \theta_P(\omega)] \} d\omega, \qquad (27)$$

where

$$T_P(\omega) = 1, \qquad \omega \leqq |\omega_c - \omega_1|$$

$$T_P(\omega) = 0, \qquad \omega > |\omega_c - \omega_1|$$

$$\theta_P(\omega) = -\omega t_d, \qquad \omega \leqq |\omega_c - \omega_1|.$$

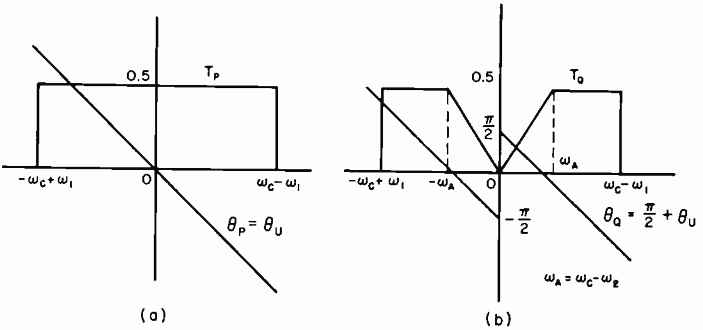

Fig. 14—Low-pass analogs of standard television RA characteristic with carrier at 50 per cent response point.

Using the system characteristics as given above, the response is

$$P(t) = \frac{1}{4\pi j} \int_{-(\omega_c-\omega_1)}^{\omega_c-\omega_1} \frac{\exp\{j\omega(t-t_d)\}}{\omega} d\omega$$

$$= \frac{1}{4} + \frac{1}{2\pi} \operatorname{Si} [(\omega_c - \omega_1)(t - t_d)] \qquad (28)$$

where the steady-state term results from the pole at the origin. Equation (28) is seen to be the same as Equation (2) derived by the normal method in Appendix I. The quadrature component response can be more easily obtained if the system is modified to the equivalent linear phase system shown in Figure 15. The system transfer function is represented by

$$T_Q(\omega) = -0.5 \qquad -(\omega_c - \omega_1) \leqq \omega \leqq -(\omega_c - \omega_2)$$

$$= \frac{\omega}{2(\omega_c - \omega_2)} \qquad -(\omega_c - \omega_2) \leqq \omega \leqq \omega_c - \omega_2$$

$$= 0.5 \qquad \omega_c - \omega_2 \leqq \omega \leqq \omega_c - \omega_1$$

$$\theta_Q = \frac{\pi}{2} - \omega t_d \qquad -(\omega_c - \omega_1) \leqq \omega \leqq \omega_c - \omega_1$$

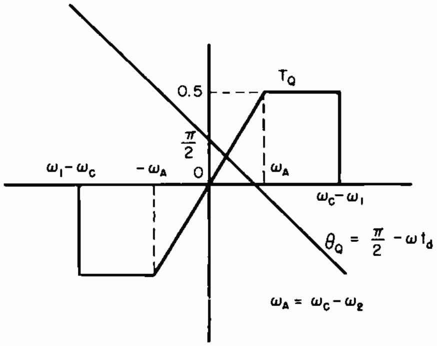

Fig. 15—Equivalent characteristic of quadrature component.

Using the equivalent system characteristics, the response to a unit-step function is

$$Q(t) = \frac{1}{2\pi}\int_{-\infty}^{\infty} T_Q(\omega)G(\omega)\exp\{j\lfloor \omega t + \theta_Q(\omega)\rceil\}d\omega$$

$$= \exp\left\{j\frac{\pi}{2}\right\}\left(\frac{-1}{4\pi j}\int_{-(\omega_c-\omega_1)}^{-(\omega_c-\omega_2)} \frac{\exp\{j\omega(t-t_d)\}}{\omega}d\omega + \frac{1}{4\pi(\omega_c-\omega_2)j}\right.$$

$$\left.\int_{-(\omega_c-\omega_2)}^{\omega_c-\omega_2} \exp\{j\omega(t-t_d)\}d\omega + \frac{1}{4\pi j}\int_{\omega_c-\omega_2}^{\omega_c-\omega_1}\frac{\exp\{j\omega(t-t_d)\}}{\omega}d\omega\right)$$

$$= j\left(\frac{1}{2\pi j}\int_{\omega_c-\omega_2}^{\omega_c-\omega_1}\frac{\cos\omega(t-t_d)}{\omega}\,d\omega\right.$$

$$\left.+\frac{1}{4\pi(\omega_c-\omega_2)j}\int_{-(\omega_c-\omega_2)}^{\omega_c-\omega_2}\cos\omega(t-t_d)\,d\omega\right)$$

$$=\frac{1}{2\pi}\Big(\mathrm{Ci}\,[(\omega_c-\omega_1)(t-t_d)]-\mathrm{Ci}\,[(\omega_c-\omega_2)(t-t_d)]$$

$$+\frac{1}{(\omega_c-\omega_2)(t-t_d)}\sin\,[(\omega_c-\omega_2)(t-t_d)]\Big). \qquad (29)$$

Since $(\omega_3-\omega_2)=2(\omega_c-\omega_2)$, Equation (29) is seen to be equal to Equation (3), which is derived in the Appendix from the bandpass function. The low-pass analog depends upon the carrier position so that general equations for the inphase and quadrature responses cannot be formally written for an arbitrary carrier position.

LOW-PASS ANALOG FOR PARABOLIC BANDPASS SYSTEM

The low-pass analogs for the parabolic bandpass system discussed earlier are obtained by use of Equations (22) to (25). In Equations (22) and (24), the upper-sideband response T_U and the lower sideband response T_L are given by

$$\begin{aligned} T_U &= 1-\left(\frac{\omega_c+\omega_m-\omega_0}{\omega_2-\omega_0}\right)^2, & 0 &\leq \omega_m \leq \omega_2-\omega_c \\ &= 0 & \omega_2-\omega_c &\leq \omega_m \end{aligned} \qquad (30)$$

and

$$\begin{aligned} T_L &= 1-\left(\frac{\omega_c-\omega_m-\omega_0}{\omega_2-\omega_0}\right)^2, & 0 &\leq \omega_m \leq \omega_c-\omega_1 \\ &= 0 & \omega_c-\omega_1 &\leq \omega_m. \end{aligned} \qquad (31)$$

With the carrier on the high-frequency side of the center frequency of the bandpass system, T_U will be zero when $\omega_m=\omega_2-\omega_c$, so that both T_P and T_Q will follow the lower sideband equation as given by Equation (31). Substituting Equations (30) and (31) into Equation (22)

$$T_P(\omega_m) = \frac{1}{2}\left[1 - \frac{\omega_m^2 + (\omega_c - \omega_0)^2}{(\omega_2 - \omega_0)^2}\right] \qquad 0 \leq \omega_m \leq \omega_2 - \omega_c$$

$$= \frac{1}{2}\left[1 - \left(\frac{\omega_c - \omega_m - \omega_0}{\omega_2 - \omega_0}\right)^2\right] \qquad \omega_2 - \omega_c \leq \omega_m \leq \omega_c - \omega_1 \tag{32}$$

for the inphase analog-filter amplitude characteristic. The phase characteristic is linear and is given by Equation (23).

Use of Equation (24) gives the quadrature amplitude characteristic;

$$T_Q(\omega_m) = \frac{2\omega_m(\omega_c - \omega_0)}{(\omega_2 - \omega_0)^2}, \qquad 0 \leq \omega_m \leq \omega_2 - \omega_c$$

$$= \frac{1}{2}\left\{1 - \left[\frac{\omega_c - \omega_m - \omega_0}{\omega_2 - \omega_0}\right]^2\right\}, \qquad \omega_2 - \omega_c \leq \omega_m \leq \omega_c - \omega_1. \tag{33}$$

The corresponding phase characteristic is given by Equation (25). A plot of Equations (32) and (33) are shown in Figure 16 for the various carrier positions treated earlier. It is seen that there is considerable high-frequency peaking in the amplitude of the inphase filter when the bandpass has a parabolic or "haystack" shape and the system is operated with the carrier below the 50 per cent response point. With the carrier at 50 per cent, there is a dip in the inphase response characteristic at a relatively low frequency, and the response again attains the d-c response amplitude at some higher frequency. When the carrier is placed above the 50 per cent response point on the bandpass curve, low-frequency peaking of the inphase analog filter results, as indicated in Figure 16 where the carrier is at 60 per cent.

As indicated in Equation (33), the quadrature analog filter characteristic is linear from the origin to the frequency $\omega_m = \omega_2 - \omega_c$, and then follows the curve for the inphase analog filter.

USE OF LOW-PASS/BANDPASS ANALOGY TO DERIVE BANDPASS SYSTEM

A linear-phase low-pass system with amplitude characteristics such as those shown in Figure 17 has a desirable transient response for television application. The amplitude characteristics shown in Figure 17 are mathematically represented by

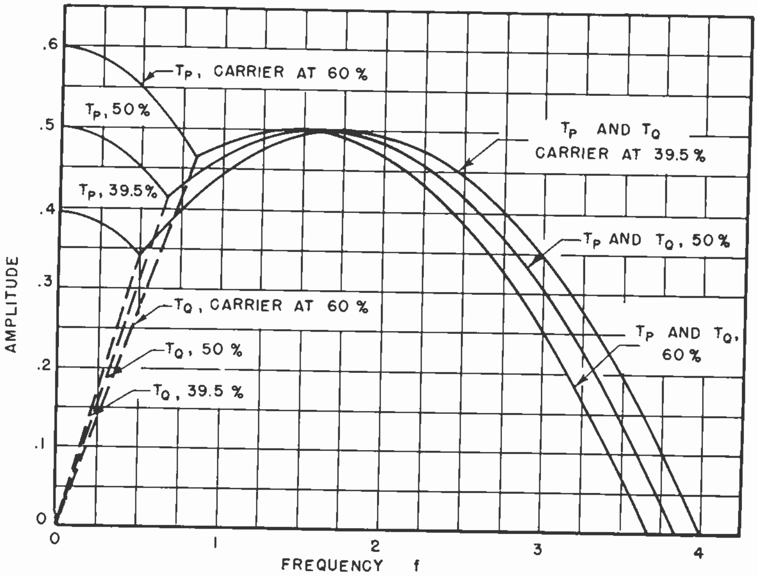

Fig. 16—Low-pass analogs for parabolic bandpass system under vestigial operation.

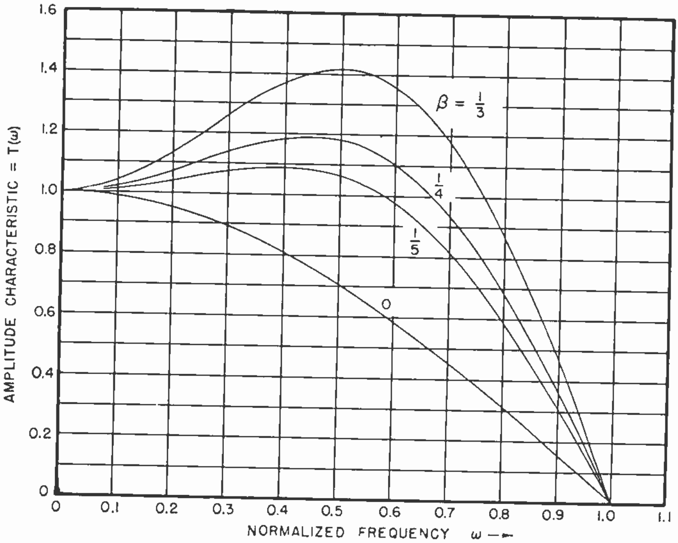

Fig. 17—Cosine minus third-harmonic amplitude characteristic.

$$T(\omega) = \frac{1}{1-\beta}\left[\cos\frac{\pi\omega}{2} - \beta\cos\frac{3\pi\omega}{2}\right], 0 \leqq \omega \leqq 1, \tag{34}$$

where β is the relative amplitude of the third-harmonic component compared to the fundamental. Equation (34) has been plotted in Figure 17 for several values of β. The figure shows the manner in which the amount of high-frequency peaking increases with increasing values of β.

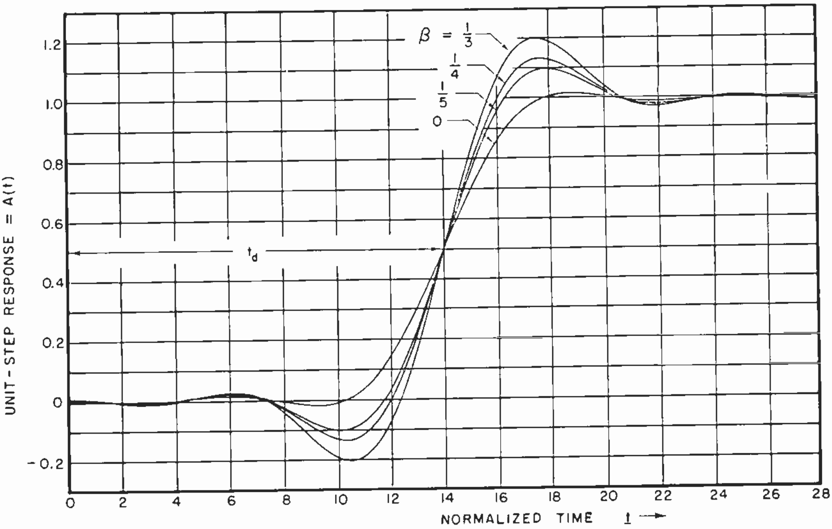

Fig. 18—Unit-step response of linear phase filter with cosine minus third-harmonic amplitude characteristic.

The step response of this low-pass system, shown in Figure 18, has accentuated precursory and following overshoots with minimum transitory ringing before and after the main transition. For television, this type of response is desirable, since it tends to improve the picture quality by providing better resolution.

To obtain an envelope response to a stepped-carrier input similar to that shown in Figure 18, a bandpass system must have an inphase analog filter which is given by Equation (34). If this condition is fulfilled by the bandpass system, the stepped-carrier response will be the same as that for the inphase analog filter for small step amplitude to carrier amplitude ratios.

Using the inphase component as defined by Equation (34) and the low-pass/bandpass relation given by Equation (22), a bandpass system with an amplitude response such as that shown in Figure 19 can be found. In this case, the curve for $\beta = 1/4$ was chosen for the inphase component and the amplitude of the carrier frequency was taken to be 0.5. The peak of the resultant bandpass characteristic is 1.185, so that the carrier is at the 42.2 per cent response point. In accordance with Equation (24), the corresponding quadrature analog is as shown in Figure 20.

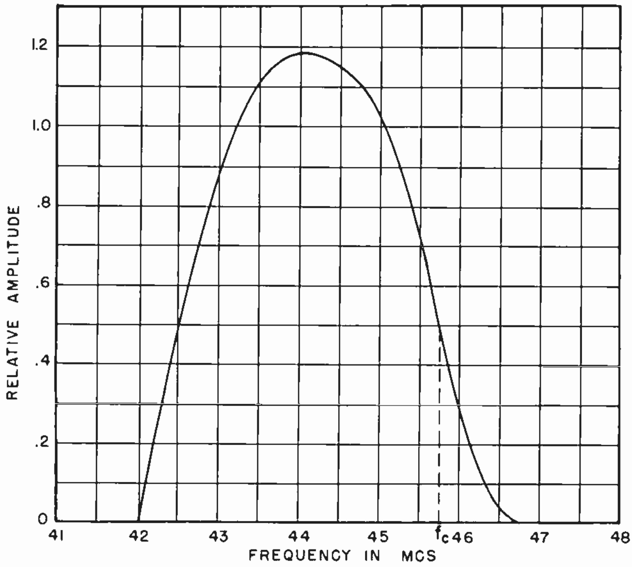

Fig. 19—Bandpass system derived from low-pass analog.

The response of this bandpass system to a suddenly applied carrier is found from the inphase and quadrature components by the method demonstrated previously for the idealized VSB system. The analysis, details of which are given in Appendix III, results in the envelope response plotted in Figure 21. In Figure 21, the response to a unit step of carrier applied at the 0.5 response point is shown. When compared to the curve of Figure 5 for the parabolic bandpass system, the two are seen to be quite similar. With a lower per cent step modulation of the input carrier, the output envelopes are modified as shown in Figure 22. These curves are very similar to the curves of Figure 6 for the parabolic bandpass system. Since the transient response for the derived bandpass system is quite close to that of the parabolic

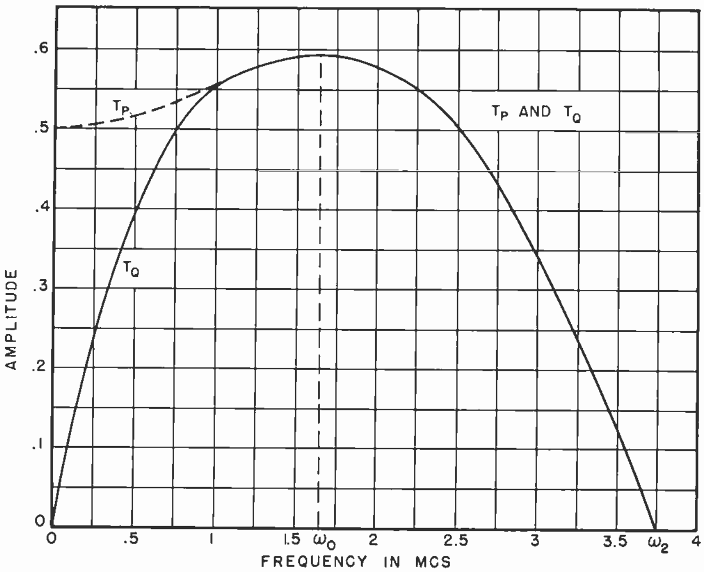

Fig. 20—Low-pass analogs for optimum linear phase i-f curve.

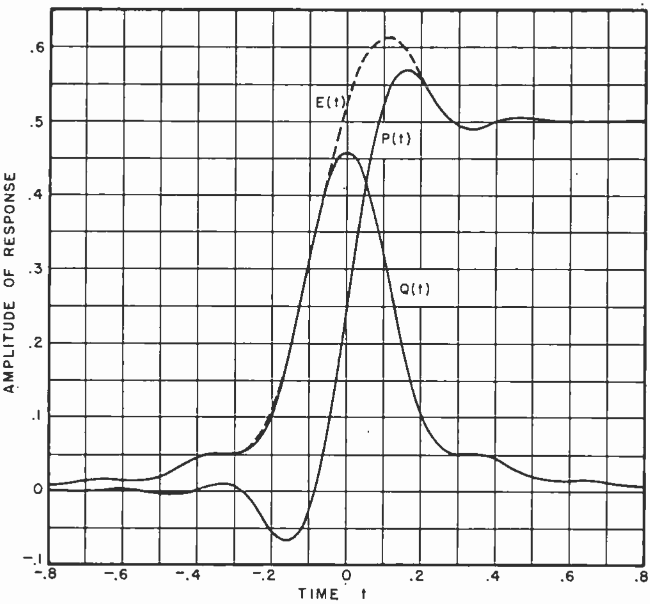

Fig. 21—Envelopes of output carrier from optimum linear phase television i-f characteristic (step of carrier at 42.2 per cent point).

bandpass system for the carrier positions chosen (42.2 and 39.5 per cent), the responses for the other carrier positions are probably very similar. Thus, the response of the bandpass filter shown in Figure 19 with the carrier at 50 per cent would be essentially that given by Figures 8 and 9 for the conditions indicated. Also, the curves of Figures 10 and 11 give the corresponding responses with the carrier at 60 per cent.

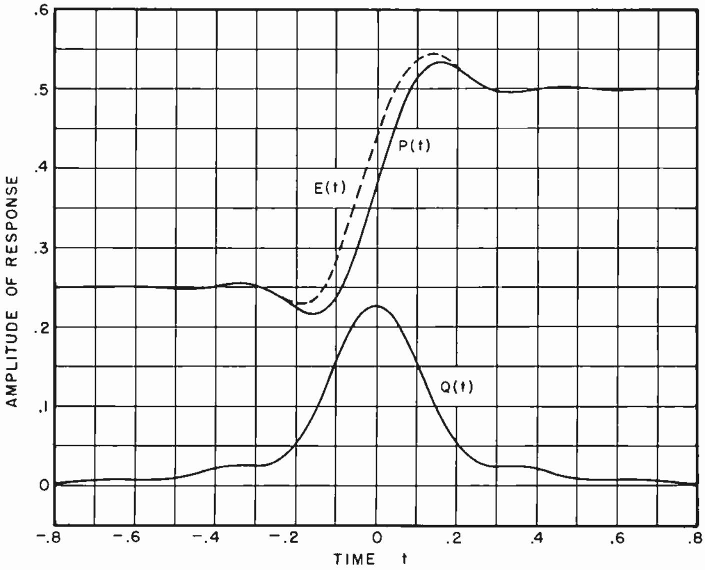

Fig. 22—Envelopes of output carrier for optimum linear phase bandpass system with 50 per cent step-modulated carrier at 42.2 per cent point.

Bandpass analogs for other inphase analog-filter curves can be found in the same manner. If the curve for $\beta = 1/3$ in Figure 17 were chosen, the resultant bandpass system would be as shown in Figure 23. The dashed curve in this figure indicates a possible alternate band shape having the same inphase-analog-filter characteristic. Since more high-frequency peaking occurs with the larger value of β, the effective carrier position is lowered to the 35.5 per cent response point of the derived bandpass systems.

The two band shapes shown in Figure 23 under linear phase conditions would yield the same transient response for small percentages of step-modulation of the input carrier. In this case, the envelope of the output carrier would correspond to the curve for $\beta = 1/3$ in Figure

18. For larger modulation percentages, the quadrature components would have to be considered and the envelopes of the output carrier would then be different.

EXPERIMENTAL RESULTS

The theory of band shaping of the i-f amplifier selectivity curve was applied to a standard production television receiver. With factory type alignment, the selectivity and response to a square-wave modulated carrier was as shown in Figures 24(a) and (b), respectively. For the case shown, the modulation percentage was approximately 50 per cent and the carrier placement was at 45 per cent on the selectivity curve. The output was measured after the second detector in each case. In Figure 24(b), the time-axis deflection sensitivity was 2 microseconds per centimeter with each main division corresponding to 1 centimeter. Skew symmetry in the transient response

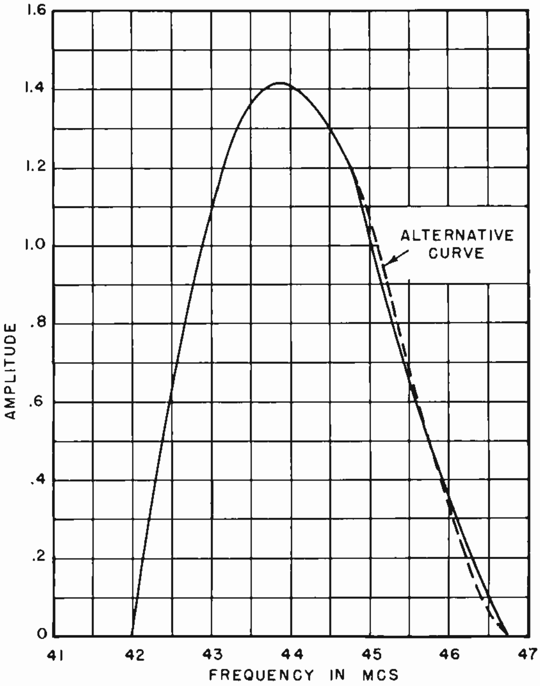

Fig. 23—Bandpass characteristics corresponding to inphase component curve, $\beta = 1/3$.

indicates a phase nonlinearity that can be corrected by linear passive phase correctors or by realignment of the tuned circuits in the i-f amplifier.

Details of the rising and falling transients of the square-wave envelope are shown in Figures 25(a) and (b). In these figures, each centimeter of the time axis is 0.2 microsecond, and the rise and fall times measure approximately 0.23 microsecond. It is noted that the trailing edges of the transitions are smeared. Figures 26(a) and (b) show the corresponding output from the video amplifier driving the cathode of the kinescope. The smear noted in Figure 25 has been considerably reduced due to the overshoot in the video amplifier. At the output of the video amplifier the rise and fall times are about 0.25 microsecond.

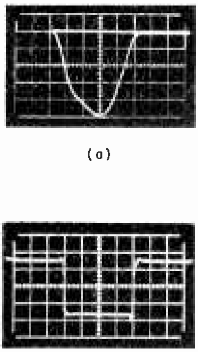
(a)
(b)

FIG. 24 SELECTIVITY AND RESPONSE TO MODULATED CARRIER AT SECOND DETECTOR

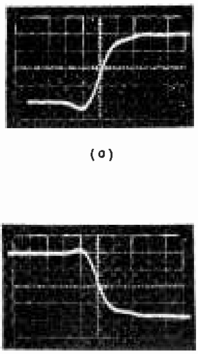
(a)
(b)

FIG. 25 DETAILS OF TRANSIENT RESPONSE AT SECOND DETECTOR

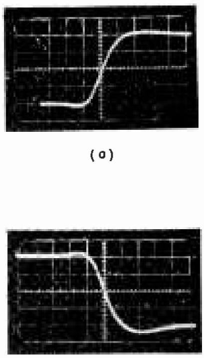
(a)
(b)

FIG. 26 DETAILS OF TRANSIENT RESPONSE AT OUTPUT OF VIDEO AMPLIFIER

The amplitude- and square-wave-modulated carrier responses following the second detector that resulted after realignment of the receiver i-f in accord with the theory discussed are shown in Figures 27(a) and (b), respectively. It is seen that the selectivity curve is quite similar to the band shapes necessary for the single-overshoot transient response. The carrier was placed at the 40 per cent response point on the selectivity curve to obtain the necessary overshoot in the transient response. As in the previous case, the modulation percentage was chosen to be 50 per cent.

Figures 28(a) and (b), showing details of the rising and falling edges, gives a better picture of the improvement obtained in the transient response by phase linearization and band shaping of the i-f characteristic. As before, the time scale is chosen as 0.2 microsecond per centimeter. The rise and fall times are approximately 0.16 microsecond with an associated overshoot of about 15 per cent. After passing through the video amplifier, the response is modified as shown in Figures 29(a) and (b). The video characteristics are such that the following transient ringing shown in Figures 28(a) and (b) are eliminated as indicated in Figures 29(a) and (b). Modification of the waveform by the video amplifier results in an over-all rise time of 0.18 microsecond and a fall time of 0.17 microsecond.

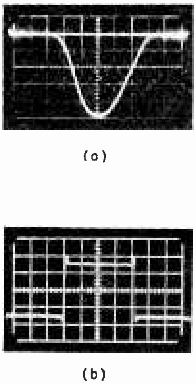
(a)
(b)

FIG. 27 SELECTIVITY AND RESPONSE TO MODULATED CARRIER AT SECOND DETECTOR AFTER REALIGNMENT

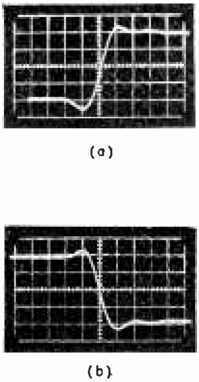
(a)
(b)

FIG. 28 DETAILS OF TRANSIENT RESPONSE AT SECOND DETECTOR AFTER REALIGNMENT

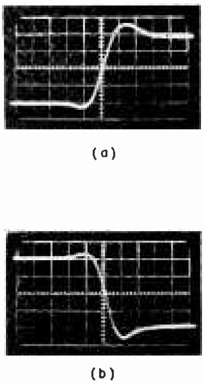
(a)
(b)

FIG. 29 DETAILS OF TRANSIENT RESPONSE AT OUTPUT OF VIDEO AMPLIFIER AFTER REALIGNMENT

These experimental results show that a substantial improvement in the system transient response can be made by proper alignment of the i-f amplifier. Since the "haystack" type of bandpass characteristic is closely associated with a linear phase system having a minimum net phase shift, the band shape and linear phase requirements are compatible.

CONCLUSIONS

To obtain an over-all system transient response which does not have transient ringing before and after the precursory and following overshoot, it is necessary to have a parabolic or "haystack" shaped bandpass system. This conclusion is based on the assumption of a linear phase system and, in addition, that the carrier position is below the 50 per cent response point on the bandpass characteristic. With the carrier below the 50 per cent response point, there is high-frequency peaking of the equivalent analog filter. The amplitude of the precursory and following overshoot is governed by both the band shape and carrier position on the bandpass selectivity curve. As the carrier position is lowered below the 50 per cent response point, the preshoot and overshoot amplitudes increase. At the same time, however, the amplitude of the quadrature component increases so that the over-all envelope response of the system to a stepped carrier becomes more distorted. Thus a compromise must be made in the amount of overshoot desired and the amount of quadrature distortion of the envelope at a given modulation level. Theoretical and experimental results indicate that a carrier position at approximately 40 per cent results in a practical compromise.

APPENDIX I—RESPONSE OF IDEAL VSB SYSTEM TO SUDDENLY APPLIED CARRIER

For the system response characteristic shown in Figure 1,

$$\begin{aligned} T(\omega) &= 1.0 && \omega_1 \leqq \omega \leqq \omega_2 \\ &= \frac{\omega_3 - \omega}{\omega_3 - \omega_2} && \omega_2 \leqq \omega \leqq \omega_3 \\ \theta(\omega) &= -(\omega - \omega_0)t_d && \omega_1 \leqq \omega \leqq \omega_3. \end{aligned} \qquad (35)$$

Using the approximate form of the Fourier integral, the response to a suddenly applied carrier of frequency ω_c is given by

$$R(t) = \frac{1}{2\pi}\int_{-\infty}^{\infty} T(\omega)G(\omega)\exp\{j[\omega t + \theta(\omega)]\}d\omega, \qquad (36)$$

where $G(\omega) = \frac{1}{j(\omega - \omega_c)}$.

Substituting the proper values for $T(\omega)$ and $\theta(\omega)$,

$$\hat{R}(t) = \frac{1}{2\pi j}\int_{\omega_1}^{\omega_2} \exp\{j(\omega t - \omega t_d + \omega_0 t_d)\}\frac{d\omega}{\omega - \omega_c}$$

$$+\frac{1}{2\pi(\omega_3-\omega_2)j}\int_{\omega_2}^{\omega_3}\frac{\omega_3-\omega}{\omega_3-\omega_2}\exp\{j(\omega t-\omega t_d+\omega_0 t_d)\}d\omega, \tag{37}$$

where $\hat{R}(t)$ denotes the complex envelope response function so that $R(t)=\text{Im}\,[\hat{R}(t)]$.

In Equation (37), let $x=\omega-\omega_c$ so that

$$\hat{R}(t)=\frac{\exp(j\Omega_c)}{2\pi j}\left[\int_{\omega_1-\omega_c}^{\omega_2-\omega_c}\exp[jx(t-t_d)]\frac{dx}{x}\right.$$

$$\left.+\frac{1}{\omega_3-\omega_2}\int_{\omega_2-\omega_c}^{\omega_3-\omega_c}\frac{\omega_3-x-\omega_c}{x}\exp[jx(t-t_d)]\,dx\right]$$

$$=\frac{\exp(j\Omega_c)}{2\pi j}\left[\int_{\omega_1-\omega_c}^{\omega_2-\omega_c}\cos[x(t-t_d)]\frac{dx}{x}\right.$$

$$+j\int_{\omega_1-\omega_c}^{\omega_2-\omega_c}\sin[x(t-t_d)]\frac{dx}{x}$$

$$+\frac{\omega_3-\omega_c}{\omega_3-\omega_2}\int_{-(\omega_c-\omega_2)}^{\omega_c-\omega_2}\cos[x(t-t_d)]\frac{dx}{x}$$

$$+\frac{\omega_3-\omega_c}{\omega_3-\omega_2}\int_{\omega_c-\omega_2}^{\omega_3-\omega_c}\cos[x(t-t_d)]\frac{dx}{x}$$

$$+j\frac{\omega_3-\omega_c}{\omega_3-\omega_2}\int_{\omega_2-\omega_c}^{\omega_3-\omega_c}\sin[x(t-t_d)]\frac{dx}{x}$$

$$\left.-\frac{1}{\omega_3-\omega_2}\int_{\omega_2-\omega_c}^{\omega_3-\omega_c}\exp[jx(t-t_d)]\,dx\right]$$

$$
\begin{aligned}
&= \frac{\exp\,(j\Omega_c)}{2\pi j} \Bigg[\mathrm{Ci}\,[(\omega_2 - \omega_c)(t - t_d)] - \mathrm{Ci}\,[(\omega_1 - \omega_c)(t - t_d)] \\
&\quad + j\,\{\mathrm{Si}\,[(\omega_2 - \omega_c)(t - t_d)] - \mathrm{Si}\,[(\omega_1 - \omega_c)(t - t_d)]\} \\
&\qquad\qquad\qquad\qquad\qquad\qquad\qquad\qquad + \frac{\pi j\,(\omega_3 - \omega_c)}{\omega_3 - \omega_2} \\
&\quad + \frac{\omega_3 - \omega_c}{\omega_3 - \omega_2}\,\{\mathrm{Ci}\,[(\omega_3 - \omega_c)(t - t_d)] - \mathrm{Ci}\,[(\omega_c - \omega_2)(t - t_d)]\} \\
&\quad + j\,\frac{\omega_3 - \omega_c}{\omega_3 - \omega_2}\,\{\mathrm{Si}\,[(\omega_3 - \omega_c)(t - t_d)] - \mathrm{Si}\,[(\omega_2 - \omega_c)(t - t_d)]\} \\
&\quad - \frac{1}{j\,(\omega_3 - \omega_2)(t - t_d)}\,\{\cos\,[(\omega_3 - \omega_c)(t - t_d)] \\
&\qquad\qquad\qquad\qquad - \cos\,[(\omega_2 - \omega_c)(t - t_d)] \\
&\quad + j\sin\,[(\omega_3 - \omega_c)(t - t_d) - j\sin\,[(\omega_2 - \omega_c)(t - t_d)]\} \Bigg],
\end{aligned}
\tag{38}
$$

where $\exp\,(j\Omega_c) = \exp\,\{j[\omega_c(t - t_d) + \omega_0 t_d]\}$. The response $R(t)$ can be written as

$$
R(t) = P(t)\sin\,[\omega_c(t - t_d) + \omega_0 t_d] + Q(t)\cos\,[\omega_c(t - t_d) + \omega_0 t_d],
\tag{39}
$$

where

$$
\begin{aligned}
P(t) &= \frac{1}{2}\left(\frac{\omega_3 - \omega_c}{\omega_3 - \omega_2}\right)\Bigg[1 + \frac{1}{\pi}\,\{\mathrm{Si}\,[(\omega_3 - \omega_c)(t - t_d)] \\
&\qquad\qquad\qquad\qquad - \mathrm{Si}\,[(\omega_2 - \omega_c)(t - t_d)]\}\Bigg] \\
&\quad + \frac{1}{2\pi}\,\{\mathrm{Si}\,[(\omega_2 - \omega_c)(t - t_d)] - \mathrm{Si}\,[(\omega_1 - \omega_c)(t - t_d)]\} \\
&\quad + \frac{1}{2\pi(\omega_3 - \omega_2)(t - t_d)}\,\{\cos\,[(\omega_3 - \omega_c)(t - t_d)] \\
&\qquad\qquad\qquad\qquad - \cos\,[(\omega_2 - \omega_c)(t - t_d)]\}
\end{aligned}
\tag{40}
$$

$$Q(t) = -\frac{1}{2\pi}\Bigg[\{\mathrm{Ci}\,[(\omega_2 - \omega_c)(t - t_d)] - \mathrm{Ci}\,[(\omega_1 - \omega_c)(t - t_d)]\}$$

$$+ \frac{\omega_3 - \omega_c}{\omega_3 - \omega_2}\{\mathrm{Ci}\,[\omega_3 - \omega_c)(t - t_d)] - \mathrm{Ci}\,[(\omega_c - \omega_2)(t - t_d)]\}$$

$$- \frac{1}{(\omega_3 - \omega_2)(t - t_d)}\{\sin[(\omega_3 - \omega_c)(t - t_d)]$$

$$- \sin[(\omega_2 - \omega_c)(t - t_d)]\}\Bigg]. \qquad (41)$$

If the carrier frequency is placed midway between ω_2 and ω_3, so that $\omega_3 - \omega_c = \omega_c - \omega_2$, then Equations (40) and (41) reduce to

$$P(t) = \frac{1}{4}\left\{1 + \frac{2}{\pi}\,\mathrm{Si}\,[(\omega_c - \omega_1)(t - t_d)]\right\} \qquad (42)$$

$$Q(t) = \frac{1}{2\pi}\Bigg\{\frac{2\sin[(\omega_3 - \omega_c)(t - t_d)]}{(\omega_3 - \omega_2)(t - t_d)} - \mathrm{Ci}\,[(\omega_2 - \omega_c)(t - t_d)]$$

$$+ \mathrm{Ci}\,[(\omega_1 - \omega_c)(t - t_d)]\Bigg\}. \qquad (43)$$

APPENDIX II—RESPONSE OF PARABOLIC BANDPASS SYSTEM TO SUDDENLY APPLIED SINE WAVE

Let the transfer function for the parabolic bandpass system be represented by

$$Z(\omega) = T(\omega)\exp(-j\omega t_d), \qquad (44)$$

where

$$T(\omega) = 1 - \left(\frac{\omega - \omega_0}{\omega_2 - \omega_0}\right)^2, \qquad \omega_1 \leq \omega \leq \omega_2.$$

By the Fourier Integral, the complex form of the response to a step of carrier of frequency ω_c will be

$$\hat{R}(t) = \frac{1}{2\pi j}\int_{\omega_1}^{\omega_2}\left[1 - \left(\frac{\omega - \omega_0}{\omega_2 - \omega_0}\right)^2\right]\frac{1}{\omega - \omega_c}\exp(j\omega t)\,d\omega, \qquad (45)$$

omitting the delay t_d. Substituting $x = \omega - \omega_c$ in Equation (45), we obtain

$$\hat{R}(t) = \frac{1}{2\pi j} \int_{\omega_1 - \omega_c}^{\omega_2 - \omega_c} \frac{1}{x} \left[1 - \frac{(x + \omega_c - \omega_0)^2}{(\omega_2 - \omega_0)^2} \right] \exp\left[j(x + \omega_c)t \right] dx$$

$$= \frac{\exp(j\omega_c t)}{2\pi j} \left[\int_{\omega_1 - \omega_c}^{\omega_2 - \omega_c} \frac{\exp(jxt)}{x} dx \right.$$

$$\left. - \frac{1}{(\omega_2 - \omega_0)^2} \int_{\omega_1 - \omega_c}^{\omega_2 - \omega_c} \frac{(x + \omega_c - \omega_0)^2}{x} \exp(jxt)\, dx \right]$$

$$= \frac{\exp(j\omega_c t)}{2\pi j} \left[\int_{\omega_1 - \omega_c}^{\omega_2 - \omega_c} \frac{\cos xt}{x} dx + j \int_{\omega_1 - \omega_c}^{\omega_2 - \omega_c} \frac{\sin xt}{x} dx \right.$$

$$\left. - \frac{1}{(\omega_2 - \omega_0)^2} \int_{\omega_1 - \omega_c}^{\omega_2 - \omega_c} \frac{x^2 + 2x(\omega_c - \omega_0) + (\omega_c - \omega_0)^2}{x} \exp(jxt)\, dx \right]$$

$$= \frac{\exp(j\omega_c t)}{2\pi j} \left[j\pi + \int_{\omega_c - \omega_1}^{\omega_2 - \omega_c} \frac{\cos xt}{x} dx + j \int_{\omega_1 - \omega_c}^{\omega_2 - \omega_c} \frac{\sin xt}{x} dx \right.$$

$$- \frac{1}{(\omega_2 - \omega_0)^2} \int_{\omega_1 - \omega_c}^{\omega_2 - \omega_c} x \exp(jxt)\, dx - \frac{2(\omega_c - \omega_0)}{(\omega_2 - \omega_0)^2} \int_{\omega_1 - \omega_c}^{\omega_2 - \omega_c} \exp(jxt)\, dx$$

$$\left. - \frac{(\omega_c - \omega_0)^2}{(\omega_2 - \omega_0)^2} \int_{\omega_1 - \omega_c}^{\omega_2 - \omega_c} \exp(jxt) \frac{dx}{x} \right]. \qquad (46)$$

Integrating Equation (46) term by term gives

$$\hat{R}(t) = \exp(j\omega_c t) \left\{ \frac{1}{2} + \frac{1}{2\pi j} \left[\mathrm{Ci}\,(\omega_2 - \omega_c)t - \mathrm{Ci}\,(\omega_c - \omega_1)t \right] \right.$$

$$
\begin{aligned}
&-\frac{1}{2}\left(\frac{\omega_c-\omega_0}{\omega_2-\omega_0}\right)^2+\frac{1}{2\pi}\left[\mathrm{Si}\,(\omega_2-\omega_c)t-\mathrm{Si}\,(\omega_1-\omega_c)t\right]\\
&-\frac{\exp\{j(\omega_2-\omega_c)t\}}{2\pi j(\omega_2-\omega_0)^2}\left[\frac{\omega_2-\omega_c}{jt}+\frac{1}{t^2}\right]\\
&+\frac{\exp\{j(\omega_1-\omega_c)t\}}{2\pi j(\omega_2-\omega_0)^2}\left[\frac{\omega_1-\omega_c}{jt}+\frac{1}{t^2}\right]\\
&+\frac{\omega_c-\omega_0}{\pi(\omega_2-\omega_0)^2t}\left[\exp\{j(\omega_2-\omega_c)t\}-\exp\{j(\omega_1-\omega_c)t\}\right]\\
&-\frac{(\omega_c-\omega_0)^2}{2\pi j(\omega_2-\omega_0)^2}\left[\mathrm{Ci}\,(\omega_2-\omega_c)t-\mathrm{Ci}\,(\omega_1-\omega_c)t\right]\\
&\left.-\frac{(\omega_c-\omega_0)^2}{2\pi(\omega_2-\omega_0)^2}\left[\mathrm{Si}\,(\omega_2-\omega_c)t-\mathrm{Si}\,(\omega_1-\omega_c)t\right]\right\}. \qquad (47)
\end{aligned}
$$

Equation (47) may be rewritten in the form

$$\hat{R}(t)=\exp\,(j\omega_c t)\,[P(t)+jQ(t)], \qquad (48)$$

where $P(t)$ and $Q(t)$ are given by Equations (6) and (7). If the time delay t_d is to be included, t is replaced by $t-t_d$.

APPENDIX III—RESPONSE OF SYSTEM WITH OPTIMUM BAND SHAPE TO SUDDENLY APPLIED SINE WAVE

The amplitude function of the inphase analog filter is given by one half of Equation (34) and is redrawn in Figure 30 as an even function of frequency. By the Fourier integral, the unit-step response is given by

$$P(t)=\frac{1}{2\pi}\int_{-\infty}^{\infty}T_p(\omega)G(\omega)\exp j[\omega t+\theta(\omega)]\,d\omega$$

$$=\frac{1}{4\pi j(1-\beta)}\int_{-\omega_2}^{\omega_2}\frac{1}{\omega}\left[\cos\frac{\pi\omega}{2}-\beta\cos\frac{3\pi\omega}{2}\right]\exp\,(j\omega t)\,d\omega$$

$$= \frac{1}{4} + \frac{1}{4\pi(1-\beta)} \int_{-\omega_2}^{\omega_2} \frac{1}{\omega} \left[\cos \frac{\pi\omega}{2} - \beta \cos \frac{3\pi\omega}{2} \right] \sin \omega t \, d\omega, \tag{49}$$

where the steady-state term is the contribution of the pole at the origin. Equation (49) can be rewritten as

$$P(t) = \frac{1}{4} + \frac{1}{2\pi(1-\beta)} \int_{0}^{\omega_2} \frac{1}{\omega} \left[\sin \omega \left(t + \frac{\pi}{2} \right) + \sin \omega \left(t - \frac{\pi}{2} \right) \right] d\omega$$

$$- \frac{\beta}{2\pi(1-\beta)} \int_{0}^{\omega_2} \frac{1}{\omega} \left[\sin \omega \left(t + \frac{3\pi}{2} \right) + \sin \omega \left(t - \frac{3\pi}{2} \right) \right] d\omega, \tag{50}$$

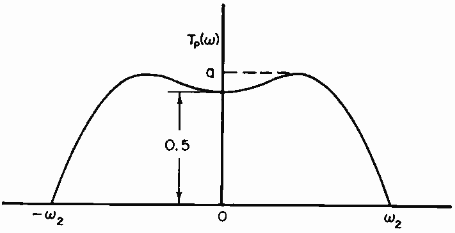

Fig. 30—Amplitude curve of inphase analog filter.

so that the envelope of the inphase component of the output carrier is

$$P(t) = \frac{1}{4} + \frac{1}{2\pi(1-\beta)} \left\{ \mathrm{Si}\, \omega_2 \left(t + \frac{\pi}{2} \right) + \mathrm{Si}\, \omega_2 \left(t - \frac{\pi}{2} \right) \right\}$$

$$- \frac{\beta}{2\pi(1-\beta)} \left\{ \mathrm{Si}\, \omega_2 \left(t + \frac{3\pi}{2} \right) + \mathrm{Si}\, \omega_2 \left(t - \frac{3\pi}{2} \right) \right\} \tag{51}$$

In order to obtain the quadrature component of the output carrier, an explicit expression must be obtained for the quadrature amplitude characteristic. It is found that a fairly good representation of the quadrature curve shown in Figure 20 is given by the functions

$$
\begin{aligned}
T_Q(\omega) &= a\left[\;1+\left(\frac{\omega-\omega_0}{\omega_0}\right)^3\right] && 0 \leqq \omega \leqq \omega_0\\
&= a\left[\;1-\left(\frac{\omega-\omega_0}{\omega_2-\omega_0}\right)^2\right] && \omega_0 \leqq \omega \leqq \omega_2. \qquad (52)
\end{aligned}
$$

The analog filter for the quadrature component is shown in Figure 31. To make the integration process simpler, the amplitude and phase functions are modified as indicated by the dashed lines in Figure 31.

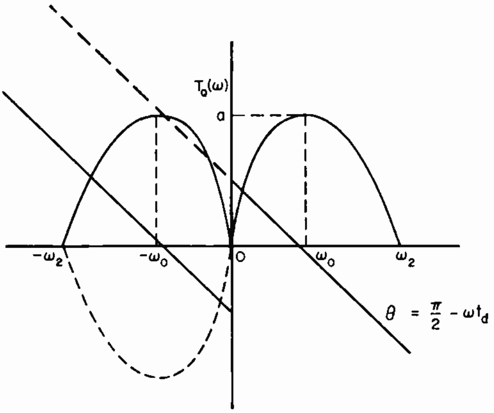

Fig. 31—Low-pass analog for quadrature component.

With this change, the system transfer function becomes

$$T_Q \exp j\theta_Q = T_Q \exp\left[\;j\left(\frac{\pi}{2}-\omega t_d\right)\right]. \qquad (53)$$

The response of the analog to a unit step is then given by

$$
\begin{aligned}
Q(t) &= \frac{1}{2\pi j}\int_{-\infty}^{\infty}\frac{T_Q(\omega)}{\omega}\exp\left[\;j\left(\omega t+\frac{\pi}{2}\right)\right]d\omega\\
&= \frac{a\exp(j\pi/2)}{2\pi j}\left[-\int_{-\omega_2}^{-\omega_0}\frac{1}{\omega}\left[1-\left(\frac{\omega+\omega_0}{\omega_2-\omega_0}\right)^2\right]\exp(j\omega t)\,d\omega\right.
\end{aligned}
$$

$$-\int_{\omega_0}^{0} \frac{1}{\omega}\left[1-\left(\frac{\omega+\omega_0}{\omega_0}\right)^3\right]\exp\,(j\omega t)\,d\omega$$

$$+\int_{0}^{\omega_0} \frac{1}{\omega}\left[1+\left(\frac{\omega-\omega_0}{\omega_0}\right)^3\right]\exp\,(j\omega t)\,d\omega$$

$$+\int_{\omega_0}^{\omega_2} \frac{1}{\omega}\left[1-\left(\frac{\omega-\omega_0}{\omega_2-\omega_0}\right)^2\right]\exp\,(j\omega t)\,d\omega\,\Bigg]. \qquad (54)$$

Equation (54) can be integrated and reduced to the form

$$Q(t)=\frac{a}{\pi}\left\{\left[1-\frac{\omega_0^2}{(\omega_2-\omega_0)^2}\right]\left[\mathrm{Ci}(\omega_2 t)-\mathrm{Ci}(\omega_0 t)\right]-\frac{\cos\omega_2 t}{t^2(\omega_2-\omega_0)^2}\right.$$

$$+\frac{2\omega_0-\omega_2}{t(\omega_2-\omega_0)^2}\sin\omega_2 t+\frac{1}{t^2}\left[\frac{1}{(\omega_2-\omega_0)^2}-\frac{1}{\omega_0^2}\right]\cos\omega_0 t$$

$$\left.+\left[\frac{1}{\omega_0 t}-\frac{2}{\omega_0^3 t^3}-\frac{\omega_0}{(\omega_2-\omega_0)^2 t}\right]\sin\omega_0 t+\frac{3}{\omega_0^2 t^2}\right\}. \qquad (55)$$

When $t = 0$, the quadrature component $Q(t)$ reduces to

$$Q(0)=\frac{a}{\pi}\left\{\left[1-\frac{\omega_0^2}{(\omega_2-\omega_0)^2}\right]\log_e\frac{\omega_2}{\omega_0}+\frac{\omega_2+\omega_0}{2(\omega_2-\omega_0)}+\frac{5}{6}\right\}. \qquad (56)$$

Equation (56) is obtained from equation (55) using the relations

$$\mathrm{Ci}(x)=\Gamma+\log x+\cdots$$

$$\sin x=x-\frac{x^3}{3!}+\cdots$$

$$\cos x=1-\frac{x^2}{2!}+\cdots$$

Γ is Euler's constant.

SUPPRESSION AND LIMITING OF UNDESIRED SIGNALS IN TRAVELING-WAVE-TUBE AMPLIFIERS*

By

H. J. Wolkstein

RCA Electron Tube Division,
Harrison, N. J.

Summary—*It is well known that a traveling-wave tube will amplify signals of more than one frequency simultaneously with negligible interaction as long as the total input r-f power does not drive the tube into saturation. Not so well known is the performance of the traveling-wave tube in amplifying low-level signals in the presence of r-f power as high as 30 decibels over that required to saturate the tube. The drop in gain of the low-level signal has been found to be, in general, proportional to the input power and inversely proportional to the frequency of the large signal. However, the complexity of beam bunching above saturation results, for each tube type, in different rates of low-level signal suppression. In some cases, when the tubes are overdriven too far, this bunching actually produces a tendency for the suppression to decrease. This paper considers saturation characteristics in the presence of overdriving signals and the effect on gain and power output.*

Introduction

TRANSMISSION AND RECEPTION of microwave frequencies have been considerably improved through the development of the traveling-wave tube. The large bandwidth–gain product (five to six orders of magnitude greater than the best conventional gridded tube) makes the traveling-wave tube an exceedingly useful circuit component. Microwave literature adequately describes traveling-wave tube performance, technology, and system usage exploiting the octave bandwidth coverage and the attendant high gain available. However, most of the literature has been confined to single-frequency performance in the octave bandpass and fails to predict adequately the behavior of the traveling-wave tube in many applications.

This paper describes the performance of traveling-wave tubes in the presence of multiple signals of varied frequency and power levels within the pass band. Signal suppression, cross modulation, and power overdrive are also discussed.

---

* Manuscript received 28 March 1961.

SIMILARITY OF CONVENTIONAL GRIDDED TUBES AND TRAVELING-WAVE TUBES

The traveling-wave tube, like the low-frequency conventional gridded amplifier, is exposed to a wide range of signal strengths in many applications. The performance characteristic of the gridded tube can be adequately predicted for a wide variation of signal input by use of appropriate dynamic transfer curves, as shown in Figure 1(a). It is interesting to note that the operating performance of the traveling-wave tube can also be predicted from similar transfer curves.

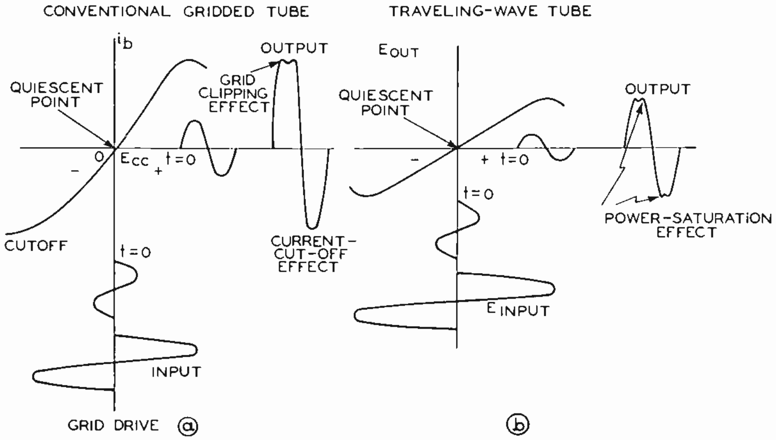

Fig. 1—Dynamic transfer curves of (a) a conventional gridded tube and (b) a traveling-wave tube.

The similarity becomes quite apparent when the usual traveling-wave-tube power characteristics are presented in terms of input–output voltages. This presentation provides a transfer characteristic symmetrical about the operating quiescent point of the traveling-wave tube, as shown in Figure 1(b). Presentation of transfer curves for traveling-wave tubes in this manner has been found useful.

In many applications, linear performance with little amplitude and phase distortion is desired. Such performance characteristics obviously require operation confined to the small-signal linear-gain transfer region. In other applications where strong signals are encountered, good output overdrive characteristics are desired. In both methods of amplification, however, considerable amplitude distortion and harmonic generation is experienced when operation occurs in the non-linear transfer regions, as shown in Figure 1.

Overdrive operation for the gridded tube results in squaring due to grid clipping and current cutoff. The traveling-wave tube produces similar amplitude distortion (particularly when exposed to comparatively strong signals) which causes beam-bunching saturation.

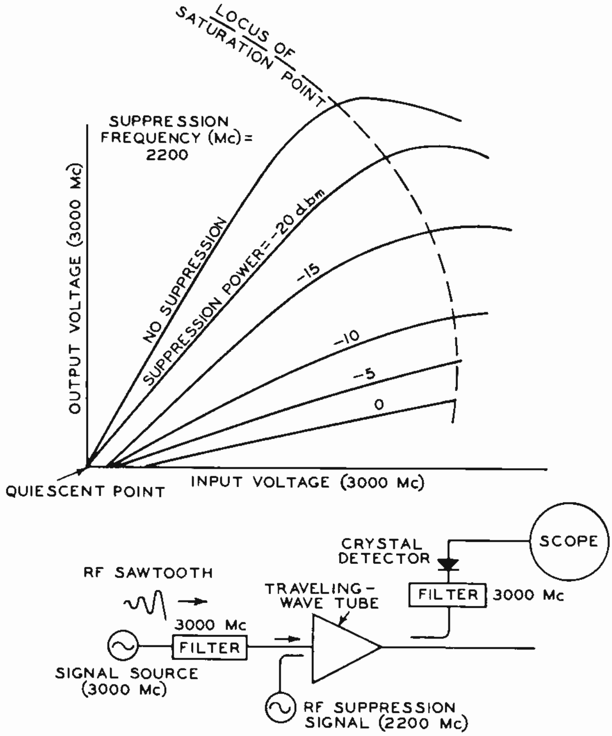

Fig. 2—Transfer characteristics of a traveling-wave tube in the presence of an extraneous suppression signal at a fixed frequency.

MULTIPLE-SIGNAL OPERATION

Operation of the traveling-wave tube in many applications can not be predicted on the basis of single-frequency performance when other signals exist in the pass band. As an indication of this phenomenon, dynamic transfer curves at unique frequencies were obtained in the presence of extraneous signals of varied strength elsewhere in the band. A set of these measurements obtained from an S-band 10-milliwatt traveling-wave tube is shown in Figure 2.

Individual voltage transfer curves were obtained by use of a recurrent linear varying r-f input signal at 3000 megacycles in the presence of a fixed-amplitude extraneous or undesired 2200-megacycle signal passed through the same traveling-wave tube. The detected, positive-output half of the symmetrical voltage-transfer curve is shown in Figure 2. As a basis for reference, the upper curve indicates the transfer characteristics at 3000 megacycles with no extraneous input signal. The additional descending curves were observed for various extraneous signal levels starting with —20 dbm of the unwanted 2200-megacycle input signal and increasing to 0 dbm in 5-decibel increments. These data show that the small-signal gain, initially of the order of 30 decibels as defined by the slope of the linear portion of the transfer curve, is suppressed to 12 decibels by an increase in overdriving power at some other frequency. Actually, as long as the total input power (at all frequencies) is less than that required to cause operation in the nonlinear region of the transfer characteristic, only negligible gain suppression occurs. However, when one or more of the signals cause the total input power to be in the nonlinear region, significant gain suppression occurs. The stronger signal in the pass band exerts the greater control on the beam and hence causes the power output at other frequencies to be suppressed. This suppression leads to a reciprocal influence which generally affects the gain everywhere in the band.

An interesting aspect of these characteristics is the inference that increased gain suppression at an extraneous frequency causes the linear portion of the transfer curve to extend and thereby improves the dynamic range of the tube. Reduction of amplitude distortion by this technique is discussed later.

Several interesting curves, joined to form a contour plot of suppression characteristics, are shown in Figure 3. When the ordinate displays output and the abscissa input, a transfer plot is formed for the data given. In these plots, dynamic transfer curves are obtained at a fixed frequency of 3000 megacycles, with the suppression frequency varied from 2500 to 4000 megacycles. Again, the uppermost curve represents the positive-detected half of the voltage transfer curve in the absence of overdriving signals; successively lower curves depict the degradation in gain due to various suppression-signal levels.

It should be noted that a suppression signal of a lower frequency has a greater effect on the degradation of gain than higher-frequency suppression signals of the same power level. This control is apparently a result of the increased beam-to-helix coupling and the increased depth of bunching across the radius of the beam, both of which are a function of wavelength. The difference in suppressed-gain levels is of the order of 15 decibels for maximum-suppression signal amplitude at both ends of the band.

The degradation of gain as a result of the aforementioned suppression characteristics in the pass band must be anticipated. Such degradation is of extreme importance when a wide-open traveling-wave tube amplifier is used in microwave receiver front-end operation. It becomes increasingly important when jamming signals are encountered. There are additional applications, however, in which these suppression characteristics can be effectively employed, at the desired frequency, to reduce the gain of undesirable signals and thereby enhance single-frequency performance. Furthermore, for this mode of operation, in which good suppression characteristics are desired, it is felt that a hollow beam and good circuit coupling would provide optimum results.

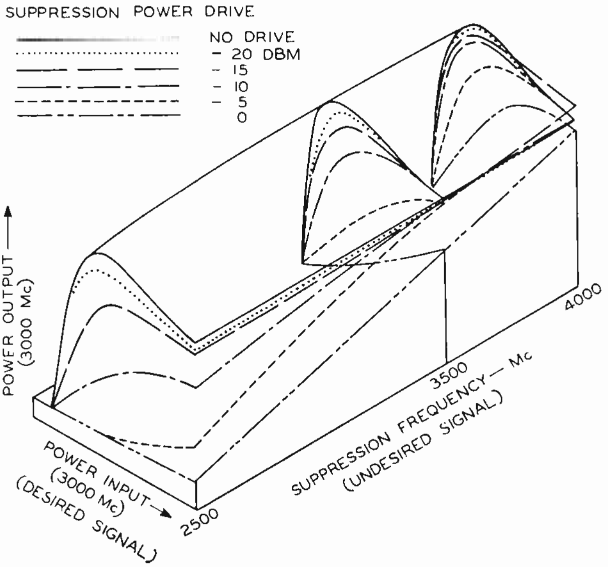

Fig. 3—A contour plot of the characteristics of a traveling-wave tube in the presence of an extraneous suppression signal with varying frequency.

CROSS MODULATION

As may be inferred from the previous discussion of suppression characteristics, cross modulation must also be dependent on the instantaneous power elsewhere in the pass band of the traveling-wave-tube amplifier. An oscillograph display indicating the effect of cross modulation on an S-band, 10-milliwatt tube is shown in Figure 4. For these measurements, a square-wave-modulated extraneous r-f signal at 2200 megacycles is applied to the traveling-wave tube for operation

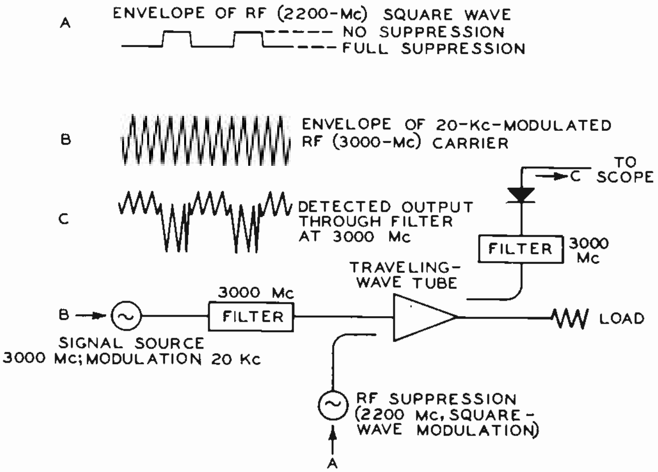

Fig. 4—The effects of suppression signals on cross modulation of a traveling-wave tube.

near saturation. A small-amplitude r-f wave at 3000 megacycles modulated at a 20-kilocycle rate, is also passed through the tube. The detected output (shown at the bottom of Figure 4) obtained through

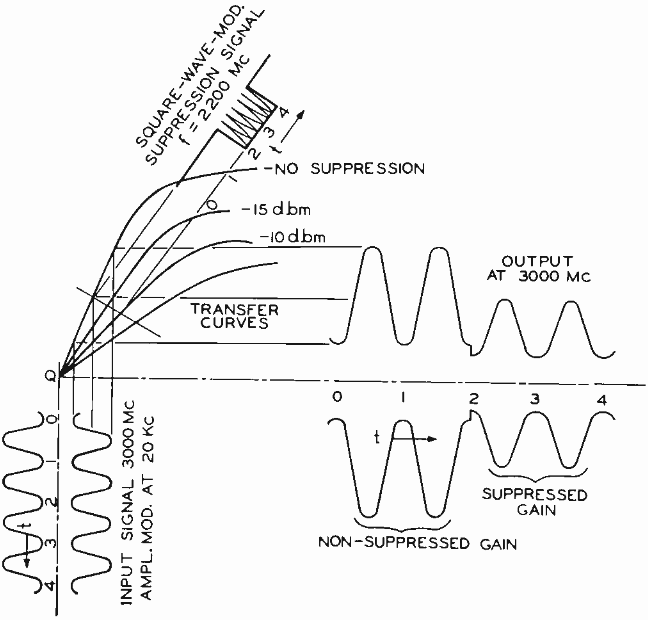

Fig. 5—The prediction of cross modulation using the dynamic transfer curves in the presence of a suppression signal of varying strength.

a 3000-megacycle filter, displays pronounced cross-modulation effects. Results can be analyzed and predicted by use of the previously established transfer curves, as shown in Figure 5.

As illustrated, a cross plot of the small-signal r-f carrier operated in the linear-gain region is made with the appropriate dynamic transfer curve. This transfer curve, and also the gain degradation, varies with the modulation of the suppression signal and results in predictable cross-modulation effects at the small-signal frequency. This cross-modulation, manifested by a dependence of the output on the modulation signals involved, can be considerably reduced if over-all system operation is confined to the linear small-signal region.

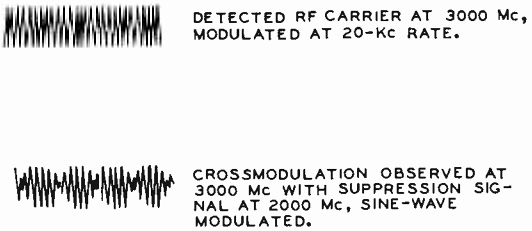

Fig. 6—Cross-modulation effects when a sinusoidally varying extraneous overdrive signal is applied to a traveling-wave tube.

Figure 6 shows an additional oscilloscope display of the qualitative effects of cross-modulation when a sinusoidally varying overdrive signal is substituted for the square wave previously used. The upper curve represents the single-frequency case at 3000 megacycles in the presence of the sine-wave-modulated over-driving suppression signal. This effect is an extreme example of modulation distortion.

OVERDRIVE CHARACTERISTICS

In an attempt to resolve the problems of signal suppression and modulation distortion, which are the results of saturation somewhere in the pass band, emphasis has been placed on extending the input power range of the traveling-wave tube. Particular emphasis has been directed toward the low-frequency end of the pass band, where suppression capabilities of extraneous signals have a decided effect on small signals at the high end of the band. The traveling-wave tube used to obtain the curve shown in Figure 7 provides more than 50 milliwatts of peak power, yet has only a 15-decibel range of input power that will insure an output over 5 dbm at all frequencies in the octave band. This tube uses a single conventional attenuator to isolate input from output.

Extensive measurements made on a number of traveling-wave tubes have indicated that, in general, the rate of power fall-off beyond saturation varies with increased wavelength across the band for a tube having uniform initial gain conditions. Figure 8 shows a contour plot illustrating the power fall-off dependence on frequency in the overdrive region. As indicated, there is a pronounced dip and rise in power output at low frequencies which virtually disappears with increased frequency. Moreover, those same conditions which produce the power dip and gain reduction for low frequencies in the overdrive region also cause severe gain suppression for other signals in the pass band.

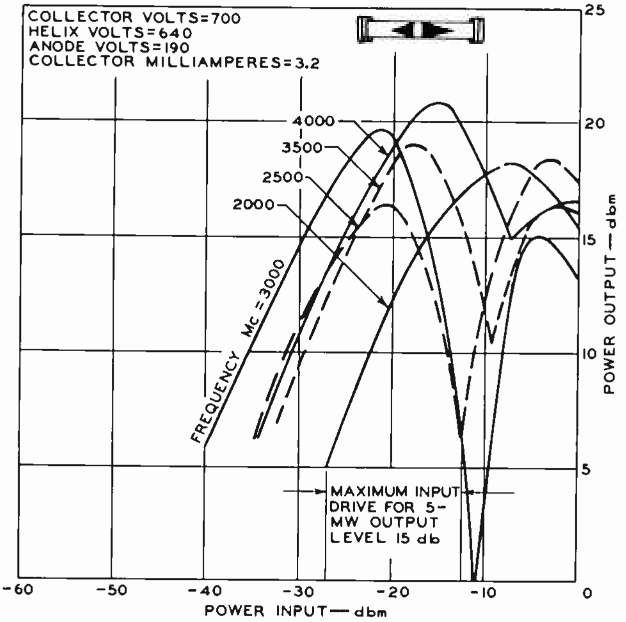

Fig. 7—Power overdrive characteristics of a traveling-wave tube using a single lumped attenuator.

The factors which have been found to influence the overdrive characteristics are numerous. Basically, the penetration of the axial electric field emanating from the helix increases considerably with increased wavelengths. It is probable that this (preferred) field penetration at low frequency causes the decelerated portion of the electron beam to re-extract energy efficiently from the amplified helix wave beyond saturation.

The placement of decoupling attenuators is an additional critical

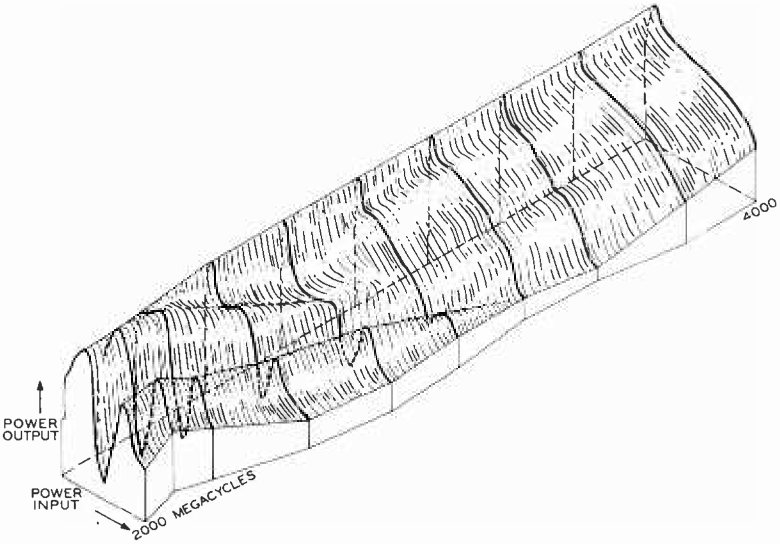

Fig. 8—A contour plot of the power-overdrive characteristics of a traveling-wave tube using single lumped attenuation.

parameter which affects overdrive characteristics. Empirical positioning of several small, external, multiple attenuators on the traveling-wave-tube envelope, which was previously described as inadequate for overdrive, resulted in greatly improved overdrive characteristics, as shown in Figure 9. Considerable reduction in power "fall-off" with

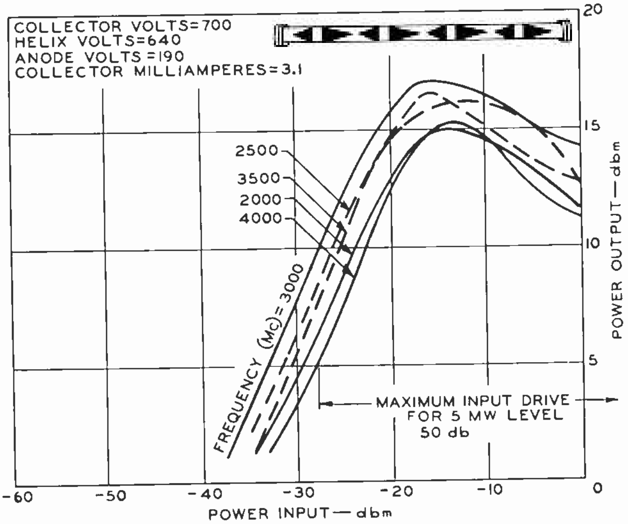

Fig. 9—Improved power-overdrive characteristics of a traveling-wave tube using segmented lumped attenuation.

increased input power has been observed. The tolerable overdrive range has been increased from approximately 15 decibels to well over 40 decibels at the 5-milliwatt output-power level. This improvement is attributed to the segmented slow-wave structure which, in effect, creates a number of circuits in cascade. R-F coupling is provided by the modulated beam which interacts with successive helix sections.

In addition to the extension of overdrive capabilities, there is an indication that suppression of low-level signals may be minimized by the use of multiple attenuators. Figure 10 shows the small-signal performance at a constant input power of —20 dbm for several specific frequencies in the band. The gain for these various frequencies has been observed to decrease linearly when plotted as a function of input power. These small-signal gain curves resemble the gain curve for the overdriving signal, which in this case is 3600 megacycles. This relationship suggests that delaying the onset of power fall-off for the overdriving signal will tend to maintain slightly higher gain for the low-power suppressed signals across the band. Conversely, tolerating a rapid overdrive power fall-off enhances suppression and reduces the low-level gain in the band in the presence of overdriving signals. Verification of this effect is shown in Figure 11. A comparison of the difference in gain with respect to input power, for both the narrow-range and wide-range overdrive tubes previously described,

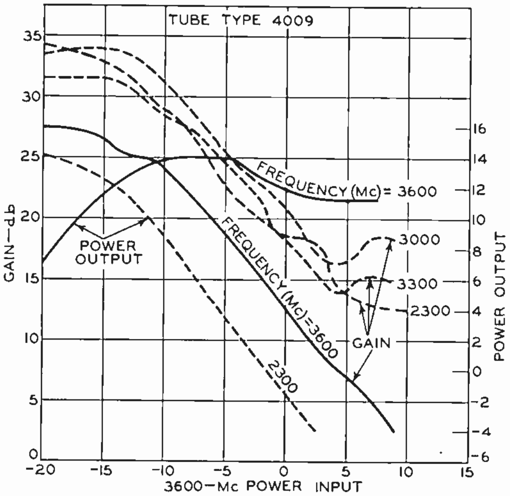

Fig. 10—The power output and gain characteristics of a traveling-wave tube at various frequencies as a function of input at a fixed frequency. (The plot is for a multiple-attenuation tube.)

is illustrated. The top curve indicates the gain for the narrow-range, single-attenuator tube; the additional gain curve shows the performance of the multiattenuator tube. The difference in gain for these two extreme conditions is shown at the bottom of Figure 11. As indicated, the gain difference increases considerably for the multiattenuator tube with large overdriving signal. At an input power level of —10 dbm, for example, the multiattenuator tube yields 20 decibels more gain than the single-attenuator tube. This increase in gain for the overdriving signal insures a similar increase for the low-level suppressed-signal gain across the band.

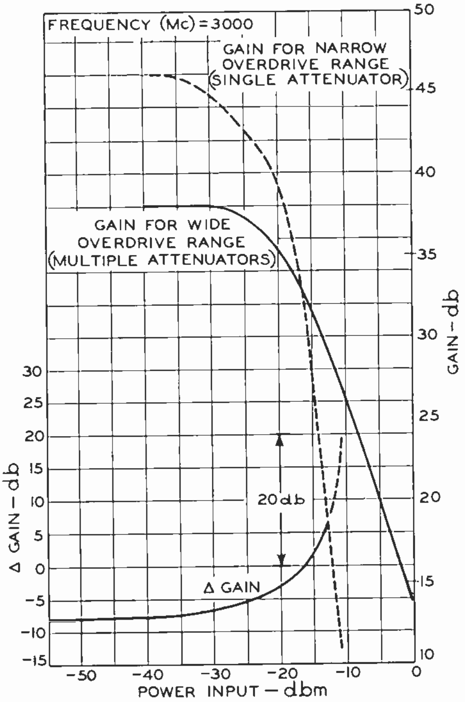

Fig. 11—The difference in gain with power overdrive for the same traveling-wave tube using a single attenuator in comparison with multiple attenuators.

This feature is invaluable in many wide-band microwave-receiver applications where exposure to surveillance, countermeasures, and/or jamming signals of varied strength is encountered, and where receiver sensitivity must be guarded from excessive gain suppression to allow reception of weak signals in the band.

CONCLUSIONS

Exposure of the wide-band traveling-wave tube to various signal environments requires a critical analysis of expected tube performance. It has been shown qualitatively that good reproduction can be obtained at small-signal levels only if no overdriving extraneous signals exist in the same band. Furthermore, in the presence of large overdriving signals which require reduction of signal suppression, improved operation can be achieved with the use of multiple attenuators.

In various other applications in which signal-suppression characteristics may be desired, single lumped attenuators, a hollow beam, and good circuit coupling would undoubtedly yield the best results. In any of the aforementioned applications, however, the use of transfer curves to accommodate a wide variation of signal environment provides a method for predicting output results.

ACKNOWLEDGMENT

The author gratefully acknowledges the major contributions of E. Kinaman to the work described in this paper, and also the help of R. Lorentzen who made many of the measurements presented.

THERMOELECTRIC AIR CONDITIONER FOR SUBMARINES*

BY

J. R. ANDERSEN

RCA Defense Electronic Products,
Camden, N. J.

Summary—*The results thus far obtained in a program of design and experimental development of a thermoelectric air conditioner for submarines are reviewed. The basic design concept is discussed in terms of performance, pressurization, sea-water corrosion, and simplicity. A working theory which expresses the performance of a "real" thermoelectric refrigeration machine leads to a discussion of the design parameters for such a machine. The results of design optimization studies are then displayed showing, specifically, the size of the machine and the weight of thermoelectric material required as a function of maximum coefficient of performance for a variety of thermopile configurations. The final design, based on these considerations, is presented and its expected performance is discussed. Experimental performance data obtained from a one-ton model, constructed according to this design, is discussed and compared with predicted performance, and some difficulties in implementing the design concepts are mentioned. It is concluded that large-capacity, compact thermoelectric air conditioners for special applications are feasible at the present state of the thermoelectric art.*

INTRODUCTION

THE objective of this program was to determine feasibility, design, and develop an experimental thermoelectric air conditioner for use in submarines. In addition to an analysis of potential performance, consideration was given to size, weight, submergence pressurization, sea-water corrosion, reliability, maintenance, control, and serviceability. Specifically, it was proposed to design a central refrigeration plant to replace the mechanical unit in an existing submarine air-conditioning system. This plant would produce chilled water at 50°F with an inlet temperature of 85°F.

BASIC DESIGN CONCEPT

The design configuration that appeared to best fulfill the requirements was a unit in the form of a modified shell-and-tube heat ex-

---

* Manuscript received 28 February, 1961.

changer, the active thermoelectric elements being built into the tubes. A cutaway drawing of this arrangement is shown in Figure 1. Chilled water flows inside the tubes and the sea water is on the shell side. This configuration was dictated mainly by the desire to alleviate sealing problems and to provide a structure which would support the pressurization loads without subjecting the thermopile modules to these loads. Subsequent experience has not indicated any necessity to alter this basic design philosophy.

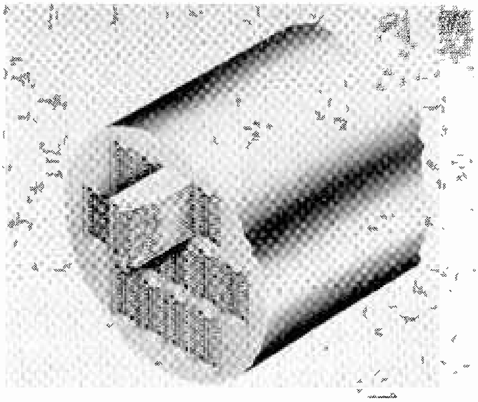

Fig. 1—Thermoelectric air conditioner shell and tube arrangement.

The final design consists of several identical units, each having a nominal capacity of ten tons of refrigeration. Each unit will be contained in a pressure vessel 20 inches in diameter and 10 feet long and will contain 30 identical tube subunits, substantially identical to the units used in the model described later.

IDEALIZED THERMOELECTRIC REFRIGERATOR

The basic relations for the steady performance of an idealized thermoelectric refrigerator are well known. Assuming that the thermoelectric properties are independent of temperature, these relations are

$$q = -\frac{1}{2}\rho l i^2 + eT_1 i - \frac{k}{l}(T_0 - T_1) \tag{1}$$

$$p = \rho l i^2 + e(T_0 - T_1)i \tag{2}$$

$$\phi = \frac{q}{p}. \tag{3}$$

where q = refrigeration density

ρ = resistivity of the thermoelectric material

l = thermoelement length

i = current density

e = thermoelectric power

k = thermal conductivity of the thermoelectric material

T_0 and T_1 = hot- and cold-junction temperatures, respectively

p = power input density

ϕ = coefficient of performance of a refrigeration machine

The first term of Equation (1) expresses that part of the Joule heat generation, caused by the current passing through the thermoelement, which is returned to the cold junction. The other half of the Joule heat appears at the hot junction. The second term is the Peltier cooling at the cold junction. The third term is the rate of heat conduction to the cold junction due to the temperature difference between the hot and cold junctions. The first term of Equation (2) is the total rate of Joule heat generation. The second term is the power required to overcome the Seebeck voltage generated by the temperature differential between the hot and cold junctions of the thermocouple circuit. Equation (3) defines the coefficient of performance of a refrigeration machine.

While Equations (1) through (3) completely describe the performance of an idealized thermoelectric refrigeration machine, they are not in suitable form to display the performance characteristics in terms of convenient experimental parameters. The relevant performance parameter is the figure of merit, Z, of an idealized thermocouple. The figure of merit is defined as $Z = e^2/\rho k$ and is arrived at in the following manner: the maximum cooling for a given temperature differential $(T_0 - T_1)$ is obtained with a current density for which $dq/di = 0$. This gives $i = eT_1/\rho l$. The maximum temperature differential obtainable, $(T_0 - T_1)_{\max}$, is then obtained by setting $q = 0$. The result is

$$(T_0 - T_1)_{\max} = \frac{1}{2} \frac{e^2}{\rho k} T_1^2 \tag{4}$$

or

$$(T_0 - T_1)_{\max} = \frac{1}{2} Z T_1^2. \tag{5}$$

The figure of merit is an experimental measure of the quality of thermoelectric materials for refrigeration applications and it is easily obtained by a measurement of the maximum temperature differential under conditions of no net heat transfer at the cold junction. In a similar way, an expression for the maximum coefficient of performance of an idealized thermoelectric refrigerator is obtained in the well known form

$$\phi_{\max} = \frac{T_1 \sqrt{1 + \frac{1}{2} Z (T_0 + T_1)} - \frac{T_0}{T_1}}{(T_0 - T_1) \sqrt{1 + \frac{1}{2} Z (T_0 + T_1)} + 1}. \tag{6}$$

PERFORMANCE OF A "REAL" THERMOELECTRIC REFRIGERATOR

Equations (5) and (6) show that the performance of an idealized thermoelectric refrigerator is independent of the length of the thermoelements. This conclusion is not true if the contact resistance at the thermocouple junctions is considered. If the contact resistance, R, is assumed to be equally divided between the hot and cold junctions, Equations (1) and (2) become, respectively,

$$q = -\frac{1}{2} (\rho l + 2R)\, i^2 + e T_1 i - \frac{k}{l} (T_0 - T_1) \tag{7}$$

$$p = (\rho l + 2R)\, i^2 + e\, (T_0 - T_1)\, i. \tag{8}$$

From these equations, the effective figure of merit, Z_{eff}, is defined as

$$Z_{\text{eff}} = \frac{Z}{\left(1 + \frac{2R}{\rho l}\right)}, \tag{9}$$

such that the maximum temperature differential obtainable is

$$(T_0 - T_1)_{\max} = \frac{1}{2} Z_{\text{eff}} T_1^2, \tag{10}$$

and the maximum coefficient of performance is

$$\phi_{\max} = \frac{T_1 \sqrt{1 + \frac{1}{2} Z_{\text{eff}} (T_0 + T_1)} - \frac{T_0}{T_1}}{(T_0 - T_1) \sqrt{1 + \frac{1}{2} Z_{\text{eff}} (T_0 + T_1)} + 1}. \tag{11}$$

Note that, with the assumption of equal contact resistance at the hot and cold junctions, the introduction of the effective figure of merit (defined by Equation (9)) leads to expressions identical in form to the idealized performance equations. The above relations assume that the thermoelectric properties are independent of temperature. However, Equation (10) can be used as a definition of a mean figure of merit over the temperature range $(T_0 - T_1)_{\max}$, and with this understanding, Equation (11) can be used to explore with sufficient accuracy the performance characteristics of a real thermoelectric refrigerator.

Making use of the definition of effective figure of merit, Equation (9), we can eliminate the current density, i, between Equations (7) and (8). The resulting expression can be put in the form

$$\frac{q}{\frac{k}{l}(T_0 - T_1)} = \frac{1}{4} Z_{\text{eff}} (T_0 + T_1) \left[\sqrt{1 + \frac{4lp}{kZ_{\text{eff}}(T_0 - T_1)^2}} - 1 \right] - \frac{pl}{k(T_0 - T_1)} - 1. \tag{12}$$

This relation suggests the definition of the following dimensionless parameters

$$q^* = \frac{ql}{k(T_0 - T_1)} \tag{13}$$

$$p^* = \frac{pl}{k(T_0 - T_1)} \tag{14}$$

$$\theta = \frac{1}{4} Z_{\text{eff}}\,(T_0 + T_1). \tag{15}$$

By using these parameters, we can put Equation (12) in the form

$$\frac{q^* + 1}{\theta} = \sqrt{1 + \frac{p^*}{\theta}\left(\frac{T_0 + T_1}{T_0 - T_1}\right)} - \frac{1}{2}\,\frac{p^*}{\theta} - 1. \tag{16}$$

The virtue of Equation (16) is that the dimensionless refrigerating capacity, $(q^* + 1)/\theta$, can be calculated in terms of the dimensionless power input, p^*/θ, and the operating absolute temperature ratio, T_0/T_1, without explicit reference to any specific properties of the thermoelements. Equation (16) is displayed graphically in Figure 2.

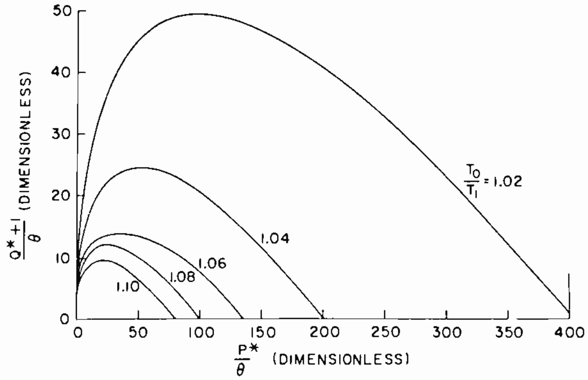

Fig. 2—Generalized thermoelectric performance function.

The following expressions for performance at particular operating conditions follow from Equations (13) through (16). The cooling capacity at maximum coefficient of performance is

$$(q^*)\phi_{\max} = \frac{4\theta\left[M - \frac{1}{2}\left(\frac{T_0}{T_1} + 1\right)\right]}{(M-1)^2\left(\frac{T_0}{T_1} + 1\right)}, \tag{17}$$

where $M = \sqrt{1 + 2\theta}$.

The maximum coefficient of performance is

$$\phi_{\max} = \left(\frac{T_1}{T_0 - T_1}\right)\frac{M - \frac{T_0}{T_1}}{M + 1}. \tag{18}$$

The maximum cooling capacity is

$$(q^*)_{\max} = \frac{2\theta T_1{}^2}{T_0{}^2 - T_1{}^2} - 1. \tag{19}$$

The power required at zero cooling capacity is

$$(p^*)_{q^*=0} = \frac{4\theta W T_1{}^2}{T_0{}^2 - T_1{}^2}\left[\left(\frac{T_0}{T_1} - 1\right) - W\right], \tag{20}$$

where

$$W = 1 - \sqrt{1 - \frac{Z\left[\left(\frac{T_0}{T_1}\right)^2 - 1\right]}{\theta}}.$$

The cooling capacity at zero power input is

$$(q^*)_{p^*=0} = -1. \tag{21}$$

Equations (16) through (21) are in convenient form to explore the performance characteristics and control aspects of a thermoelectric refrigerator.

The foregoing performance equations are expressed in terms of junction temperatures. Although these equations are adequate for some design considerations, one must ultimately consider the effect of the over-all heat-transfer coefficients at the hot and cold junctions, β_0 and β_1, respectively, in order to adequately determine the performance of a real thermoelectric refrigeration machine. As has been seen, the performance of a thermoelement module, with known junction temperatures, depends only on the effective figure of merit and current density. When a module and associated heat-transfer structures are operated between fluids of known temperature, the packing density of thermoelements in the module, η_p, becomes an important parameter of thermopile design. The over-all heat-transfer coefficient, based on unit area of thermoelement material, is inversely proportional to the packing density for a given heat-transfer structure. When it is necessary to express performance in terms of fluid temperatures, two additional relations must be satisfied,

$$q = \frac{\beta_1}{\eta_p} (T_1' - T_1) \tag{22}$$

$$q + p = \frac{\beta_0}{\eta_p} (T_0 - T_0'), \tag{23}$$

and Equation (7) is modified to become

$$q = -\frac{1}{Z} (\rho l + 2R) i^2 + eT_1 i - \frac{k_e}{l} (T_0 - T_1) \tag{24}$$

where $$k_e = k \left[1 + \frac{k_p}{k} \left(\frac{1}{\eta_p} - 1 \right) \right],$$

and k_p represents the thermal conductivity of the encapsulant. k_e accounts for the back flow of heat through the interstices between the thermopile elements.

We have not yet succeeded in obtaining a compact representation of performance in terms of given fluid temperatures such as was possible using junction temperature. Therefore, a scheme of successive approximations was used to obtain the maximum coefficient of performance for a given set of design parameters.

THERMOPILE OPTIMIZATION

Of all the parameters appearing in the performance equations, only two can be arbitrarily chosen by the designer. These are the thermoelement length, l, and the thermopile packing density, η_p. The hot and cold fluid temperatures are given. The properties of the thermoelectric material used and the junction contact resistance are determined by the state of the thermoelectric art. An extensive experimental evaluation of the performance of available thermoelectric materials and an investigation in depth of thermocouple joint-formation techniques led to the choice of the following properties as representative mean values of the best that can be achieved at the present time.

$Z = 2.80 \times 10^{-3}\ {}^\circ\mathrm{K}^{-1}$

$e = 218 \times 10^{-6}$ volt/°K

$k = 0.017$ watt/cm-°K

$R = 10 \times 10^{-6}$ ohm-cm^2

$\rho = 10.0 \times 10^{-4}$ ohm-cm

$k_p = 0.0003$ watt/cm-°K

The over-all heat-transfer coefficients of the hot and of the cold sides require further discussion. The most important of these, as well as the one most subject to unavoidable limitation due to the environmental considerations of pressure and corrosion is the heat-transfer coefficient of the hot, or sea-water, side. The preferred material is 70-30 cupro-nickel, and the calculations given in the paper are based on its properties. The thermal resistance of the electrical insulation between the thermopile connector bars and the heat-transfer structure is another important limiting factor on the over-all heat-transfer coefficient. After considerable experimental effort to find the best method, it was finally decided to use a layer of aluminum oxide (the so-called Martin* hardcoat) formed on an aluminum plate and attached to the thermopile by a thin layer of epoxy cement. The heat-transfer structure adopted was considered to be a good compromise between the thermal and structural requirements. The fluid velocity between the finned heat-transfer surfaces was adjusted to give the optimum balance between increased surface heat-transfer coefficient and pressure drop. The over-all maximum coefficients of performance presented include the fluid pumping power as part of the power input to the machine.

The results of these optimization computations are shown in Figures 3 and 4. Figure 3 shows the weight of thermoelectric material required per ton of refrigeration and the over-all maximum coefficient of performance as functions of the two module design parameters, thermoelement length and module packing density. Figure 4 shows

---

* Registered trade mark.

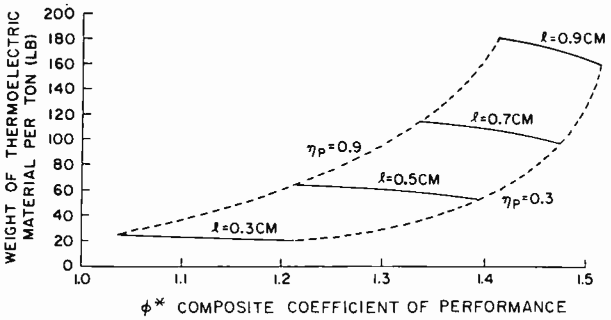

Fig. 3—Thermoelectric material and coefficient of performance versus module parameters.

the volume per ton of refrigeration and the over-all maximum coefficient of performance as functions of these same two parameters. It is interesting to note the large changes in performance, volume, and amount of thermoelectric material required for a given refrigeration capacity resulting from relatively small changes in thermopile configuration. The final configuration chosen as best compromise between these values was $l = 0.5$ centimeter and $\eta_p = 0.5$.

FINAL DESIGN AND MODEL

The final refrigeration plant will consist of several individual units, each having a nominal cooling capacity of ten tons of refrigeration at design conditions and containing 30 identical tube subunits in a pressure vessel 20 inches in diameter and 10 feet long.

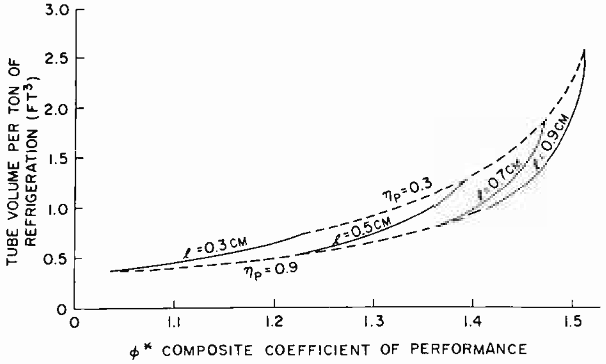

Fig. 4—Volume and coefficient of performance versus module parameters.

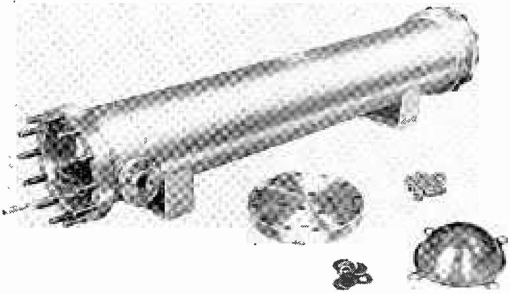

Fig. 5—One-ton thermoelectric air conditioner.

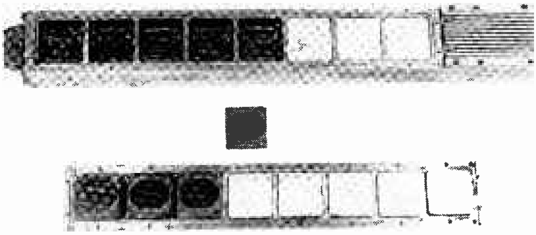

Fig. 6—Thermoelectric air conditioner subunit.

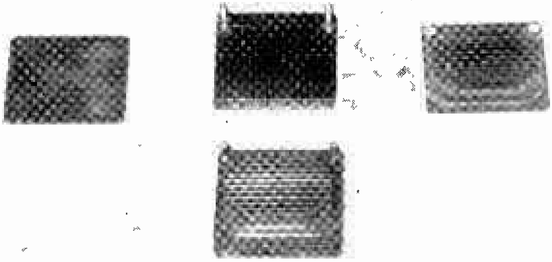

Fig. 7—Thermopile module.

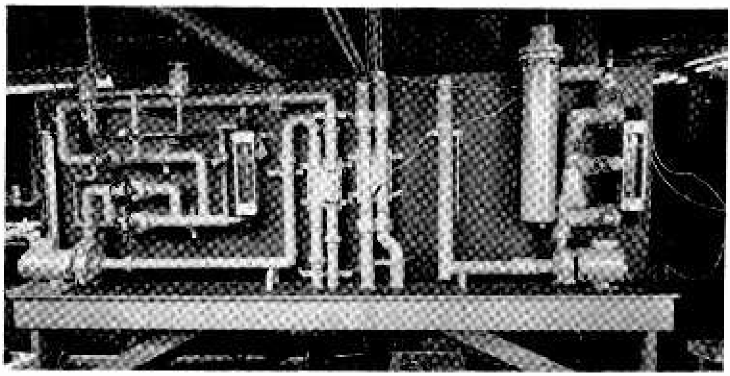

Fig. 8—Apparatus for testing one-ton air-conditioner model.

A one-ton model of this design has been constructed. It contains six tube units (identical in design to that for the final unit) five feet long, and contained in a pressure vessel 10 inches in diameter. Figure 5 shows this model partially assembled. One tube unit partially assembled is shown in Figure 6, and a single thermopile module is shown in Figure 7. Each five-foot tube of the one-ton model contains 48 thermopile modules, each module containing 18 thermocouples. Each module is 2 × 2 inches in cross-section, with integral heat-transfer extended surface on the chilled water side. The thermoelements are 0.7 centimeter in diameter and 0.5 centimeter long. The

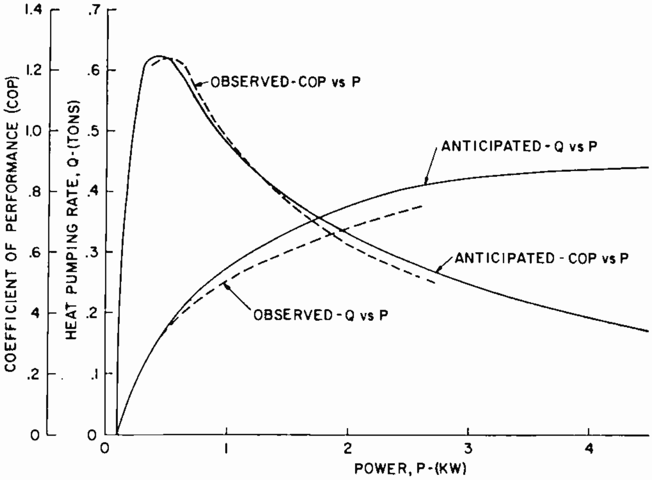

Fig. 9—Anticipated and observed performance characteristics.

sea-water tube structure is aluminum bronze 3.06 inches by 2.29 inches in cross section. The hot-side fin plates and end bells are pressure-sealed with O-rings. The modules are electrically connected in series and are of the plug-in type for easy disassembly and maintenance. The pressure vessel is stainless steel.

One tube of the one-ton model has been tested for performance. Figure 8 shows the double test loop used for performance evaluation. Figure 9 shows the performance data thus far obtained with this tube. Figure 9 also shows the performance predicted from the design computations. The substantial agreement between the predicted and realized performance is gratifying.

The only difficulties encountered in implementing this design were some minor water-sealing problems on the chilled water side and unreliability of the electrical insulation on the thermopile modules. The sealing problem has been corrected. A short circuit to ground through the thermopile insulation on one of the modules occurred when the tube was being operated near its maximum cooling capacity and after the tube had been under test for about 40 hours. The adequacy of aluminum oxide films for electrical insulation is being investigated.

It is concluded that large-capacity, compact thermoelectric refrigeration machines having adequate performance can be built utilizing present thermoelectric art, and that this performance can be reliably predicted.

ACKNOWLEDGMENT

The project on which this paper is based was supported by the U. S. Navy, Bureau of Ships. This support is gratefully acknowledged. In addition, the work could not have been accomplished without the contributions of my co-workers—L. Pessel, E. Farmer, R. Johnston, M. Crouthamel, B. Shelpuk, and H. Walter.

THE HIGH-BEAM-VELOCITY VIDICON*

By

J. Dresner

RCA Laboratories
Princeton, N. J.

Summary—*One of the barriers to the construction of Vidicons with high sensitivity and fast response is the phenomenon of capacitive lag which, when the scanning beam lands at low velocity, necessitates the use of porous photoconductors having generally low sensitivity. It is demonstrated that this capacitive lag can be reduced to a very low value by making use of a scanning beam landing at high velocity. It is then possible to utilize glassy photoconductive layers of high sensitivity and large capacitance.*

The redistribution problems associated with high-beam-velocity operation are studied in detail. Means are described by which they can be reduced to the point where their effect on image quality is minimal.

An experimental tube has been constructed which uses a glassy Sb_2S_3 photoconductive layer with a capacitance of 8000 picofarads. The speed of response with a high-velocity beam is considerably faster than with a low-velocity beam. The image quality is adequate for many purposes.

INTRODUCTION

THE VIDICON is a television camera tube in which a photoconductive layer of high resistivity serves both as a light-sensitive element and as a storage target.[1] As in most modern camera tubes, the storage target is scanned by an electron beam which lands at near zero velocity. This paper considers the operation of a Vidicon where the beam lands at high velocity, i.e., the secondary-emission ratio from the scanned surface is greater than unity.

A photoconductive layer suitable for use as a Vidicon target must have a high resistivity, the proper spectral response, a high sensitivity, and a fast speed of response. One of the best materials available for these targets is a glassy layer of amorphous antimony trisulfide. While such a thin evaporated layer can be made very sensitive, its maximum usable thickness is approximately 2 microns, which results in a capacitance of the order of 10,000 picofarads. When a high-capacitance layer is used in conjunction with a scanning beam landing

---

* Manuscript received 16 March, 1961.

[1] P. K. Weimer, S. V. Forgue, and R. R. Goodrich, "The Vidicon Photoconductive Camera Tube," *Electronics*, Vol. 23, p. 70 (1950).

at low velocity, the phenomenon of capacitive lag occurs because of the inability of the beam to discharge the target fully after each frame time, and the response time of the device drops below the useful limit. To circumvent this limitation, use is made of porous layers of antimony trisulfide (evaporated at a pressure of approximately 1 mm Hg) which have a capacitance of the order of 1000 picofarads and, thus, are not subject to serious capacitive lag. However, these porous layers are generally of lower sensitivity than the glassy films. This is probably caused principally by the large ratio of surface area to volume present in the porous structure, which implies a large number of recombination centers and a short lifetime for the photoexcited carriers. In addition, the target will exhibit photoconductive lag which may, in some cases, be so long as to dominate the response time of the device. It is shown below that operation of a Vidicon in the high-beam-velocity mode makes possible the elimination of capacitive lag and may open the way for the practical utilization of glassy Sb_2S_3 layers of high sensitivity and high capacitance.

The phenomenon of capacitive lag has been studied by several investigators and is well understood.[2-4] For small values of the target voltage, V_t, the current flowing into the target is

$$I_t = a \exp \{bV_t\},$$

where a is proportional to the total beam current. By setting the parameter $b = e/kT$, an effective temperature can be assigned to the electron beam. It is usually found that the measured value of b corresponds to a temperature much larger than that of the cathode of the electron gun. This difference can be attributed to an additional spread in the axial velocities of the electrons introduced by the aberrations of the electron-optical systems. The various authors all assume an exponential shape for the beam-landing curve and arrive at similar results. The methods used differ in the way in which the charging of a target element by the scanning beam is treated, or in the use of "flood beam" approximations in which the beam is assumed to spray the entire target with electrons after each frame time. Their

---

[2] R. W. Redington, "The Transient Response of Photoconductive Camera Tubes Employing Low-Velocity Scanning," *Trans. IRE PGED*, Vol. 3, July 1957.

[3] L. Heijne, *Acta Electronica*, Vol. 2, p. 124 (1957).

[4] B. Meltzer and P. L. Holmes, "Beam Temperature, Discharge Lag, and Target Biasing in Some Television Pick-Up Tubes," *Brit. Jour. Appl. Phys.*, Vol. 9, p. 139 (1958).

conclusions state that capacitive lag can be minimized by reducing the target capacitance and by increasing the value of b. This last condition is equivalent to requiring a large value of the beam conductance, dI_t/dV_t near the equilibrium potential of the scanned surface. It can also be shown that the lag behavior cannot be improved by increasing the total beam current, at least where the beam-landing curve is exponential.

If the target capacitance is to be large, some means must be found to increase the beam conductance. This could be done by reducing the energy spread of the electrons in the beam. A reduction of the cathode temperature to obtain a narrower distribution of thermal energies is not advantageous, however, unless an improvement is also made in the optics of the electron gun. It is doubtful, moreover, that the improvement in beam conductance obtained in this way would be sufficiently large to permit the use of glassy photoconductive layers. During the past decade, there have been many other attempts to circumvent the capacitive-lag problem. One approach was that of the miniature Vidicon,[5] where the scanned area was reduced by a factor of four, with an equivalent reduction in capacitance. This approach has limited use, because the signal decreases with the target area for a fixed-scene illumination and because the resolution is reduced by miniaturization. Another scheme that has been proposed is the bridge-type target, in which the potential of the surface is re-established independently of the scanning beam.[6] This requires the use of an intricate electrode structure which is difficult to manufacture and which inherently limits the resolution. The differential lag compensation scheme[7] requires either the use of two Vidicons, or of a structure-type target with two photoconductors having different decay times. The RC lag compensation method[8,9] is more attractive, since it does not require structure in the target. In this method, an auxiliary layer is evaporated on the scanned side of the photoconductor. If the resistivity and dielectric constant of this auxiliary layer are

---

[5] A. D. Cope, "A Miniature Vidicon of High Sensitivity," *RCA Review*, Vol. 17, p. 460, December 1956.

[6] S. A. Cchs and P. K. Weimer, "Some New Structure-Type Targets For the Vidicon — An Analysis of Their Operation," *RCA Review*, Vol. 19, p. 49, March 1958.

[7] H. Borkan and P. K. Weimer, "Differential Method of Lag Compensation in Photoconductive Devices," *RCA Review*, Vol. 19, p. 62, March 1958.

[8] H. Borkan, unpublished work.

[9] J. A. Cksman and M. V. Epifanov, "On the Question of Sluggishness of Photoresistive Camera Tubes of the 'Vidicon' Type," *Radiotechnika i Elektronika*, Vol. 3, p. 1501 (1958).

properly selected, an increase in the speed of response is obtained. In practice, however, it has proven very difficult to evaporate auxiliary layers with the correct properties.

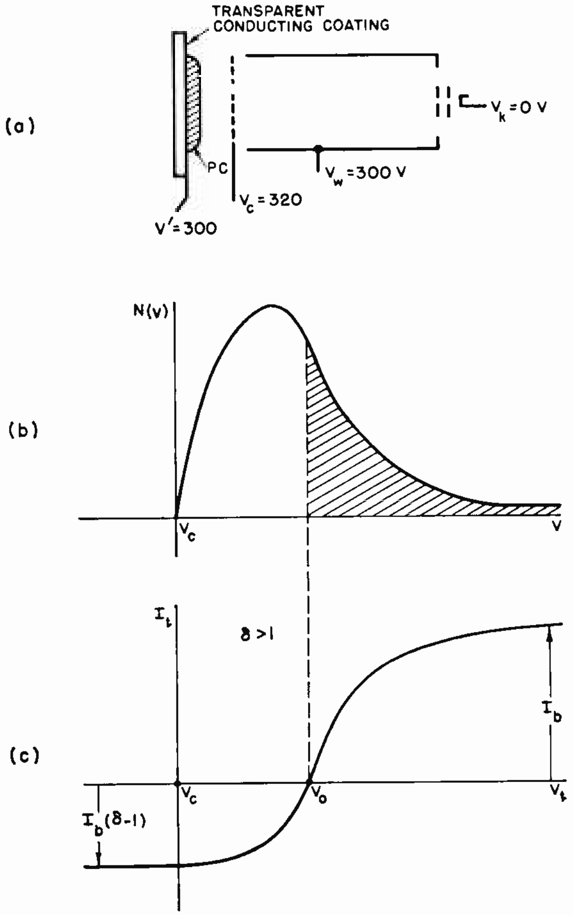

Fig. 1—Scanning with high-velocity beam: (a) experimental arrangement, (b) energy distribution of secondary electrons, and (c) effective beam-landing curve.

HIGH BEAM VELOCITY

Figure 1a shows the arrangement of electrodes for high-beam-velocity operation, with typical values for the applied potentials. The only difference from the standard low-beam-velocity Vidicon that concerns us at present is the high voltage, V', applied to the transparent conducting electrode. In the following analysis, redistribution effects do not come into play; they are discussed later. The beam finds the photoconductive layer at $V_t \approx V'$, and hence lands with an energy sufficiently high to produce a secondary emission $\delta > 1$. The energy distribution of the secondary electrons produced at the target is plotted in Figure 1b, with the collector voltage, V_c, taken as reference voltage. The figure only shows the general features of the distribution of low-energy secondaries and covers a range of kinetic energies from 0 to approximately 10 ev. The peak of the distribution is, in actuality, closer to the origin than has been shown here. The elastically scattered primary electrons which would produce a sharp peak in the curve at an energy of about 300 ev are few in numbers and are not shown. Figure 1c shows the electron current flowing into the target as a function of the target voltage, V_t, under the above conditions. When the target is driven very positive with respect to the potential of the collecting mesh, the secondary electrons are unable to leave and the current will be that in the incoming beam, I_b. When $V_t \leq V_c$, all secondary electrons can be collected, and the current saturates to a value $-I_b(\delta - 1)$. The target current is given by

$$I_t = I_b \left[1 - \delta \int_{V_t}^{\infty} N(V)\,dV \right], \qquad (1)$$

where

$$\int_0^{\infty} N(V)\,dV = 1.$$

The surface of an insulating target will become charged to a potential V_0, such that the net current into it is zero, i.e., all secondary electrons in the shaded area of Figure 1b are collected by the mesh. According to this picture, the surface of the photoconductor tends to stabilize at a voltage near V_0, as determined by the collector voltage, V_c, and lying a few volts above it. For a fixed V_c, the potential across the photoconductor depends on the voltage V' applied to the transparent electrode, and the photocurrent can be made to flow in either direction according to whether V' is larger or smaller than V_0. For a small dark current, the beam will thus find the target at a potential in the vicinity of V_0. From Equation 1, one obtains

$$\frac{dI_t}{dV_t} = \delta I_b N(V_0), \qquad (2)$$

which gives the beam conductance at V_0 as a function of the beam current and the secondary electron distribution. It is obvious that the beam conductance can be made arbitrarily high by increasing I_b sufficiently. According to the previous discussion, the capacitive lag can then be reduced by increasing the beam current. This situation is in sharp contrast to that at low velocity where the capacitive lag is, to first order, independent of the total beam current.*

The use of high beam velocity thus offers a simple solution for the capacitive lag problem, according to Equation (2). The requirements for the secondary emission from the scanned target are not critical, as long as $\delta > 1$. A very large value of δ is not necessarily desirable because V_0 might then be shifted towards higher values of V_t (Figure 1c), in a region where $N(V)$ decreases rapidly. Since it is desirable to have the greatest values of dI_t/dV_t occur near the equilibrium potential, V_0, it is still helpful to have a scanned surface which produces a narrow energy range for the secondary electrons. Then, for a fixed δ, V_0 would be located at the peak of the electron distribution curve. In practice, one has no control over the value of δ or the shape of the function $N(V)$, since the material of the sensitive target is selected on the basis of its photoconductive properties. It is shown below that under certain conditions the beam conductance can be made to depend on the δ and $N(V)$ associated with the secondary emission from the collector mesh. This introduces more freedom in the selection of those parameters.

In the derivation of Equation (2), it was assumed that all secondary electrons were ejected normal to the scanned surface, so that those collected by the mesh could be represented by the shaded area in Figure 1b. In reality, the number of secondaries emitted per unit solid angle follows a cosine distribution. In Figure 2a, we consider the path of a secondary electron having an energy V above the collector potential V_c and emitted at an angle θ from the normal. The requirement for collection is that the axially directed component of the kinetic energy

$$\frac{1}{2} mv^2 \cos^2 \theta \geqq V_T.$$

Of all the electrons having an energy V, only those emitted within a cone θ_0 will be collected, where

---

* At low velocity, raising the beam current may actually worsen the lag because of the concomitant increase in effective beam temperature. This effect is not well understood.[4]

$$\cos^2 \theta_0 = \frac{V_T}{V}.$$

The fraction of electrons having an energy V which are collected is

$$F(V) = 1 - \frac{V_T}{V}.$$

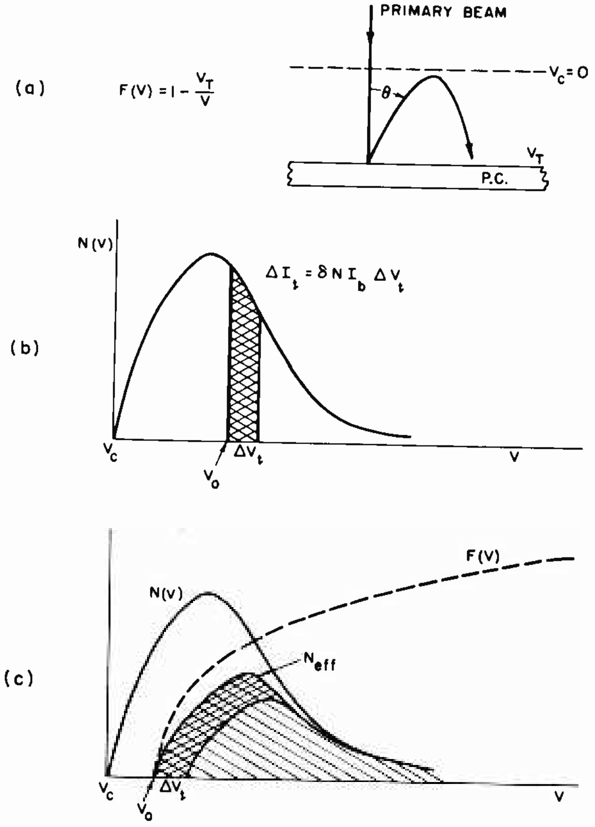

Fig. 2—Effect of a cos θ distribution of the secondary electrons on the beam conductance.

Equation (1) must then be corrected to read

$$I_t = I_b \left[1 - \delta \int_{V_t}^{\infty} N(V) \left(1 - \frac{V_t}{V} \right) dV \right], \tag{3}$$

and the beam conductance becomes

$$\frac{dI_t}{dV_t} = I_b \delta \int_{V_t}^{\infty} \frac{N(V)}{V} dV. \tag{4}$$

The dependence of the beam conductance on the beam current, I_b, is the same as in the simpler Equation (2). In the absence of an analytical expression for $N(V)$, Equation (4) cannot be solved. However, the effect of the angular distribution of velocities on the beam conductance can be found in a qualitative way. In Figure 2b, we consider the case of electron emission normal to the scanned surface, with that surface at the equilibrium potential V_0. Upon a change of potential, ΔV_t, there will be a current change, $\Delta I_t = \delta N I_b \Delta V_t$. This change is given by the contribution of the secondary electrons represented by the shaded area. In Figure 2c, the effect of the incomplete collection of secondaries is taken into account for a target at V_0. The dashed line gives the collection function $F(V)$. Only those electrons represented by the area under the curve N_{eff} will be collected by the mesh. The equilibrium potential V_0 will then be displaced towards a lower value in order to balance the incoming beam current. The change in current ΔI_t for a potential change ΔV_t is furnished by the electrons represented by the cross-hatched area. It is clear that this area will, in general, be smaller than in Figure 2b, and the beam conductance will be decreased proportionately. The decrease in the beam conductance to be expected because of this effect is not very severe, and is probably of the order of 50 per cent.

Another important effect occurring during the operation in the high-velocity mode is that of secondary electrons emitted from the collector mesh. We characterize this emission by an effective emission coefficient δ_c, taking into account only those secondaries which are emitted towards the scanned surface and can be collected by it. Electrons emitted in the backward direction can be collected by other electrodes in the system and do not come into play. For simplicity, rectangular energy distributions of secondaries from the target and the mesh have been assumed in Figure 3a. Since the secondaries from the mesh are emitted forward, their energy distribution extends towards negative values of V_t. The contributions of both sources of secondary electrons to the target current are given by the dashed lines in Figure 3b. When the scanned surface is driven to large values of V_t, the current saturates to I_b $(1 + \delta_c)$. Towards large negative values of V_t, no secondaries from the mesh can land on the target and the current saturates to the same value as previously, $I_b(\delta - 1)$. From inspection of Figure 3b, it is clear that the target surface can stabilize itself at a value of $V_0 < V_c$ provided $\delta_c > \delta - 1$, a condition that is easily satisfied in practice. Measurements on an experimental high-beam-velocity Vidicon have shown V_0 to lie about 5 volts below V_c. In this case, the beam conductance in the vicinity of V_0 is controlled by the energy distribution of the mesh secondaries and by δ_c. Some control of δ_c and $N(V)$ can be achieved independently of the target material when the tube is operating in this manner. For example, a high value of δ_c, could be obtained by using a copper mesh with an oxidized surface as the collector.

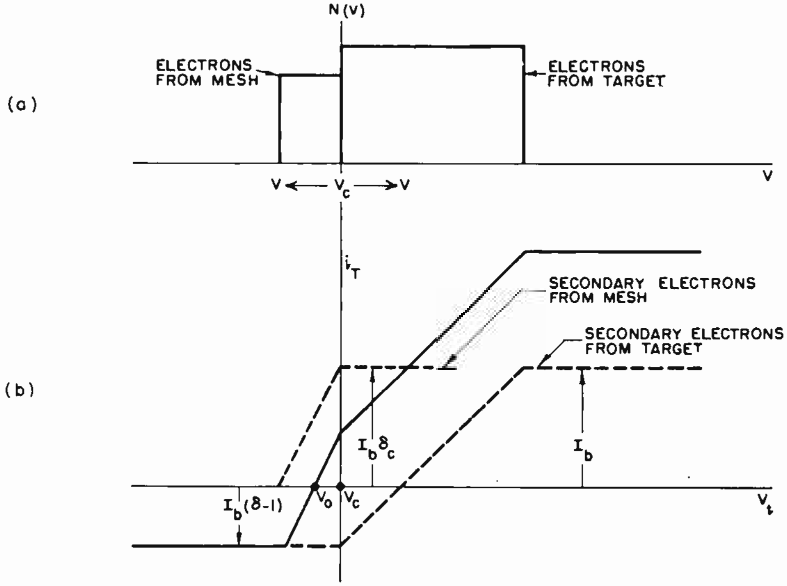

Fig. 3—Effect of secondary electrons emitted from the mesh. When $V_0 < V_c$, the beam conductance is controlled by the secondary electrons from the mesh.

THE REDISTRIBUTION PROBLEM

Before the high-velocity mode of operation can be used in a practical tube, there are three problems to be solved. These concern the quality of the image.

When a low-velocity beam is used for scanning, the image quality is not very sensitive to small defects in the surface of the target. Furthermore, the decelerating mesh need not be placed very close to the target surface, so that it is out of focus and its defects do not show in the image. With high beam velocity, however, surface defects, particles of foreign matter, or any other conditions which can result in local variations in the secondary emission of the scanned surface appear in the image. Also, the collector mesh must be placed very close to the scanned surface, so that it appears in the image. Thus the mesh must also be free of defects and nonuniformities. This problem can be solved by exercising proper precautions during the fabrication of the tube.

A more serious problem in maintaining image quality is caused by the nonuniform redistribution of the uncollected secondary electrons. Since most secondary electrons are ejected at an angle to the normal, the uncollected portion returns to the target at some distance from the point of origin. This situation is illustrated on the left side of Figure 4a for an electron ejected at an angle θ. For a velocity v the range is given by

$$R = \frac{2md}{e(V_T - V_c)} v^2 \cos\theta \sin\theta, \qquad (5)$$

where d is the target-to-mesh spacing, m the electron mass, and e the electronic charge. The secondaries are then sprayed within a radius R of the beam's point of impact. The parts of the target within R of the edges of the scanned area receive fewer secondaries than the center. They thus charge up to a different value of V_0 than the center, which gives rise to a nonuniformity of the dark current. In a standard Vidicon, such as the 7038, the mesh is located about 3 millimeters from the scanned surface. For a representative value of $V_T - V_c$ of 3 volts, a secondary electron of 5 ev emitted at 45° from the normal will land 1 centimeter away from the beam's point of impact. The nonuniformity in the dark current can thus extend over a large part of the scanned area and be so severe as to preclude the use of the standard Vidicon geometry in the high-velocity mode. In the case where the lag is controlled by the secondary electrons from the mesh, and V_0 is less than V_c, only these electrons contribute to nonuniformity in the dark current, since the secondaries from the target are all collected. The mesh electrons of a given energy emitted at an angle θ will then influence the target potential over a distance $R/2$ as shown on the right side of Figure 4a. The situation for mesh-controlled lag is thus more favorable for minimizing redistribution effects. It is obvious from Equation (5) that the nonuniformity in the dark current can be reduced by bringing the collector mesh very close to the scanned surface. This is also the situation where the control of lag by the mesh secondaries is most likely to occur. If the mesh is to be close to the target, it will appear in the image, and must therefore be fine enough so as not to degrade the resolution. The finest commercially available mesh has 750 lines/inch, with the spacing between wires of about 0.001 inch. In order that the field between the scanned surface and the collector be determined wholly by the collector potential, the mesh must be several times this spacing away from the surface. A value of $d = 0.005$ inch has been found satisfactory. With this value of d and assuming that the mesh secondaries control the lag, as was found in practice, R is reduced by a factor of 50 compared to the standard Vidicon geometry.

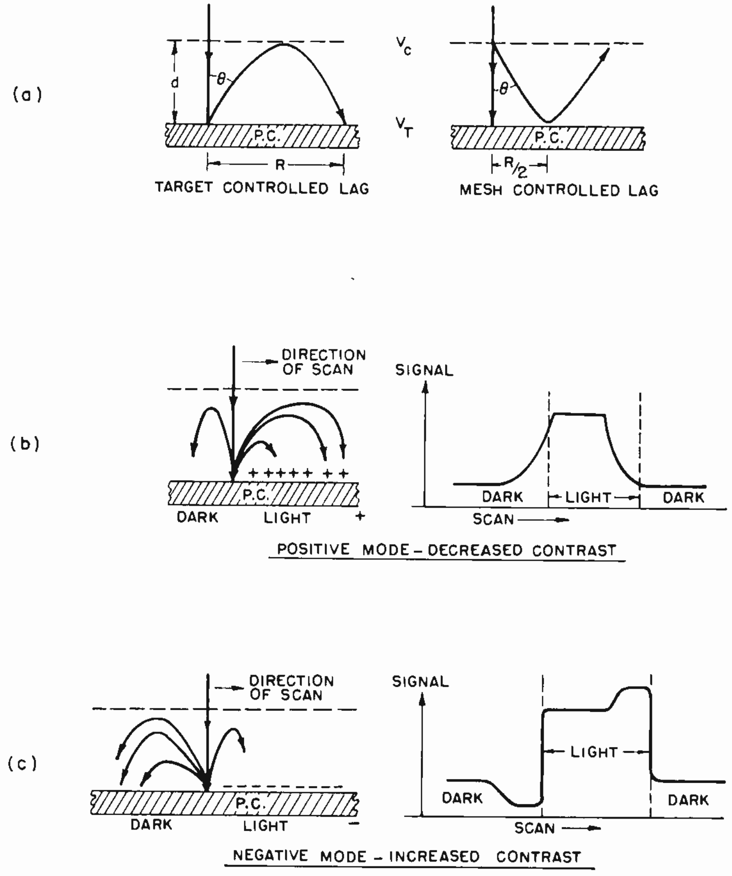

Fig. 4—Effect of the asymmetrical redistribution of secondaries on the image contrast.

Another important redistribution effect which makes a large contribution towards determining the contrast near the edge of an illuminated area is associated with the direction of scanning. We consider first a tube operating in the positive mode ($V_t > V_0$). The target surface then charges up positively under the influence of light or of the dark conductivity. The secondary electrons tend to land preferentially on the unscanned portions of the target, which are more positive (Figure 4b). As the beam approaches the edge of an illuminated area, the fraction of secondaries landing ahead of the beam increases. Since the secondaries drawn over the unscanned area have a smaller probability of reaching the mesh, the beam must drive the target area at the point of impact to a lower value of V_0 than over the rest of the dark area (see Figure 1). The potential difference across this part of the target is larger, and the signal thus increases as the illuminated area is approached, reducing the contrast at the edge (Figure 4b). As the beam approaches the far edge of the illuminated area, the fraction of secondaries which can reach the mesh suddenly increases. The beam then brings that area to a higher value of V_0 and the potential difference applied to the photoconductor decreases, thus reducing the signal within the illuminated edge.

The situation in the negative mode of high-beam-velocity operation ($V_t < V_0$) is shown in Figure 4c. There the secondary electrons tend to be repelled away from the unscanned area and to land behind the beam. As the illuminated area is approached, this repulsion increases. By the same argument as in the positive case, V_0 becomes lower near the edge. In this case, however, the potential across the photoconductor is decreased and the dark current becomes smaller outside the illuminated edge. On the far side of the illuminated region, the signal current increases just inside the edge. Thus, in the negative mode, edge contrast is increased.

It is clear that these redistribution phenomena affect the signal only when the beam is within a distance of the order of R from the edge of an illuminated area. The positive mode redistribution has the most deleterious effect on image quality. With the standard Vidicon geometry (where R may be as much as 1 centimeter), it is usually impossible to obtain any image in this mode. In the negative mode, the situation is more favorable, although there is a tendency for saturation of highlights and dark areas at high levels of illumination. As the collecting mesh is brought closer to the scanned area, both of these effects decrease. For a 750 line/inch mesh at 0.005 inch from the surface, they are reduced to the point where they have only a small effect on the image quality except at very high light levels.

The solution to most of the redistribution problems encountered in the high-beam-velocity Vidicon thus appears to lie in finer collecting meshes spaced closer to the scanned surface. The 750 line/inch mesh used in the present experimental tubes has proved satisfactory, although it is probable that an increase in the ultimate resolution capability of the tube would be obtained by the use of 1000 line/inch mesh.

There is another effect which must be eliminated before images of commercial quality can be produced by the high-beam-velocity Vidicon. In the previous discussion, it has been assumed that all secondary electrons leaving the surface with the proper energy and direction would be collected. As they approach the interstices of the mesh, however, the field they see is determined not only by V_c but also by the potential distribution on the far side of the mesh. In order to insure a uniform collection efficiency over the image field, it is necessary for the equipotentials to be flat on the beam side of the mesh. Failure to satisfy this requirement will result in variations of dark current at the edges of the field. This effect can be reduced by addition of apertures to the wall and collector electrodes, as described later in the discussion of the experimental tube.

EXPERIMENTAL TEST OF THE THEORY

Experiments were designed to test the validity of Equation 4, and to see how much improvement could be effected in the beam conductance by high-beam-velocity operation. They were performed either in a demountable test set or in a standard Vidicon in which the photoconductor had been replaced by a conducting target. Figure 5 shows some of the beam-landing curves obtained in a 7038 Vidicon with a tin-oxide-coated glass target. The vertical line at 5 volts indicates a change of scale in the target voltage. At low velocity, a value of $b = 2.9$ is obtained in the steepest part of the curve, decreasing for lower current values. This curve was taken with a relatively large beam current. If the beam current were reduced and the alignment of the magnetic field properly adjusted, a value of b as high as 6 could be measured in the steepest part of the curve. However, it is generally undesirable to have dark currents much in excess of 2×10^{-8} ampere, and, in this operating range, b would be much reduced for a low-velocity beam. Beam-landing curves are shown at high-beam-velocity negative operation for two values of the total beam current. These give values of $b = 7.7$ and $b = 23$ in the region of interest. Since the time constant for capacitive lag is inversely proportional to b, an increase in speed of the order of 10 can be expected by operating at high velocity. The curves show an important characteristic of the high-velocity beam, namely, that the beam conductance has its maximum value near V_0, where it does the most good.* The value of V_0 shifts slightly as the beam current is decreased. This has been observed on surfaces of all the materials tested. The most

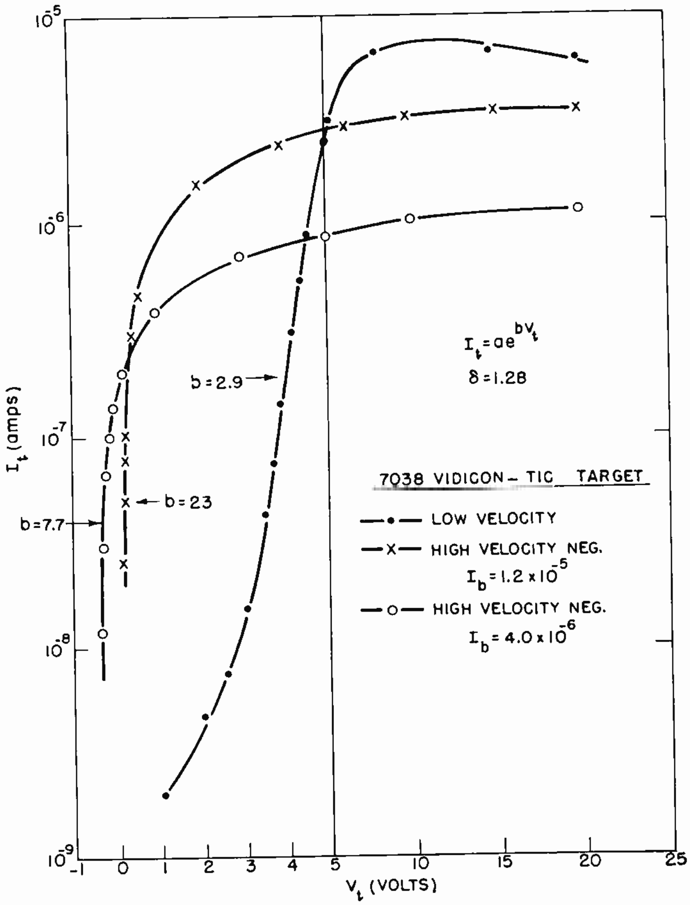

Fig. 5—Beam-landing curves for low- and high-velocity beams. For the latter case, V_0 has been located at an arbitrary point on the abscissa. These measurements were made on a 7038 Vidicon with a conducting glass target.

---

* In measuring the high-velocity curves, the target was biased near 300 volts. The value of V_0, where the current changes direction, was located at an arbitrary value on the abscissa of Figure 5 to facilitate comparison with the low-velocity curve.

probable explanation for this effect is a change in the distribution function $N(V)$ of the secondary electrons brought about by the increased amount of transverse velocities in the higher intensity beam. This effect does not come into play during the operation of the tube, since the beam current is fixed.

Table I gives the results of some beam-conductance measurements

Table I—Beam Conductance Measurements
(Primary Beam Energy = 300 volts)

	I_b (amp)	$\left(\frac{dI_t}{dV_t}\right)$ (mho)	$\eta \times 100$	δ	
Tin Oxide Coating on Glass	1.2×10^{-5}	1.3×10^{-6}	10	1.28	Sealed Tube
	4.0×10^{-6}	3.3×10^{-7}	8.3	1.28	Sealed Tube
	2.2×10^{-6}	2.0×10^{-7}	9.1	1.63	Demountable Test Set
	1.1×10^{-6}	1.3×10^{-7}	11	1.63	Demountable Test Set
	5.0×10^{-7}	6.3×10^{-8}	12	1.68	Demountable Test Set
Al Foil	2.1×10^{-6}	8.9×10^{-8}	4.3	1.62	Demountable Test Set
	9.4×10^{-7}	5.0×10^{-8}	5.3	1.54	Demountable Test Set
	2.7×10^{-7}	2.1×10^{-8}	7.9	1.70	Demountable Test Set

near V_0 for targets of SnO_2 coated glass and aluminum foil. According to Equation (4)

$$\frac{1}{I_b}\frac{dI_t}{dV_t} = \eta.$$

The constant η can be taken as a figure of merit for the high-velocity beam and includes the effects of the secondary emission δ, the energy distribution of secondaries, and the kinetic energy of the primary electrons. In these measurements, the latter quantity was 300 ev. For the various tin-oxide-coated targets, the value of η does not change much as I_b is varied through a range of 20 to 1, and Equation (4) appears to be valid. For the aluminum foil, the beam conductance increases with the primary beam current, but less rapidly than predicted by Equation (4). The data of Table I shows that a beam current of 2×10^{-6} ampere will provide beam conductances of 10^{-7} mhos or greater near the equilibrium point on surfaces which are poor secondary emitters. This should be sufficient to reduce the capacitive lag to a level where it ceases to be objectionable. Another factor of 10 in conductance can be obtained by using the full output of the Vidicon gun, but this should not be necessary. In general, the redistribution effects increase with I_b, so that it is advantageous to use the minimum beam current which will result in an acceptable value of lag.

TEST OF HIGH-BEAM-VELOCITY VIDICON

An experimental high-beam-velocity Vidicon has been constructed and tested. Since this tube was designed primarily to verify the validity of the above theory, no special care was taken to select a photoconductor layer of outstanding sensitivity. The photoconductor was a glassy layer of antimony trisulfide, of medium sensitivity, sufficiently low intrinsic photoconductive lag, and having a capacitance of approximately 8000 picofarads. This capacitance is so high as to preclude its use in a low-beam-velocity Vidicon. The construction of the tube is shown in Figure 6. The collector mesh (750 lines/inch) is mounted on a rectangular aperture 0.005 inch from the scanned area. A similar aperture is mounted at the target end of the wall electrode. The purpose of these apertures is to shape the fields properly on the beam side of the mesh so that the collection efficiency will be uniform over the entire area of the mesh. The mesh aperture, M, is mounted on insulating spacers located on the periphery of the photoconductor. The tube is otherwise identical to the 7038 Vidicon and can be used in a standard camera with the addition of only one lead to the base.

Figure 6 shows typical values of the electrode voltages used in the high-velocity positive mode. The actual potential difference across the target (in this case, about 15 volts) is determined by the equilibrium potential, V_0, of the scanned surface, which must be determined by a separate experiment. In order to operate the tube in the high-velocity negative mode, it is necessary either to raise the mesh potential or to reduce the back-plate potential, V'.

The decay of the signal with time is shown in Figure 7. The procedure used was the same for low velocity as for both modes of high-velocity operation. The dark current was 2×10^{-8} ampere and the steady-state signal current was 1×10^{-7} ampere, which required a target illumination of 0.5 foot candle. The signal decay was ob-

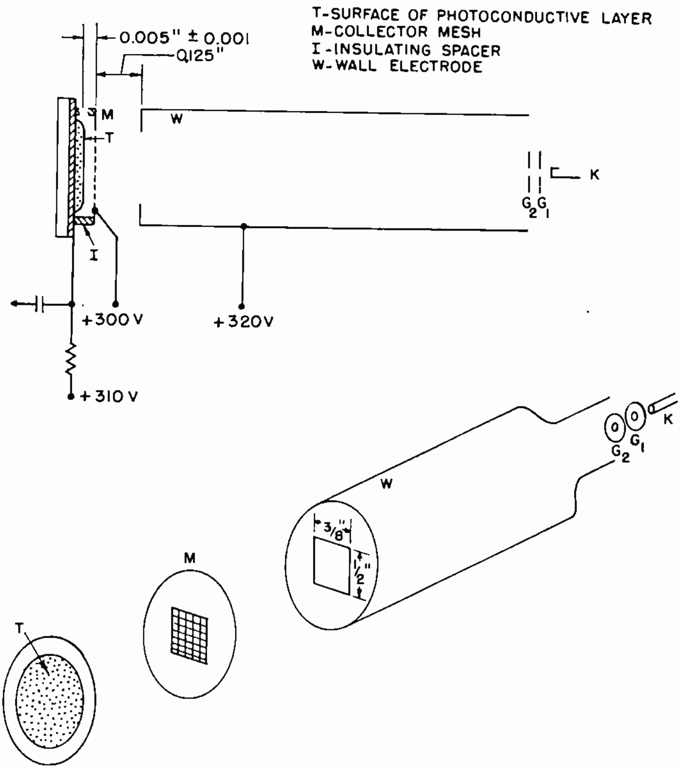

Fig. 6—Construction of experimental Vidicon for high-beam-velocity operation.

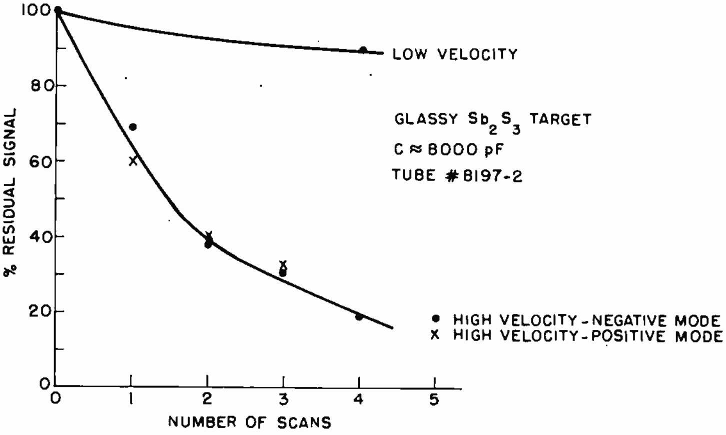

Fig. 7—Signal decay in the low- and high-velocity modes.

served by means of a line selector oscilloscope triggered by a mechanical light chopper. At low velocity, the signal decays to 89 per cent of maximum in four scans. This is roughly the capacitive lag to be expected from a layer with a capacitance of 8000 picofarads. At high velocity, using a beam current of approximately 4 microamperes, the residual signal is 20 per cent of maximum after four scans. This is slightly higher than the lag performance obtained from a Vidicon using a porous type photoconductor. There does not appear to be any difference in lag behavior between the positive and negative high-velocity modes.

Figure 8 shows the absolute value of the dark current as a function of collector potential, V_c, for a fixed value of the backplate potential, V' (260 volts). The transition between the two high-velocity modes occurs at $V_c = 265$ volts. At this point, there is no potential across the photoconductor, and the scanned surface must be at 260 volts. This point can be determined more precisely by applying a light signal to the tube and adjusting V_c for no output signal on the monitoring kinescope. Since $V_0 < V_c$, the beam conductance is controlled by the secondary emission from the collector mesh rather than from the scanned surface. This situation is favorable for the reduction of redistribution effects. Figure 8 also shows a faster rise of the dark current with voltage in the positive mode than in the negative mode. This indicates that the electron beam makes a better contact to the Sb_2S_3 layer than does the tin-oxide-coated glass electrode.

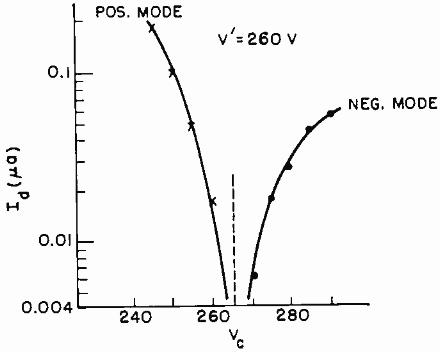

Fig. 8—Dark current versus collector potential. Since the surface of the photoconducting film stabilizes at $V_0 < V_c$, the beam conductance is controlled by the secondary electrons emitted from the collector mesh.

Figure 9 shows a test pattern and a half-tone scene obtained in the high-velocity negative mode. The vertical bars at the left side of the field originate in the test equipment and are due to pickup from the blanking pulses. They do not indicate any malfunction of the tube. The pictures appear to be free of spots due to imperfections on the mesh or scanned surface. The resolution is approximately 400 television lines. Seven steps can be distinguished in the gray scale, and the dynamic range is thus somewhat less than in a low-velocity tube. There are no severe redistribution effects, and the image appears fairly uniform over the entire field. There are still

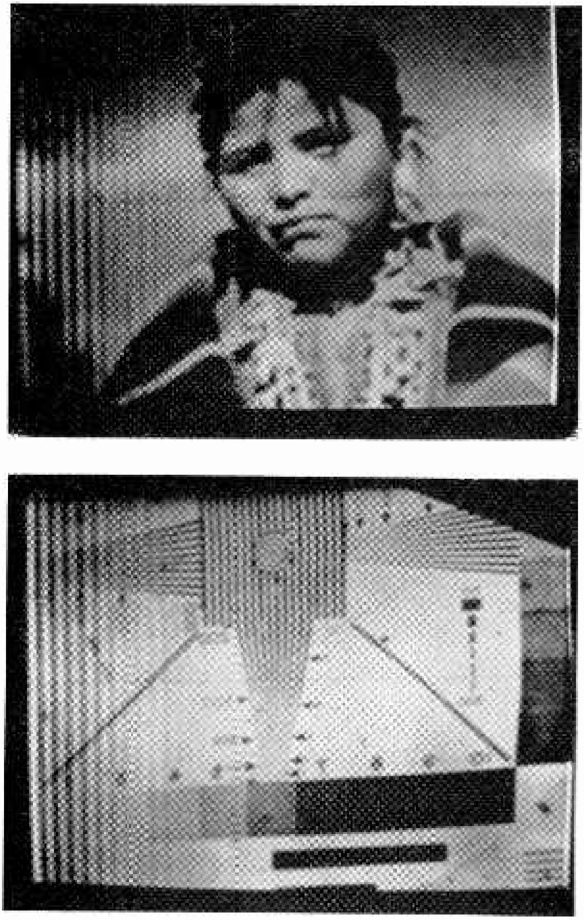

Fig. 9—High-velocity negative mode. The vertical bars at the left side of the field originate in the test equipment and are not due to malfunctioning of the tube.

some minor redistribution effects which can be seen at the boundaries of the steps in the gray scale and which tend to increase the contrast at the boundaries. The general image quality appears to be sufficient for many purposes.

CONCLUSIONS

The data presented shows that the capacitive lag associated with the glassy layers of high sensitivity can be reduced to lower levels, as predicted by the theory. The large redistribution effects, which heretofore precluded the use of a high-velocity beam, can be much reduced. There remain some local redistribution effects of small magnitude which do not greatly degrade the general image quality. Thus, it is possible to construct Vidicons, operating with high-velocity beam, which can take advantage of the inherent high sensitivity of the glassy photoconductive layers of antimony trisulfide.

It would be desirable to reduce further the small local redistribution effects which affect the contrast at the boundaries between dark and illuminated areas. In the positive mode, the contrast is decreased, thereby lowering the resolution. In the negative mode, the contrast at the boundary is increased. This tends to increase the resolution and to decrease the dynamic range of the tube. These effects increase with the magnitude of the primary beam current. In practice, therefore, the minimum beam current which will bring the capacitive lag down to a tolerable value should be used. Since the beam conductance is controlled by the secondary emission from the collector mesh, some improvement could be effected by properly selecting the mesh material. A mesh with a higher secondary emission would have a narrower energy distribution than the nickel mesh used in these experiments. An adequate value of the beam conductance would then be obtained with a lower primary beam current. Another approach to this problem is to bring the mesh closer to the scanned surface. The minimum practicable distance is probably of the order of 0.002-inch, which would necessitate the use of meshes of 1000 lines/inch.

The local redistribution problem is not at present serious enough to be an obstacle to the use of the high-beam-velocity Vidicon. A more important problem is the preparation of photoconductive layers having desirable properties to take advantage of the low capacitive lag. With the present state of the art, it is not always possible to manufacture such layers with sufficiently uniform properties to predict the performance of individual tubes. A discussion of the problems of obtaining films with uniform electrical properties or of selecting films prior to assembly of the tube is beyond the scope of this paper.

FUEL CELLS AND BATTERIES*

By

G. S. Lozier

RCA Semiconductor and Materials Division,
Somerville, N. J

Summary—*Fuel cells and batteries are devices which convert chemical energy directly into usable electrical energy by electrochemical processes. They differ only in the methods by which the chemical energy is stored and in the physical arrangement of the components. In a fuel cell, the chemical energy is stored externally and is fed into the cell at a rate determined by the power requirements of the load. In a battery, the chemical energy is stored within the cell. Because electrochemical processes are not restricted by a Carnot cycle, these devices can provide the most efficient method for converting chemical energy into electrical energy.*

This paper discusses the present state of development of fuel cells and batteries as energy sources and energy-storage devices. The various types discussed are evaluated from a consideration of the energy content of the reactant materials and the basic methods of handling the reactant materials in electrochemical cells. Regenerative electrochemical cells are also discussed, with emphasis on space applications.

EFFICIENCY OF CHEMICAL-TO-ELECTRICAL ENERGY-CONVERSION PROCESSES

CHEMICAL ENERGY may be converted to useful electrical energy by any of the basic processes shown in Figure 1. These processes may be evaluated as primary sources of power on the basis of performance characteristics such as energy density and energy-conversion efficiency. This paper discusses the relative importance of these characteristics, as determined by specific application requirements, as well as such other factors as reactant-material cost and convenience.

Electrochemical Conversion

In a fuel cell or battery, direct electrochemical conversion of chemical to electrical energy is essentially isothermal. As a result, the process escapes the Carnot-cycle limitation. The basic thermodynamic relationship between the maximum useful energy available from an electrochemical reaction and the heat content of the system is expressed by the following equation:

---

* Manuscript received 6 March 1961.

$$\Delta F = \Delta H - T\Delta S,$$

where ΔF is the free-energy change, ΔH is the heat-content change, ΔS is the entropy change, and T is absolute temperature. The maximum electrical energy available from an electrochemical process under reversible conditions is equal to the free-energy change of the reaction; the thermal efficiency, η_t, under ideal conditions may be expressed as

$$\eta_t = \frac{\Delta F}{\Delta H} = 1 - \frac{T\Delta S}{\Delta H}.$$

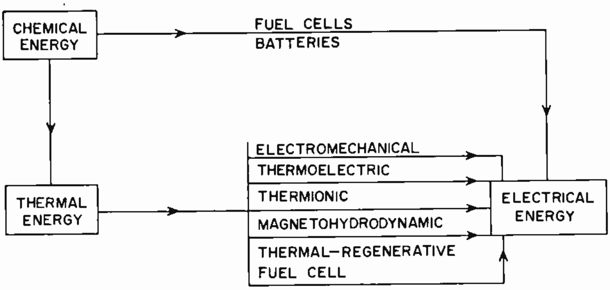

Fig. 1—Basic processes for the conversion of chemical energy to electrical energy.

Because the maximum thermal efficiency of an electrochemical cell is determined by the sign and magnitude of ΔS, which is usually small under normal operating conditions, a fuel cell or battery that approaches reversibility has a high theoretical thermal efficiency. In practice, this condition is met by cells operated near their theoretical open-circuit voltage because $-\Delta F = n\mathcal{F}E_0$, where E_0 is standard electrode potential (theoretical open-circuit voltage), $\mathcal{F}$ is the Faraday constant, and n is the electron change of the over-all cell reaction.

During battery operation, the electrochemical reaction produces both electrical energy and heat. The heat produced per mole is expressed by the equation $Q = -n\mathcal{F}(E_0 - E_{cv}) + T\Delta S$, where E_{cv} is the cell operating voltage. Deviations from reversibility result from the irreversibility of the electrode reactions and from cell resistances. Although the reaction heat can be used to maintain cell operating temperatures in some systems, in other systems it may be necessary to cool the cell.

Fuel-cell efficiency may also be stated in terms of current, voltage, and free-energy efficiencies, as shown in Table I. Free-energy efficiency is a measure of an electrochemical cell as an energy converter and may be used in comparing various cell types and constructions. Voltage efficiency is used as a first approximation of the free-energy efficiency when no side reactions or loss of active material exist (i.e., when the current efficiency is 100 per cent). Thermal efficiency is used to compare a fuel cell with an indirect process operating in a thermal cycle between the same initial and final states.

Table I

Thermal Efficiency	$\eta_t = \dfrac{\text{Electrical-energy output}}{-\Delta H} \times 100$ per cent
Free-energy Efficiency	$\eta_f = \dfrac{\text{Electrical-energy output}}{-\Delta F} \times 100$ per cent
Voltage Efficiency	$\eta_v = \dfrac{\text{Operating voltage}}{\text{Theoretical voltage}} \times 100$ per cent
Current Efficiency	$\eta_i = \dfrac{\text{Observed current}}{\text{Current equivalent of reactant materials}} \times 100$ per cent

Indirect Conversion

The efficiencies of the indirect processes shown in Figure 1 suffer from the unavoidable thermodynamic limitations imposed by a Carnot cycle on processes which convert heat into work. The maximum chemical energy that can be converted into electrical energy by a heat engine under ideal conditions is given by the expression

$$\Delta H \cdot \frac{T_H - T_C}{T_H},$$

where T_H is the temperature of the heat source of the heat engine and T_C is the temperature of the heat sink of the heat engine. Under preferred operating conditions, a central power plant would have a Carnot efficiency of approximately 65 per cent and an over-all efficiency of approximately 40 per cent. This figure is the highest efficiency obtained to date for the indirect conversion of chemical to electrical energy.

The efficiency of other conversion processes under investigation or in use are listed in Table II. These data indicate that electrochemical processes are the most efficient methods known for the direct conversion of chemical to electrical energy. The relative importance of the indirect conversion processes listed in Table II is beyond the scope of this paper.

Table II—Efficiency of Various Energy Converters

Device	*Conversion Process*	*Thermal Efficiency (Per cent)*
Fuel Cell or Battery	Chemical→Electric	90
Boiler/turbo Alternator	Heat→mechanical→electric	40
Rankine Vapor Cycles (steam, mercury, rubidium, and sodium)	Heat→mechanical→electric	38
Heat Engine Using Brayton Cycle	Heat→electric	28
Diesel Engine	Heat→mechanical	29-34
Gasoline Engine	Heat→mechanical	15-20
Thermionic	Heat→electric	14
Thermoelectric	Heat→electric	7
Magnetohydrodynamic	Heat→electric	up to 60 (estimated)

DIRECT CONVERSION OF CHEMICAL ENERGY INTO ELECTRICAL ENERGY

The basic components of a typical fuel cell and a typical primary cell and their functions are shown in Figures 2 and 3, respectively. In chemical terms, anode materials are reducing agents which are characterized by the ease with which they give up electrons and are oxidized to a higher oxidation state; cathode materials are oxidizing agents which are characterized by the ease with which they accept electrons and are reduced to a lower oxidation state. Electrical energy is derived from simultaneous oxidation of anode material and reduction of cathode material by electrochemical reaction; electrons flow

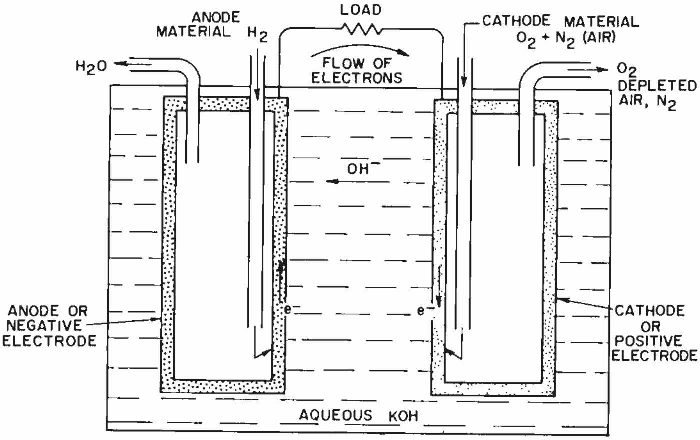

Fig. 2—Electrode reactions and relative flow of ions in a typical fuel cell (hydrogen–oxygen).

anode reaction: $H_2 + 2OH^- \rightarrow 2H_2O + 2e$

cathode reaction: $O_2 + 2H_2O + 2e \rightarrow 4OH^-$

over-all energy-producing reaction: $2H_2 + O_2 \rightarrow 2H_2O$

from the anode electrode through the external circuit to the cathode electrode.

The anode and cathode electrodes make electrical contact with the anode and cathode reactant materials. In the case of nonconducting anode and cathode materials, electrodes usually consist of some form

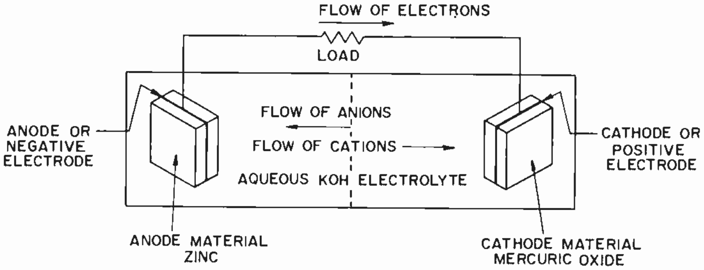

Fig. 3—Electrode reactions and relative flow of ions in a typical primary cell (zinc–mercuric oxide)

anode reaction: $Zn + 2OH^- \rightarrow Zn(OH)_2 + 2e$

$$Zn(OH)_2 \downarrow ZnO + H_2O$$

cathode reaction: $HgO + H_2O + 2e \rightarrow Hg + 2OH^-$

over-all energy-producing reaction: $Zn + HgO \rightarrow ZnO + Hg$

of a porous-carbon or metal matrix. In many electrochemical-cell designs, however, metal-anode material may also serve as the electrode. An electrolyte which permits the flow of ions between the anode and cathode electrodes completes the circuit.

On a weight and volume basis, the available energy from a fuel cell or battery is determined by the basic properties of anode and cathode materials. The two most basic properties are the ampere-hour capacity of the anode and cathode materials as determined by Faraday's Law and the cell potential as determined by the expression $-\Delta F = n\mathcal{F}E_0$. Tables III and IV list the theoretical ampere-hour capacities for various anode and cathode materials now used or being considered for use in batteries and fuel cells. The ampere-hour values, which are calculated on the basis of Faraday's Law, are directly proportional to the number of Faradays per mole involved in the

Table III—Capacity Data for Complete Oxidation of Various Anode Materials

Anode Material	*Theoretical Capacity* *Ampere Hours per pound*	 *Ampere Hours per cubic inch*
Hydrogen	12,062	30.6*
Methane	6,030	120. *
Propane	5,450	115. *
Decane	5,250	138. *
Pentaborane, stable	4,450	98. *
Carbon	4,049	330. #
Ethyl Alcohol (complete oxidation)	3,140	88.8*
Methyl Alcohol	2,250	64.5*
Lithium	1,751	33.6#
Formaldehyde	1,600	67.0*
Hydrazine	1,500	54.0*
Aluminum	1,352	132.0#
Ethyl Alcohol (partial oxidation)	1,040	29.6*
Magnesium	1,000	62.5#
Carbon Monoxide	860	115.0*
Iron	653	185. #
Sodium	528	18.4#
Zinc	371	96.0#
Cadmium	216	66.5#
Lead	118	47.5#

* Liquid state.
# Solid state.

electrochemical reaction. The ampere-hour capacity values are inversely proportional to the molecular weight and volume of material.

An examination of the basic properties of anode and cathode materials indicates why many approaches are being considered for the design of electrochemical cells as energy sources. For example, although hydrocarbons are promising materials, they are not electrochemically active in aqueous solutions and need high-temperature molten-salt electrolytes. This high-temperature problem has led to a consideration of redox systems and partially oxygenated carbon compounds as anode materials. These systems may be used in aqueous electrolytes for cells operated at approximately room temperature.

Table IV—Capacity Data for Various Cathode Materials

	Theoretical Capacity	
Cathode Material	*Ampere Hours per pound*	*Ampere Hours per cubic inch*
Oxygen	1510	62.3*
m-dinitrobenzene	862	49.5#
Fluorine	640	39.1*
Hexachloramelamine	436	25.6#
Chlorine	342	18.5*
Copper (II) Oxide	306	71.3#
Silver (II) Oxide	195	52.5#
Manganese (IV) Oxide	140	25.4#
Nickel Oxide**	133	
Mercuric (II) Oxide	110	42.3#
Lead (IV) Oxide	102	34.2#

---

* Liquid state.

** NiOOH is assumed to be active material in alkaline electrolytes.

\# Solid state.

The high-capacity metals either operate considerably below their reversible potentials or are too reactive to be used in aqueous electrolytes. However, an amalgam electrode apparently has solved the latter problem in the case of sodium. It should be noted that the anode materials currently used in electrochemical cells (zinc, cadmium, lead, and iron) have a fairly low capacity. Although magnesium is used in primary cells, it operates considerably below its reversible potential and at current efficiencies of 80 per cent or less. A typical borohydride compound was included in Table III because of its high theoretical ampere-hour capacity. The electrochemical problems associated with these materials are unknown.

Because oxygen has a high ampere-hour capacity and is readily available from the atmosphere, the design of electrochemical cells which use air as a cathode material is a desirable goal. In addition, oxygen cathodes make possible the design of invariant fuel cells with a variety of anode materials. Some of the problems associated with air operation are discussed later.

Fluorine, because of handling problems, and chlorine, because of both handling problems and low ampere-hour capacity with respect to oxygen, are not suitable as cathode materials. Oxide and organic cathode materials find most application in conventional primary and secondary cells.

Table V—Free Energy and Theoretical Watt-Hour per Pound for Various High-Energy Couples

Couple *Anode*	*Cathode*	*Over-all Reaction*	*ΔF at 25°C K cal/mole*	*Theoretical Watt-Hr./lb/for Over-all Reaction*	*E_0 at 25° volts*
H_2	O_2	$H_2 + \frac{1}{2}O_2 \rightarrow H_2O$	−56.7	1650	1.23
C	O_2	$C + O_2 \rightarrow CO_2$	−94.3	1120	1.02
CH_4	O_2	$CH_4 + 2O_2 \rightarrow CO_2 + 2H_2O$	−185.5	1220	1.01
C_3H_8	O_2	$C_3H_8 + 5O_2 \rightarrow 3CO_2 + 4H_2O$	−508.8	1280	1.10
$C_{10}H_{22}$	O_2	$C_{10}H_{22} + 15\frac{1}{2}C_2 \rightarrow 10CO_2 + 11H_2O$	−1,565.	1290	1.10
Li	F	$Li + F \rightarrow LiF$	−136.3 (aq)	2760	5.93
Li	Cl	$Li + Cl \rightarrow LiCl$	−102	1260	4.43
Na	O_2	$2Na + H_2O + \frac{1}{2}O_2 \rightarrow 2NaOH$	−144.6	950	3.14
N_2H_4	O_2	$N_2H_4 + O_2 \rightarrow N_2 + 2H_2O$	−143.2	1180	1.56
CH_3OH	O_2	$CH_3OH + 1\frac{1}{2}O_2 \rightarrow CO_2 + 2H_2O$	−167.7	1100	1.21
Formaldehyde	O_2	$CH_2O + O_2 \rightarrow CO_2 + H_2O$	−120.0	1010	1.31
Zinc	O_2	$Zn + \frac{1}{2}O_2 \rightarrow ZnO$	−75.7	490	1.64

Table V lists the theoretical energy content of some possible anode–cathode combinations calculated from ΔF of the over-all cell reaction at 25°C. Although many combinations have a high theoretical energy content, only a few can approach these values in practice. The principal reasons why electrochemical cells do not approach the theoretically available energy content are:

1. Because of the effects of activation, concentration, and

ohmic polarization encountered under load conditions, the voltage efficiency of electrodes is never 100 per cent.

2. The current efficiency is less than 100 per cent because of side reactions.
3. Active material is sometimes unavailable because of cell design.
4. The stoichiometry of the cell reaction requires use of water or some other nonenergy-producing component.
5. The storage containers for the materials and the auxiliary equipment represent an appreciable fraction of the total system weight and volume.
6. The electrical resistances in the cell reduce the total available energy.

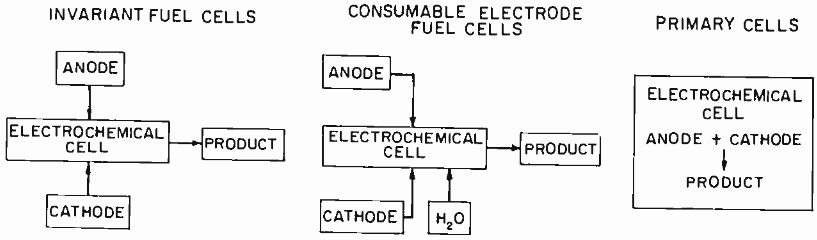

TYPCIAL SYSTEMS

ANODE	CATHODE	PRODUCT
H_2	O_2	H_2O
HYDROCARBONS	O_2	$CO_2 + H_2O$
ALCOHOLS	O_2	$CO_2 + H_2O$
ALDEHYDES	O_2	$CO_2 + H_2O$
HYDRAZINE	O_2	$N_2 + H_2O$

TYPICAL SYSTEMS

ANODE	CATHODE	PRODUCT
Na	O_2	NaOH(aq.)
Mg	Cl_2	$MgCl_2$(aq)
Zn	Cl_2	$ZnCl_2$(aq.)

TYPICAL SYSTEM

ANODE	CATHODE
Zn	MnO_2
Zn	AgO
Zn	HgO
Zn	CuO
Mg	MnO_2
Mg	m-dinitrobenzene
Mg	Cu_2Cl_2
Mg	AgCl

Fig. 4—Classification of electrochemical cells based on methods of handling materials.

TYPES OF ELECTROCHEMICAL CELLS

The simplified classification of fuel cells and batteries shown in Figure 4 is based on the means by which the active materials are handled, and indicates some of the important factors which determine the performance and energy density of an over-all electrochemical system. This method of classification has the advantage of grouping together active materials having similar properties. Typical electrochemical anode–cathode couples are indicated for each type of cell. The more conventional classifications, based on electrolyte type or operating temperature, are used when the various electrochemical couples are discussed.

In the invariant-type cell, the reactant materials form a product which can be removed from the cell without change in the electrolyte. The operating conditions of the cell require that there be no side reactions, corrosion, or deterioration of the electrodes. The most desirable anode–cathode couples are those in which H_2O, CO_2, and N_2 are the sole reaction products because these materials can be removed easily from the cell. The invariant fuel-cell systems are important because the total available energy density approaches the theoretical maximum, and the long operating life with little maintenance provides economical long-term operation.

Consumable-electrode fuel cells are electrochemical systems in which the reaction products cannot be removed without a change in the electrolyte composition. The anode materials in this class of fuel cell are high-energy-content metals (Al, Mg, Li, and Na), and the reaction products are materials which cannot be removed by simple processes. In the operation of some of these types of cells, the electrolyte may be circulated and the reaction products removed by filtration or complexing. In others, water may be added to maintain optimum electrolyte concentration.

A consumable-electrode fuel cell is the optimum physical arrangement for couples which use the high-energy metals listed in Table III. Despite their advantages over conventional primary cells of higher theoretical energy content, the full value of most of these systems is realized only when water is readily available. On a volume basis and under certain conditions of hydrogen storage, the consumable-electrode fuel cells will have a greater capacity than the hydrogen–oxygen fuel cell. The consumable-electrode fuel cells will have limited application because of availability and cost of reactant materials. The only advantage of these cells is their power density, which makes them suitable for some specific military applications.

The sodium-amalgam/oxygen system of the type shown in Figure 5 is the most highly developed of the consumable electrode cells. If a borohydride-anode electrochemical cell is developed, the borates formed must be removed by processes similar to those used for consumable-electrode cells.

Conventional primary cells differ from the above electrochemical cells in that the active materials are self-contained, and neither the active materials nor the electrolyte need be circulated for maximum performance. Because of their simplicity, primary cells are widely used as small portable sources of electric power. In general, the theoretical capacity of primary cells is considerably less than that of other systems because of the limitations placed on the active materials. These limitations are in part due to cell design, shelf life, and the cost of materials. The highest capacities of primary cells are approximately 80 watt-hours per pound and 7.5 watt-hours per cubic inch.

The construction and performance characteristics of various primary cells have been discussed in detail by Morehouse, Glicksman, and Lozier (see Bibliography). The recently announced zinc–oxygen fuel cell is a variation of the air cell and has characteristics similar to both consumable-electrode and primary-cell types.

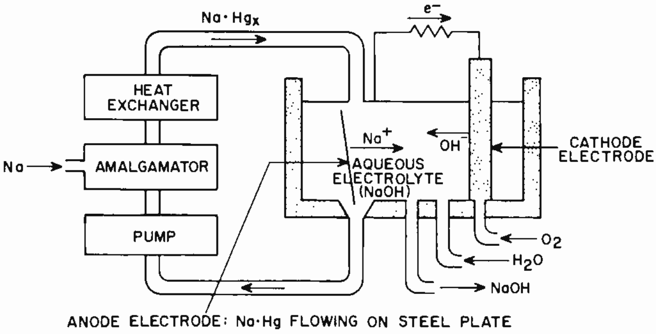

Fig. 5—Sodium-amalgam consumable-electrode fuel cell.

anode reaction: $NaHg_x \rightarrow Na+ + e + Hg_x$

cathode reaction: $O_2 + 2H_2O + 4e \rightarrow 4OH-$

over-all energy-producing reaction: $4NaHg_x + O_2 + 2H_2O \rightarrow 4NaOH + Hg_x$

Status of Invariant Fuel-Cell Systems

The electrochemical systems which meet the requirements of invariant operation fall in three broad classes: (1) hydrogen–oxygen systems, (2) direct and indirect cells which use low-cost carbonaceous fuels, and (3) low-temperature cells which use special reactant materials.

Hydrogen–Oxygen Fuel Cells

The hydrogen–oxygen fuel-cell system shown in Figure 2 is the most highly developed of all the fuel-cell systems and operates at practical power levels and good efficiencies for long periods. The most widely used types of hydrogen–oxygen fuel cells include low-temperature low-pressure cells, high-temperature high-pressure cells, and ion-membrane cells. The electrode design and operating conditions of these three types are summarized in Table VI.

High-temperature, high-pressure fuel cells operate at high current densities and are the most compact of the three types. However, high-temperature operation limits the life of the cells by rapid deterioration of the oxygen electrode. The longest operating life reported to date is approximately 1500 hours.

Table VI—Electrode Design and Operating Conditions of Various Hydrogen–Oxygen Cells

System	*Anode Electrode*	*Cathode Electrode*	*Electrolyte*	*Operating Temperature Degrees C*	*Operating Pressure*
High-Temperature, High-Pressure	Porous sintered nickel	Porous, sintered nickel pre-oxidized in LiOH	6-14 Molar KOH	200-240	400 PSI
Low-Temperature, Low-Pressure	Porous carbon with catalyst	Porous carbon with catalyst	6-14 Molar KOH	70	Atmospheri
Low-Temperature, Low-Pressure	Raney nickel	Porous nickel or silver with silver catalyst	5.5-7 Molar KOH	85	Atmospheri
Ion-membrane	Platinized nickel gauze	Platinized nickel gauze	Phenol sulfonic acid formaldehyde resin	Ambient	Atmospheri

Because these cells operate at a high temperature, they must be heated to start operation. When the cells are not operated at maximum power, some of the output may be used to maintain the cell temperature; a power output of 100 watts is the minimum practical capacity that can maintain self-sufficient operating temperature.

A further disadvantage is that these cells require hydrogen of high purity and oxygen which is free of carbon dioxide, because carbon dioxide forms a carbonate with an alkaline electrolyte. Although air can be used if the nitrogen and carbon dioxide are removed, the compression of nitrogen reduces the energy content of the system. The high-temperature operation permits relatively easy removal of the product water.

Low-temperature, low-pressure cells are simple, need little maintenance, and are easy to operate. They have a reasonable initial cost, and a long operating life. In contrast to the high-temperature cells, these cells do not require extremely pure reactants because the carbon electrodes are relatively insensitive to the catalytic poisons. Cells having anode materials such as carbon monoxide, alcohols, and aldehydes have been operated with good results at low temperatures. For long-term operation, however, the carbonate that is formed must be removed because the electrolyte is alkaline. The major factor affecting the operating life of this cell is the "wettability" of the porous carbon electrodes. Up to two years of operating life have been achieved.

The vaporized water product is passed into the hydrogen and oxygen feed gases and removed by circulating the feed gases in a condenser. The cell is designed so that this process occurs mainly in the hydrogen feed. The water is condensed in a separate unit and the feed gases are recirculated. For low-power applications, a considerable dilution of the electrolyte can be tolerated; because a one-ampere cell produces less than a pound of water during 1000 hours of operation, recirculation is not necessary.

The ion-exchange membrane cell shown in Figure 6 uses an ion-permeable membrane electrolyte which permits hydrogen ions to migrate from the anode electrode to the cathode electrode during current flow. Hydrogen ions react with oxygen and the electrons at the cathode electrode to form water. Although the water is automatically rejected, so that no special equipment is needed, the humidity on the electrodes must be controlled to prevent drying. Another important feature of the ion-exchange membrane is the use of an acidic electrolyte, which prevents carbonization of the electrolyte. The use of an acidic electrolyte permits operation of the cell in air.

Table VII summarizes the characteristics and performance data of the three types of hydrogen–oxygen fuel cells. The theoretical capacity of these cells on a weight basis is determined by the methods of handling and storing hydrogen. Theoretical capacities using various methods of reactant storage are compared with primary-battery capacities in Table VIII, which shows that high-capacity primary cells offer definite advantages for low-power requirements and short-term operation.

Various other methods of supplying hydrogen for large- and medium-power cells have been described by B. R. Stein. The most attractive methods are those which produce hydrogen by the dehydrogenation of methyl alcohol or similar materials, or which convert hydrocarbons, in the presence of steam and various catalysts, to

Table VII—Characteristics and Performance Data of Various Hydrogen–Oxygen Fuel Cells

System	*Cell-Size Data (Power Output Kilowatts)*	*Max. Power Output (KW/ft.³)*	*Max. Power Output (Watts/lb.)*	*Longest Reported Operating Life*	*Thermal Efficienc (per cent*
High-Pressure, High-Temperature	5-10 44	10.7	9.2 50	1500 hours	up to 80
Low-Pressure, Low-Temperature	1	3	20	2 years	65-70
Ion-Membrane	0.1	0.85	12	over 1 year	65-70

hydrogen and carbon dioxide. The carbon dioxide is then removed by the Gerbotol process.

Fuel cells of the hydrogen–oxygen system may eventually compete with conventional heat engines because the starting materials are both economical and easy to handle. Hydrogen–oxygen systems which are most tolerant of impurities in the hydrogen and are capable of operation in air at atmospheric pressure could most readily use hydrogen produced in this manner.

Invariant Fuel Cells Using Low-Cost Carbonaceous Fuels

The most promising invariant fuel cell is one which uses a low-cost carbonaceous material for the anode and which, on reaction with oxygen, produces carbon dioxide and water in stoichiometric amounts. The use of carbonaceous materials in fuel cells such as that shown in Figure 7 has been hindered by the fact that hydrocarbons, which are not electrochemically active at low temperatures, require a molten-salt electrolyte. Although the molten-salt electrolyte presents several serious design problems and makes small units impractical, these

Table VIII—Theoretical Energy-To-Weight Ratios of Various Hydrogen-Oxygen Cells Based on Various Methods of Storing H_2—O_2 and Optimum Experimental Capacity of Some Primary Batteries

	Watt-Hours per lb.
Liquid H_2 and Liquid O_2	1000
$NaBH_4$ and free air	280
Bottled H_2 and O_2	100-125
Silver-zinc primary cell	80
Magnesium meta-dinitrobenzene primary cell	90

high-temperature cells should find wide application in large power stations because of their high thermal efficiency. The performance characteristics and composition of various molten-salt fuel cells have been summarized by J. Yeager and by B. R. Stein (see Bibliography).

The following generalizations may be made concerning the material limitations and electrode reactions in these fuel-cell systems:

1. A carbonate electrolyte is required to maintain invariant cell conditions.

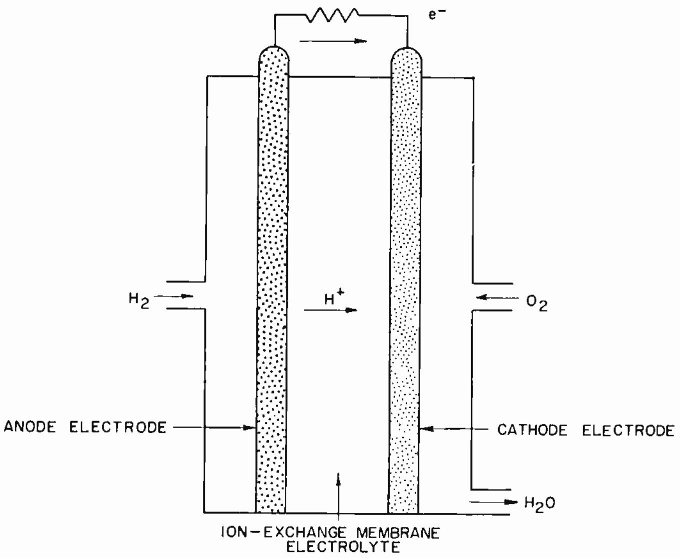

Fig. 6—Ion-exchange fuel cell.

anode reaction: $H_2 \rightarrow 2H^+ + 2e$

cathode reaction: $O_2 + 4H^+ + 4e \rightarrow 2H_2O$

over-all energy-producing reaction: $2H_2 + O_2 \rightarrow 2H_2O$

2. The fuel gas requires some cycling to obtain a maximum E_f. Free-energy efficiencies up to 78 per cent and thermal efficiencies up to 60 per cent have been reported for various carbonaceous fuels in the temperature range from 550 to 700 degrees centigrade.
3. Operational life is short due to loss of electrolyte by vaporization and corrosion of construction materials. The best reported operating life has been six months.

4. There is a potential problem of carbon deposition because of the Boudouard equilibrium $2\,CO \rightarrow C + CO_2$. This reaction can be controlled by proper choice of electrode materials and incoming-gas temperature.

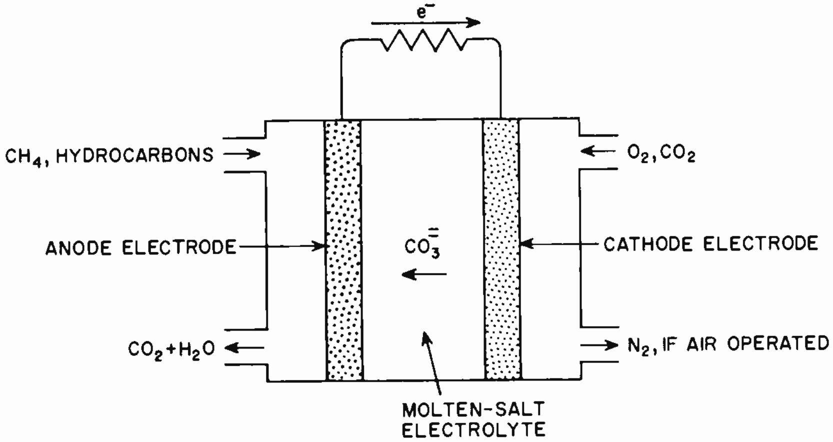

Fig. 7—Molten-salt fuel cell.

anode reaction: electrochemical

$$H_2 + CO_3^{=} \rightarrow H_2O + CO_2 + 2e$$

$$CO + CO_3^{=} \rightarrow 2CO_2 + 2e$$

chemical

$$CH_4 + H_2O \rightarrow CO + 3H_2$$

$$CO + H_2O \rightarrow CO_2 + H_2$$

cathode reaction: $\frac{1}{2}O_2 + CO_2 + 2e \rightarrow CO_3^{=}$

over-all energy-producing reaction: $CH_4 + 2O_2 \rightarrow CO_2 + 2H_2O$

The accepted cell reactions in a carbonate electrolyte are as follows:

Cathode: $\frac{1}{2}O_2 + CO_2 + 2e \rightarrow CO_3^{=}$

Anode: $H_2 + CO_3^{=} \rightarrow H_2O + CO_2 + 2e$
$CO + CO_3^{=} \rightarrow 2CO_2 + 2e.$

It should be noted that the $O^{=}$ ions are transferred almost completely in the solvated state of $CO_3^{=}$. In continuous operation, some CO_2 must be added to the oxygen.

The objective in this area is to produce a fuel cell which can use these materials at temperatures below 100 degrees centigrade and at atmospheric pressure. The problems arising from the handling and storage of hydrocarbon anode materials would be considerably fewer than those encountered with hydrogen. If the initial cost and size can be reduced, the invariant carbonaceous cell would be suitable as a power source for a wide variety of applications which now use conventional heat engines.

Some progress has been made toward this goal. One fuel cell has been demonstrated which operates on propane under ambient conditions. Another has been reported to give good performance with a fuel gas consisting of propane mixed with 33 per cent hydrogen.

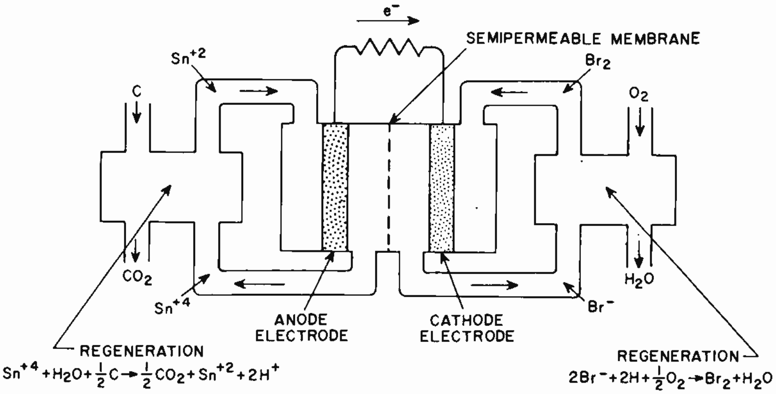

Fig. 8—Redox fuel cell.

anode reaction: $Sn^{+2} \rightarrow Sn^{+4} + 2e$

cathode reaction: $Br_2 + 2e \rightarrow 2Br^-$

over-all energy-producing reaction: $C + O_2 \rightarrow CO_2$

The fuel cell shown in Figure 8 offers another approach to the utilization of coal and cheap hydrocarbon anode materials at near-ambient conditions, and avoids the problems encountered in the handling of fused salts. The construction and principle of operation of the redox cells have been described by E. Yeager, B. R. Stein, and A. M. Posner (see Bibliography). The basic problems of redox systems include a lack of reduction–oxidation couples which provide favorable cell voltages and the difficulty in handling bromine. The membrane separating the anode and cathode materials must have a high electrical conductivity but be impermeable to the active ions.

Low-Temperature Fuel Cells

Some anode materials which can be used in ambient-temperature invariant fuel cells are the partially oxygenated organic materials such as methanol, formaldehyde, formate ions, and hydrazine. Present ambient-temperature fuel cells which use these organic materials use alkaline electrolytes and produce carbonates as the reaction product. A more detailed discussion has been given by H. Hunger (see Bibliography). Because hydrazine is reduced to water and nitrogen in alkaline electrolytes, it can be coupled to an oxygen cathode to form an invariant system. For special applications, the handling properties of hydrazine may make it a more desirable anode material than hydrogen. The operating characteristics of this system are not known at this time.

REGENERATIVE FUEL CELLS

Three primary sources of energy may supply the electric power to a space vehicle: chemical, nuclear, and solar. Chemical energy is limited as a primary power source in space applications because of its low energy-to-weight capacity. Until the reliability problems associated with a nuclear-energy source for space applications are overcome, solar energy is the only practical source of power. However, devices which use solar energy require a secondary power source for dark-time operation.

The high efficiency and simplicity of electrochemical processes has led to their consideration for space applications as a part of closed-cycle systems in which the chemical energy is continuously regenerated by solar or nuclear energy. These electrochemical systems are important for the following reasons:

1. They may be used as secondary power sources.
2. They can be used as energy converters with special properties.
3. They can provide, in one system, a combined high-efficiency energy converter and energy-storage device.

The block diagram shown in Figure 9 shows the over-all processes of regeneration. Two primary sources of energy have been considered, nuclear and solar energy.

It is a basic requirement that the reactions in the regenerative electrochemical cell be reversible, i.e., the anode and cathode materials must react electrochemically to form a product which must dissociate, without side reactions, to reform the reactants. Otherwise, the system would have a very limited cycle or operating life. Other important performance considerations of the electrochemical system include energy density per unit weight and volume, over-all efficiency, and power output per unit weight and volume.

Four methods of regenerating the chemical energy in a regenerative fuel cell by dissociation of the reactant materials are (1) photochemical, (2) radiochemical, (3) thermochemical, and (4) electrochemical. Because the direct processes for generating chemical energy photochemically and radiochemically are inefficient and offer many experimental difficulties, various indirect methods are being considered. Some of these methods, which involve the conversion of solar or nuclear energy to an intermediate form of energy (thermal or electric), are shown schematically in Figure 9. For space application in the present and the immediate future, these indirect processes seem the most practical on the basis of efficiency and design reliability. At present, energy-storage systems using electrochemical regeneration (the common secondary or storage battery) are the only systems in use. In particular, the nickel–cadmium secondary battery is used, although its capacity is as low as one watt-hour per pound under certain operating conditions. Other secondary systems either cannot be hermetically sealed in present designs or do not have the cycle life of the nickel–cadmium system. A possible exception is the cadmium–silver (II) oxide battery.

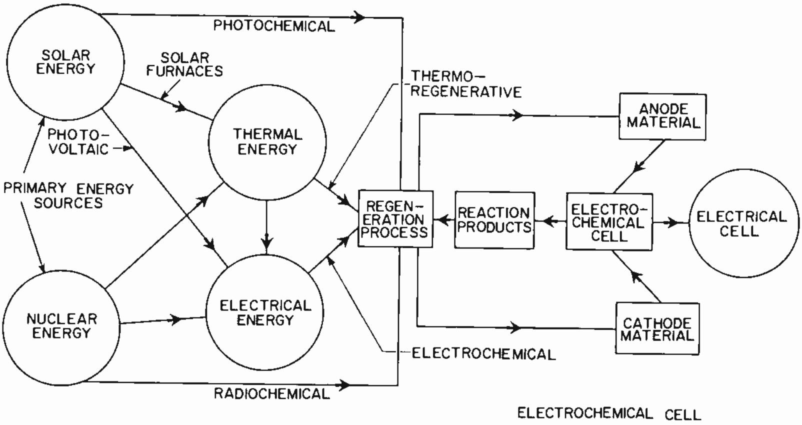

Fig. 9—Regeneration processes.

The disadvantages of conventional secondary batteries have increased the need for new electrochemical regenerative couples, but the requirement of reversibility greatly limits the available reactant materials, particularly anode materials. For example, the hydrocarbons, alcohols, formaldehyde, boron hydrides, and hydrazine cannot be electrochemically regenerated under conditions that are reversible. Although the hydrogen–oxygen couple shows the most promise for the development of an electrochemically regenerative secondary cell, the energy efficiency of the cell will probably never exceed 50 per cent because of the large difference between the voltage required to electrolyze water at a practical rate and the operating voltage of the cell. Practical use of hydrogen–oxygen cells will also be determined by the handling and storage problems of the reactant materials and the problems of separating liquid and gases in zero-gravity fields.

A zinc–oxygen reversible system is also being considered. Feasibility studies on new secondary couples utilizing alkali-metal or alkaline-earth-metal anode materials and various high-capacity cathode materials are in progress. However, the irreversibility of the alkali-metal and alkaline-earth-metal anode materials in aqueous electrolytes require the use of a nonaqueous electrolyte.

Thermal regenerative systems are attractive because they have a relatively high conversion efficiency, require a minimum of mechanical devices in high-temperature environments, and can be used in space applications where heat rejection from a thermal cycle is a problem.

Lithium hydride and closely related ionic-hydrides systems are the only practical systems proposed to date. The reactions occurring in these systems proceed as follows:

Electrochemical cell:

Anode: $2Li \rightarrow 2Li^{++} + 2e$

Cathode: $H_2 + 2e \rightarrow 2H^-$

Energy Reaction: $2Li + H \rightarrow 2LiH$ Open-circuit voltage 0.6 volt

Regeneration cell:

Regeneration Reaction: $2LiH \rightarrow 2Li + H_2$.

Although it is known that the efficiency of practical thermal regenerative systems will be lower than that of conventional heat engines, further investigations will determine their ultimate practicability.

All the direct photochemical regeneration processes under investigation have low efficiency ratings. Most of the endothermic photochemical reactions reported are irreversible, have very small quantum yields per low ΔF, and are physically unsuitable.

The NOCl system, the best reported to date, has a theoretical efficiency of 7 per cent. The over-all reactions in this system are as follows:

Regeneration Process:

$$NOCl \rightarrow NO + Cl$$

Electrochemical cell:

Anode: $NO \rightarrow NO^+ + e$

Cathode: $\frac{1}{2}Cl_2 + e \rightarrow Cl^-$

Over-all cell reaction: $NO + Cl \rightarrow NOCl$

The efficiency of a silicon photovoltaic converter is approximately 12 per cent. Photochemical systems that are based on the decomposition of water in the presence of cerous ions have an efficiency of approximately 0.1 per cent.

The radiochemical regenerative fuel cells are also characterized by a low efficiency. Efficiencies of three to five per cent have been obtained on systems using gamma rays from a cobalt-60 source to decompose acidified ferrous sulfate solutions to ferric sulfate and hydrogen. The electrochemical cell has a hydrogen anode and a ferric sulfate cathode. Another system uses the alpha decay Po^{210} to decompose water into hydrogen and H_2O_2; the H_2O_2 is then catalytically decomposed into H_2O and oxygen. The electrochemical cell in this case would be a hydrogen–oxygen cell.

CONCLUSIONS

The use of electrochemical cells as efficient energy sources is limited to primary cells. With the possible exception of the hydrogen–oxygen system, the fuel cells still require considerable development before they are ready for use as energy sources.

The use of electrochemical cells as secondary power sources is limited to the well-known secondary battery.

BIBLIOGRAPHY

Adams, A. M., "Electrochemical Cells as Energy Converters," *AIEE Conference Paper* No. CP 56-266, January, 1956.

Austin, L. F., "Fuel Cells," *Scientific American*, Vol. 201, pp. 72-92, 1959.

Davtvan, O. K., "Gas Cell with a Solid Electrolyte," *Izvest, Akad. Nauk, U.S.S.R., Otdell Tekli, Nauk*, Vol. 2, pp. 215-218. (1946) (British Electrical and Allied Industries Research Association, Technical Report Z/T 76).

Daniel, Bek, Mints, Sysoeva, and Tikhonova, "A Study of Fuel Cells with Solid Electrolytes," *4th Soviet Conference on Electrochemistry*, Academy of Science, U.S.S.R., Division of Chemical Science, October, 1956 (Abstract only).

Evans, G. E., "An Experimental Hydrogen–Oxygen Fuel Cell System," *Proceedings of the 12th Annual Battery Research and Development Conference*, pp. 4-8, U. S. Army Signal Engineering Laboratories, Fort Monmouth, N.J., May, 1958.

Gorin, E., and Recht, H. L., "Fuel Cells," *Chem. Eng. Progress*, Vol. 55, pp. 51-58, 1959.

Hunger, H., "Investigation of the Hydrogen-Oxygen Fuel Cell," *Proceedings of the 12th Annual Battery Research and Development Conference*, pp. 11-14, U. S. Army Signal Engineering Laboratories, Fort Monmouth, N.J., 1958.

Gurevich, I. G., "Contemporary State of the Development of Fuel Cells," *Inzhener Fiz. Zhur. Akad. Nauk. U.S.S.R.*, Vol. 1, pp. 75-88 (1958).

Liebhafsky, H. A., and Douglas, D. L., "The Fuel Cell," *Mech. Eng.*, Vol. 81, pp. 64-68, 1959.

McKee, Findl, Margerum, and Lee, "Solar Regenerative Fuel Cells," *Proceedings of the 14th Annual Power Sources Conference*, pp. 68-72, U. S. Army Signal Research and Development Laboratories, Fort Monmouth, N.J., May, 1960.

Neidrack, L., "An Ion-Exchange Membrane Fuel Cell," *Proceedings of the 13th Annual Battery Research and Development Conference*, U. S. Army Signal Research and Development Laboratories, Fort Monmouth, N.J., April, 1959.

Morehouse, Glicksman, and Lozier, "Batteries," *Proc. IRE*, Vol. 46, pp. 1462-1483, 1958.

Posner, A. M., "Redox Fuel Cell," *Fuel*, Vol. 34, pp. 330-338, 1955.

Recht, H. L., "High-Temperature Fuel Cells," *Proceedings of the 12th Annual Battery Research and Development Conference*, pp. 14-17, U. S. Army Signal Engineering Laboratories, Fort Monmouth, N.J., May, 1958.

Stein, B. R., "Status Report on Fuel Cells," *Army Research Office Report* No. 1, June, 1959.

Stein, B. R., and Cohen, E. M., "Second Status Report on Fuel Cells," *Army Research Office Report* No. 2, June 1961.

Shearer, R. E., and Werner, R. C., "Thermally Regenerated Ionic Hydride Galvanic Cell," Paper No. 5, National Meeting, *The Electrochemical Society*, Ottawa, October, 1958.

Yeager, E., "A Review of the State of the Art and Future Trends in Fuel Cell Systems," Technical Report No. 10, *Western Reserve University*, Cleveland, ONR Contract NOrd 2391(00), December, 1958.

Yeager, J. F., "Fuel Cells as Energy Converters," *Direct Conversion of Heat to Electricity*, Edited by J. Kaye and J. A. Welsh, John Wiley and Sons, Inc., New York, 1960.

Young, G. J., *Fuel Cells*, Reinhold Publishing Co., New York, 1960.

EFFECT OF DISTRIBUTED-LOSS NOISE GENERATORS ON TRAVELING-WAVE-TUBE NOISE FACTOR*†

BY

S. BLOOM

RCA Laboratories
Princeton, N. J.

Summary—An estimate is made of the effects on traveling-wave-tube noise factor of distributed Nyquist noise generators due to circuit loss. The contribution to noise factor is, in a representative case, of the order of 0.6 decibel. In the present state of the art, this is no longer a negligible effect.

THE CONVENTIONAL EXPRESSION for the minimum noise factor of a traveling-wave tube takes account of circuit loss only insofar as loss affects the gain. Thus the expression[1] for the excess noise factor, due to beam noise alone, contains the factor $1 + (d/x_1)$, where d and x_1 are the loss and gain parameters, respectively.[2]

Circuit loss can, however, have a more active effect on tube noise factor. This arises from the fact that the circuit distributed resistance produces a series of Nyquist thermal noise generators. The inclusion of circuit-loss noise generators in noise-factor formulas is common practice in the parametric amplifier and maser fields. With recent traveling-wave-tube noise factors in the range of 2.5 decibels, this hitherto neglected source of noise demands consideration.

The model here analyzed consists of a transmission line which is matched at both ends, and which has distributed series resistance, r, per unit length. The circuit is of length D, and distance z is measured from the input end. The power gain is exponential and at position z has the value $\exp(2\beta_e C x_1)z$, in Pierce's notation. The distributed resistance produces a Nyquist thermal noise voltage

---

* Manuscript received 22 March 1961.

† This work was supported by a Signal Corps Contract.

[1] S. Bloom, "The Effect of Initial Noise Current and Velocity Correlation on the Noise Figure of Traveling-Wave Tubes," *RCA Review*, Vol. 16, p. 179, June 1955.

[2] J. R. Pierce, *Traveling-Wave Tubes*, D. Van Nostrand Co., Inc., Princeton, N.J., 1950.

$$d\bar{v}^2 = (4kT\Delta f)\, r dz. \tag{1}$$

Neglecting interactions between the noise voltage generators and the traveling-wave-tube modes (which is a good approximation for small noisy losses and which underestimates the effects), one obtains for the noise power output due to these generators

$$P_r = \frac{1}{2}\,\frac{1}{2K}\,4kT\Delta f r \int_0^D \exp[2\beta_e C x_1 (D - z)]\, dz \tag{2}$$

$$= \left(kT\Delta f \frac{r}{K} \right) \frac{G-1}{2\beta_e C x_1}. \tag{3}$$

The factor of 1/2 in Equation (2) is due to half the power flowing to the right, the leftward half being harmless. K is the circuit characteristic impedance and G is the power gain. Since the output noise power due to antenna input noise is $kT_0\Delta f G$, the noise factor is

$$F = 1 + \frac{\dfrac{T}{T_0}\left(1 - \dfrac{1}{G}\right)\dfrac{r}{K}}{2\beta_e C x_1}. \tag{4}$$

This can be simplified as follows. The circuit propagation constant, for small loss, is

$$\beta = \sqrt{(r + j\omega L)}\,(j\omega c) \doteq j\omega\sqrt{Lc} + \frac{r}{2}\sqrt{c/L} \doteq j\omega\sqrt{Lc} + \frac{r}{2K}.$$

Hence the voltage attenuation varies as $\exp(-r/2K)z$. In Pierce's notation this takes the form $\exp(-\beta_e C d)z$. This relates d to r/K, and Equation (4) becomes

$$F = 1 + \frac{T}{T_0}\left(1 - \frac{1}{G}\right)\frac{d}{x_1}. \tag{5}$$

For large gain, then, the complete minimum noise factor, including both beam noise and circuit thermal noise, reads

$$F = 1 + \frac{T_c}{T_0}\,\frac{S - \Pi}{S_0}\left(1 + \frac{d}{x_1}\right) + \frac{T}{T_0}\,\frac{d}{x_1}. \tag{6}$$

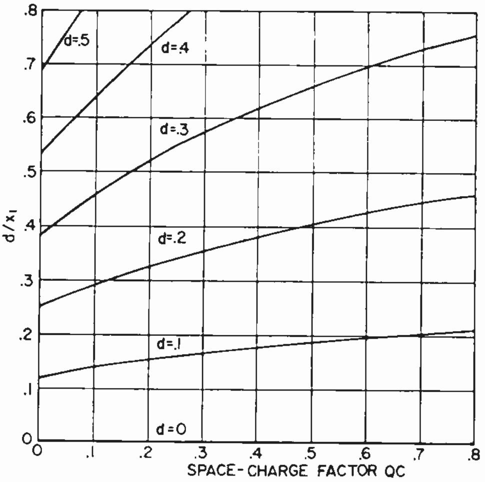

Fig. 1—Ratio, d/x_1, of loss parameter to gain parameter as a function of QC.

A tube having, for example, $QC = 0.1$ and $d = 0.15$ has $d/x_1 = .22$, as found from Figure 1 (Figure 5 of Reference 1). With the helix at room temperature ($T = T_0$), the noise factor in the absence of beam noise would be $1 + .22$, or 0.86 decibel. If this tube has a measured noise factor of 2.5 decibels, then the beam noise term has the value $(T_c/T_0)\ [(S - \Pi)/S_0] = .46$. Hence a *refrigerated* helix ($T \ll T_0$) would yield a noise factor (neglecting any reduction of d due to lowered temperature), of $F = 1 + (.46)\ (1 + .22)$, or 1.93 decibels. Alternatively, the noise factor for a resistanceless circuit ($d = 0$) is $F = 1 + .46$, or 1.65 decibels.

The third term in Equation (6) *underestimates* the contribution due to distributed circuit loss since the present model neglects, for example, the effects due to mismatch. Furthermore, because the loss factor, d, increases with frequency, the use of circuit refrigeration could play an important role in extending the low-noise-tube art to super-high frequencies.

RCA TECHNICAL PAPERS†

First Quarter, 1961

Any request for copies of papers listed herein should be addressed to the publication to which credited.

"Calculated Waveforms for Tunnel Diode Locked Pair," H. R. Kaupp and D. R. Crosby, *Proc. I.R.E.* (January)	1961
"Computer Memories: A Survey of the State-of-the-Art," J. A. Rajchman, *Proc. I.R.E.* (January)	1961
"A Computer Subsystem Using Kilomegacycle Subharmonic Oscillators," I. Abeyta, F. Borgini, and D. R. Crosby, *Proc. I.R.E.* (January)	1961
"Design and Operation of Four-Frequency Parametric Up-Converters," J. A. Luksch, E. W. Matthews, and G. A. VerWys, *Trans. I.R.E. PGMTT* (January)	1961
"Distortion of Auditory Perspective Produced by Interchannel Mixing at High and Low Audio Frequencies," D. S. McCoy, *Jour. Aud. Eng. Soc.* (January)	1961
"Electronic Brightness Contouring," R. L. Hallows, *Jour. S.M.P.T.E.* (January)	1961
"Electron Spin Resonance and Optical Absorption of $K_3[Cr(CN)_5NO] \cdot H_2O$," I. Bernal and S. E. Harrison, *Jour. Chem. Phys.* (January)	1961
"Improvements in Encapsulated Silicon Junction Alpha Detectors," R. W. Jackson, P. P. Webb, and R. L. Williams, *Trans. I.R.E. PGNS* (January)	1961
"Optical Determination of the Conduction Band Structure of GaSb," M. Cardona, *Journal of the Physics and Chemistry of Solids* (January) (Letters to the Editor)	1961
"Particle Interaction in Magnetic Recording Tapes," J. G. Woodward and E. Della Torre, *Jour. Appl. Phys.* (January) (Letters to the Editor)	1961
"Space Charge Instabilities in Synthesized Plasmas," A. L. Eichenbaum and K. G Hernqvist, *Jour. App. Phys.* (January)	1961
"Standardization of Electronic Test Equipment," D. B. Dobson and L. L. Wolff, *Elec. Eng.* (January)	1961
"A Television Imagery Simulator," J. P. Smith and J. F. Baumunk, *Jour. S.M.P.T.E.* (January)	1961
"Transistor Form of Nuclear Particle Detector," R. L. Williams and P. P. Webb, *Trans. I.R.E. PGNS* (January)	1961
"Universal Representation of Electromagnetic Parameters in Presence of DC Magnetic Fields," M. P. Bachynski, T. W. Johnston, and I. P. Shkarofsky, *Proc. I.R.E.* (January) (Correspondence)	1961
"Current-Voltage Characteristics of Forward Biased Long p-i-n Structures," R. D. Larrabee, *Phys. Rev.* (January 1)	1961
"Volume-Controlled, Two-Carrier Currents in Solids: The Injected Plasma Case," M. A. Lampert and A. Rose, *Phys. Rev.* January 1)	1961
"Effect of Photoexcitation on the Mobility in Photoconducting Insulators," R. H. Bube and H. E. MacDonald, *Phys. Rev.* (January 15)	1961
"Controlling with Magnetic Cores," M. Cooperman, *Electronic Industries* (February)	1961

---

† Report all corrections to *RCA Review*, RCA Laboratories, Princeton, N. J.

"Method of Measuring and Controlling Evaporation Rates During the Production of Thin Films in Vacuum," H. Schwarz, *Rev. Sci. Instr.* (February) 1961

"Rise-Time Measurements in MgO Cold Cathode Diodes," A. Sussman, *Proc. I.R.E.* (February) (Correspondence) 1961

"Thermal Diffusivity of Armco Iron," G. D. Cody, B. Abeles, and D. S. Beers, *Trans. Metallurgical Society of AIME* (February) 1961

"Electron Effective Masses of InAs and GaAs as a Function of Temperature and Doping," M. Cardona, *Phys. Rev.* (February 1) 1961

"Electron Microscopy," S. G. Ellis, *N. Y. Jour. of Medicine* (February 1) 1961

"A Misplaced Solar Event," J. H. Nelson, *Electronics* (February 10) (Comment) 1961

"Algorithm 37, Telescope 1," K. A. Brons, *Communications of the Association for Computing Machinery* (March) 1961

"Algorithm 38, Telescope 2," K. A. Brons, *Communications of the Association for Computing Machinery* (March) 1961

"An Algorithm for Determining Minimal Normal Forms of an Incomplete Truth Function," T. H. Mott, Jr., *Communication and Electronics* (March) 1961

"Beacon Transmitters and Power Supply for Echo I," J. G. McCubbin and H. B. Goldberg, *RCA Review* (March) 1961

"Considerations of Photoemissive Energy Converters," W. E. Spicer, *RCA Review* (March) 1961

"Direct Conversion of Heat to Electromagnetic Energy," F. M. Johnson, *RCA Review* (March) 1961

"Effect of Series Resistance on Photovoltaic Solar-Energy Conversion," J. J. Wysocki, *RCA Review* (March) 1961

"Electrically Variable Time Delay Using Cascaded Drift Transistors," R. W. Ahrons, *Semiconductor Products* (March) 1961

"Ferroelectric Scanning of Electroluminescent Displays," M. Cooperman, *RCA Review* (March) 1961

"Indium Arsenide Tunnel Diodes," H. P. Kleinknecht, *Solid-State Electronics* (March) 1961

"Large-Area Thin-Film Photovoltaic Cells," H. I. Moss, *RCA Review* (March) 1961

"Majority Gates Applied to Simultaneous Comparators," H. S. Miiller, *Trans. I.R.E. PGEC* (March) (Correspondence) 1961

"New Results on Frequency Multiplication and Nonlinear Phase Distortion in Klystrons and Traveling-Wave Tubes," F. Paschke, *RCA Review* (March) 1961

"Noise Smoothing by Reactive Damping in Finite Multivelocity Electron Beams," J. Berghammer, *RCA Review* (March) 1961

"Nondestructive Measurement of Tensile and Compressive Stresses," R. A. Shahbender, *Trans. I.R.E. PGUE* (March) 1961

"Plasma Synthesis and Its Application to Thermionic Power Conversion," K. G. Hernqvist, *RCA Review* (March) 1961

"Power Supply for the Tiros I Meteorological Satellite," S. H. Winkler, I. Stein, and P. Wiener, *RCA Review* (March) 1961

"The Present Outlook for Controlled Thermonuclear Fusion," G. Warfield, *RCA Review* (March) 1961

"Semiconductor Materials for Thermoelectric Power Generation," F. D. Rosi, E. E. Hockings, and N. E. Lindenblad, *RCA Review* (March) 1961

"Spectrally Selective (Solar Blind) UV Photomultipliers with Fluoride Windows," A. H. Sommer, *Rev. Sci. Instr.* (March) (Notes) 1961

"Spectral Response of Photovoltaic Cells," J. J. Loferski and J. J. Wysocki, *RCA Review* (March) 1961

"Synthesis of Low-Reflection Waveguide Joint Systems," P. Foldes and N. Gothard, *Trans. I.R.E. PGMTT* (March) 1961

"Transfluxor Design Considerations," W. L. Morgan, *Trans. I.R.E. PGED* (March) 1961

"Writing—Newest Engineering Skill," H. Baum, *Electronic Industries* (March) 1961

"Diffusion in Compound Semiconductors," B. Goldstein, *Phys. Rev.* (March 1) 1961

"The Crystal Structures of $TlSbTe_2$ and $TlBiTe_2$," E. F. Hockings and J. G. White, *Acta Crystallographica* (March 10) (Short Communications) 1961

"Observations of Electron-Hole Current Pinching in Indium Antimonide," M. Glicksman and R. A. Powlus, *Phys. Rev.* (March 15) 1961

"Logical Sequence and Random Sequence," E. I. Gavurin and V. M. Donahue, *Automated Teaching Bulletin* (Spring) 1961

"Alternate Routing Computer," A. Kritz and H. Roberts, *Convention Record, Fifth National Symposium on Global Communications* 1961

"Communication Error Rate Instrumentation System," J. Rabinowitz, A. Tepfer, and Coauthors, *Convention Record, Fifth National Symposium on Global Communications* 1961

"Contribution a L'Etude de L'Emission Infrarouge Dans Le Germanium," (Thesis), J. I. Pankove, *Annales de Physique*.... 1961

"Luminescence," H. W. Leverenz, *Encyclopaedia Britannica* 1961

"A New Digital Communication System Modified Diphase," G. Aaronson, D. A. Douglas, and G. J. Meslener, *Convention Record, Fifth National Symposium on Global Communications*...... 1961

"Nomograms for the Statistical Summation of Noise in Multihop Communications Systems," B. Sheffield, *Convention Record, Fifth National Symposium on Global Communications* 1961

"Synthesis of a Global Communications System Using Wideband Radio Relay Systems," J. B. Potts, *Convention Record, Fifth National Symposium on Global Communications* 1961

AUTHORS

J. R. Andersen received his B.S.M.E. and M.S.M.E. degrees from the University of California in 1937 and 1939, respectively, and his Ph.D. degree in Mechanical Engineering from the University of Pennsylvania in 1949. He was an instructor in the Applied Mechanics Department, Kansas State College during 1939-40, and from 1940 to 1958 was a member of the faculty of the Mechanical Engineering Department, University of Pennsylvania, being appointed Associate Professor in 1953. Dr. Andersen has been active in research on the thermodynamic properties of gases and moist air, the transmission of infrared radiation by the earth's atmosphere, and the diffusion of smoke in a turbulent atmosphere. Also, he has been an engineer for Douglas Aircraft Co., Pratt and Whitney Aircraft Co., Vultee Aircraft, and Westinghouse Electric Corporation, and has served as a consultant to RCA on heat transfer as related to electronic equipment. Dr. Andersen joined RCA in 1958 as Leader in Applied Research's Electro-Mechanics Group, concentrating his efforts on extending and demonstrating the practical applications of thermoelectricity to military systems.

Dr. Andersen is a member of Tau Beta Pi and Sigma Xi, and was a member and later chairman of the standing committee on Thermophysical Properties of Materials, Heat Transfer Division, American Society of Mechanical Engineers.

Stanley Bloom received the B.S. degree in Physics and Mathematics from Rutgers University in 1948. In 1949 he received the M.S. degree in Physics and in 1952, the Ph.D. degree in Physics from Yale University. In 1952 he joined the RCA Laboratories where he has engaged in research on traveling-wave tubes, plasmas, magnetic resonance, and parametric amplifiers. Dr. Bloom is a Senior Member of the IRE and is a Member of the American Physical Society, Sigma Xi, and Phi Beta Kappa.

K. K. N. Chang received the B.S. degree from the National Central University, Nanking, China, in 1940; the M.S. degree in Electrical Engineering from the University of Michigan in 1948, and the D.E.E. degree in 1954 from the Polytechnic Institute of Brooklyn. From 1940 to 1945, he was associated with the Central Radio Manufacturing Works, Kunming, China, working on radio receivers and from 1945 to 1947, he was a radio instructor in the Office of Strategic Service, U. S. Army, China Theatre. Since 1948, he has been at RCA Laboratories, Princeton, N. J., where he has engaged in research on magnetrons, traveling-wave tubes, beam-focusing devices, and parametric amplifiers. Dr. Chang is a member of Sigma Xi.

C. Louis Cuccia received the B.S. degree in E.E. in 1941 and the M.S. degree in 1942, both from the University of Michigan. From 1941 to 1942 he was also employed as a Research Engineer for the Fisher Body Division of General Motors. He joined the technical staff of the RCA Laboratories in 1942 and worked on microwave-tube research and development until 1954. From 1954 to 1957, he was assigned to the color-television activity of the RCA Patent Department, specializing in the evaluation and patenting of new color-television receiver circuits. Early in 1957, he joined the Microwave Operations of the Electron-Tube Division as Engineering Leader in charge of traveling-wave-tube and backward-wave-oscillator design and development. In 1959, he became responsible for the product development of varactor and tunnel-diode signal sources and amplifiers for the RCA Electron Tube Division, and in January 1961, he was named to manage that Division's new West Coast Microwave Engineering Laboratory in Los Angeles, to provide product development of solid-state microwave components and application programs on microwave tubes.

Joseph Dresner received the B.S. degree in 1949 and the M.S. in physics in 1950 from the University of Michigan. From 1950 to 1953 he did research on the medical uses of high-energy x-rays at the Hospital for Joint Diseases, in New York. He was research assistant at the Laboratory of Professor Kallmann at N.Y.U. in 1953-1958, at which time he did research on luminescence in solids. He received Ph.D. in physics in 1958 from N.Y.U., following which he joined the Technical Staff of RCA Laboratories. Since that time, Dr. Dresner has done research on television pickup tubes and on the study of electronic processes in photoconductors and insulators.

Gerald S. Lozier received the B.S. degree in chemistry in 1952, the M.S. degree in chemistry in 1953, and the Ph.D. degree in 1956 from Western Reserve University, Cleveland, Ohio. From September 1950 until September 1952, he held a Teaching Fellowship at Western Reserve. For the next two years, he was engaged in research on the effects of ultrasonics on electrode processes, an Office of Naval Research project, at Western Reserve. In January 1955, he joined RCA Laboratories at Princeton, N. J., where he engaged in research into new electrochemical systems. In July 1959, he transferred to the RCA Semiconductor and Materials Division in Somerville, N. J. As head of the group responsible for the development of both military and commercial systems, he has continued research on battery systems and fuel cells. Dr. Lozier is a member of the American Chemical Society and the Electrochemical Society.

T. Murakami received the B.S. degree in E.E. from Swarthmore College in 1944, and the M.S. degree from the Moore School of Electrical Engineering, University of Pennsylvania in 1947. From 1944 to 1946 he was an assistant and research associate in the Department of Electrical Engineering at Swarthmore College. From 1946 to 1961 he was associated with the Advanced Development Section of the RCA Home Instruments Division, Camden, N. J., working on radio-frequency circuit development and analyzing various radio and television problems. Since January 1961 he has been with the Advanced Techniques Development group of the RCA Missile and Surface Radar Division at Moorestown, N. J. Mr. Murakami is a Senior member of the Institute of Radio Engineers and a member of Sigma Xi and Sigma Tau.

Herbert J. Wolkstein received the B.S. degree in Electrical Engineering from Newark College of Engineering and is presently working toward an MS degree in the same field. Before joining RCA, he was employed at the Research Laboratories of National Union Electric Corporation as Project Engineer on the design of special-purpose beam-deflection and computer tubes. He joined the Microwave Tube Engineering activity of the RCA Electron Tube Division in 1955 where he has been engaged in the development of traveling-wave tubes. He is currently Engineering leader of the traveling-wave-tube group and has written a number of articles pertaining to this work. Mr. Wolkstein is a member of the Institute of Radio Engineers.